EFFECTS OF GRAIN SIZE ON THE QUASI-STATIC MECHANICAL PROPERTIES OF ULTRAFINE-GRAINED AND NANOCRYSTALLINE TANTALUM

by

Jonathan Paul Ligda

A dissertation submitted to the faculty of
The University of North Carolina at Charlotte
in partial fulfillment of the requirements
for the degree of Doctor of Philosophy in
Nanoscale Science.

Charlotte

2013

Approved by:

Dr. Qiuming Wei

Dr. Brian Schuster

Dr. Terry Xu

Dr. Stuart Smith

Dr. Barry Sherlock

ABSTRACT

JONATHAN PAUL LIGDA. Effects of grain size on the quasi-static mechanical properties of ultrafine-grained and nanocrystalline tantalum.
(Under the direction of DR. QIUMING WEI)

The increase in strength due to the Hall-Petch effect, reduced strain hardening capacity, a reduced ductility, and changes in deformation mechanisms are all effects of reducing grain size (d) into the ultrafine-grained (UFG, $100 < d < 1000$ nm) and nanocrystalline (NC, $d<100$ nm) state. However, most of the studies on the mechanical behavior of UFG/NC metals have been on face-centered cubic (FCC) metals. Of the few reports on UFG/NC body-centered cubic (BCC) metals, the interest is related to their increase in strength and reduced strain rate sensitivity. This combination increases their propensity to deform via adiabatic shear bands (ASBs) at high strain rates, which is a desired response for materials being considered as a possible replacement for depleted uranium in kinetic energy penetrators. However, an ideal replacement material must also plastically deform in tension under quasi-static rates to survive initial launch conditions. This raises the question: if the material forms ASBs at dynamic rates, will it also form shear bands at quasi-static isothermal rates? As well as, is there a specific grain size for a material that will plastically deform in tension at quasi-static rates but form adiabatic shear bands at dynamic rates?

Using high pressure torsion, a polycrystalline bulk tantalum disk was refined into the UFG/NC regime. Using microscale mechanical testing techniques, such as nanoindentation, microcompression, and microtension, it is possible to isolate locations with a homogeneous grain size within the disk. Pillars are compressed using a

nanoindenter with a flat punch tip, while “dog-bone” specimens were pulled in tension using a custom built *in-situ* tension stage within a scanning electron microscope (SEM). The observed mechanical behavior is related to the microstructure by using transmission electron microscopy (TEM) on the as-processed material and tested specimens. Synchrotron X-ray based texture analysis was also conducted on the disk to determine if any changes in the deformation texture occur during HPT processing.

Nanoindentation data shows a trend of increasing hardness with radial position that saturates at 4.5 GPa near the edge, and decreasing strain rate sensitivity. The micromechanical tests show two distinct regions on a processed circular disk, a non-shearing region and a shearing region. Microcompression/tension tests in the region of $1.0 \leq X \leq 5.3$ mm (X is the radial distance from the disk center) show limited strain hardening, homogeneous plastic deformation, and tensile elongation that varies from 0.3 – 4.0%. Tests performed at $X > 5.3$ mm show a drastic switch to localized plastic deformation in the form of shear bands, with evidence of grain rotation as the active deformation mechanism, and a measureable tension-compression asymmetry.

Grains are elongated at all locations, and while the minimum diameters are consistent between regions, the elongated diameter in the shearing region is reduced. The transition to localized deformation is attributed to this reduced dimension. A larger percentage of grains in the shearing region have an elongated diameter below the critical grain size necessary to activate the grain rotation mechanism. The tension-compression asymmetry is due to an increased dependence on the normal stress for yielding, meaning NC Ta would follow a Mohr-Coulomb criterion over the traditional Tresca or von Mises.

DEDICATION

This work is dedicated to my family and friends for their continuing support and encouragement during my graduate studies.

ACKNOWLEDGEMENTS

I would like to thank my advisor, Dr. Qiuming Wei, for allowing me to join his group and for all the help and advice given to me during my research. Also I would like to thank Dr. Brian Schuster for giving me the opportunity to perform my research at the Army Research Laboratory and all the assistance provided to me while there.

A special thanks to the many individuals who provided their assistance during various stages in the research. Dr. Ruslan Valiev, from Ufa State Aviation Technical University, for performing the HPT processing on bulk tantalum. Dr. Ken Strawhecker (ARL) and Mr. Quinn McAllister (Univ. of Delaware) provided their expertise in nanoindentation testing. Assistance with texture analysis was provided by Dr. Yang Ren and the entire beamline staff at APS. Use of the Advanced Photon Source, an Office of Science User Facility operated for the U.S. Department of Energy (DOE) Office of Science by Argonne National Laboratory, was supported by the U.S. DOE under Contract No. DE-AC02-06CH11357. TEM Orientation Mapping was done by Mr. Daniel Scotto D'Antuono with the permission of Dr. Mitra Taheri at Drexel University. Diamond Anvil Cell testing on HPT processed Ta was performed by Dr. Jennifer Ciezak-Jenkins (ARL) at ALS beamline12.2.2. The Advanced Light Source is supported by the Director, Office of Science, Office of Basic Energy Sciences, of the US Department of Energy under Contract No.DE-AC02-05CH11231.

I would also like to acknowledge the support and funding provided by UNC Charlotte, the Nanoscale Science Program, and the Army Research Laboratory through ORISE Fellowship.

Lastly, I would like to thank the other members of my dissertation committee, Dr. Stuart Smith, Dr. Terry Xu and Dr. Barry Sherlock for their valuable input and time.

TABLE OF CONTENTS

LIST OF TABLES

LIST OF FIGURES

LIST OF ABBREVIATIONS

NC	nanocrystalline	μ-EDM	micro-electro discharge machining
UFG	ultra-fine grained	LMIS	liquid metal ion source
BCC	body center cubic	MP	melting point
FCC	face center cubic	SE	secondary electrons
HCP	hexagonal close packed	SRIM	stopping range of ions in matter
IGC	inert gas condensation	TRIM	transmission range of ions in matter
SPD	severe plastic deformation	MEMS	micro-electrical mechanical systems
HPT	high pressure torsion	BMG	bulk metallic glass
ECAP	equal channel angular pressing	SXRD	synchrotron x-ray diffraction
ARB	accumulative roll bonding	MAUD	materials analysis using diffraction
MF	multiple forging	CSM	constant stiffness mode
FIB	focused ion beam	SAED	selected area diffraction pattern
SEM	scanning electron microscope	DIC	digital image correlation
TEM	transmission electron microscope	BF	bright field
SRS	strain rate sensitivity	DF	dark field
ASB	adiabatic shear band		
DU	depleted uranium		
KE	kinetic energy		

D-S	debye-scherrer	IPF	inverse pole figure
APS	advanced photon source		

CHAPTER 1: INTRODUCTION AND LITERATURE REVIEW

1.1 Hall-Petch Effect

There are many different techniques used to strengthen metals but each one is based on the premise of impeding the motion of dislocations through the crystal [1]. The most basic strengthening method is cold-working, where plastic deformation increases the dislocation density, and these dislocations form cells or forests which then act as barriers to the motion of other dislocations [2]. This technique will only achieve modest increases in strength since the amount of cold work is related to how much plastic strain is introduced into a material. Other strengthening techniques such as precipitate hardening and solid-solution strengthening require the addition of different materials to the metal lattice which act as the barriers to dislocations [3]. While both are effective at improving the strength, one of the best methods is grain refinement. In the early 1950's research on the lower yield point (σ_{LYP}) and cleavage strength (σ_c) of steels by E.O. Hall [4], equation 1.1, and N.J. Petch [5], equation 1.2, produced results that showed the magnitude of both properties is dependent on the inverse square root of the grain size. This trend of an increase in strength with decreasing grain size has come to be known as the Hall-Petch effect and, over the years, has been observed for many metals [6]. Equation 1.3 is the common expression for this effect, where σ_y is the yield stress, σ_o is the lattice friction in Pascals, $k_{H\text{-}P}$ is the Hall-Petch coefficient, and d is the grain size.

$$(\sigma_{LYP} - \sigma) \propto 1/d^{1/2} \qquad \text{equation 1.1}$$

$$\sigma_c = \sigma_o + k\ell^{-1/2} \qquad \text{equation 1.2}$$

$$\sigma_y = \sigma_o + k_{H-P} d^{-1/2} \qquad \text{equation 1.3}$$

A mechanism explaining this effect starts with production of dislocations inside grains. These dislocations propagate along their preferred crystallographic directions, eventually stop at a grain boundary but cannot cross the grain boundary due to misorientation between the adjacent grains. Dislocations continue to pile-up at the boundary until the applied stress becomes large enough to cause macroscopic yielding by either dislocation emission from the grain boundary into or activation of another source in the adjacent grain. As the grain size decreases the number of boundaries increases, stopping the dislocations more frequently and needing a higher stress to continue plastic deformation.

1.2 BCC metals

The focus of this dissertation is on the mechanical behavior of body center cubic (BCC) metals with small grain sizes. On the periodic table, these metals are mainly group V and VI elements such as W, Ta, Nb, Cr, Mo, and V. They are often referred to as refractory metals because of their high strength and melting point, which makes them attractive for many applications. In coarse grain BCC metals at relatively low homologous temperatures, dislocation motion is dominated by the screw ones with Burgers vector, $\mathbf{b} = a_o \langle 111 \rangle /2$, where a_o is the lattice parameter. The core of such screws lies on either the $\{110\}, \{321\}$, or $\{211\}$ planes, rendering a 3-dimensional core that has to be contracted prior to dislocation glide. The rate controlling mechanism for dislocation motion in BCC metals is then the formation of kink pairs via cross-slip of screw

dislocations. This mechanism is schematically illustrated in FIGURE 1.1, where a screw dislocation starts in a Peierls valley [7], then a kink-pair forms via cross slip across to the next valley, and finally the kinks propagate along the dislocation line until the entire dislocation has moved to the neighboring valley [8]. This mechanism has been shown to be temperature and strain rate dependent, which makes the flow strength of BCC metals also temperature and strain rate dependent. As the temperature gets lower or strain rate increases, the flow stress gets higher [9, 10]. The influences from these properties of BCC metals stay relevant even when the grain size is reduced into the nanometer range.

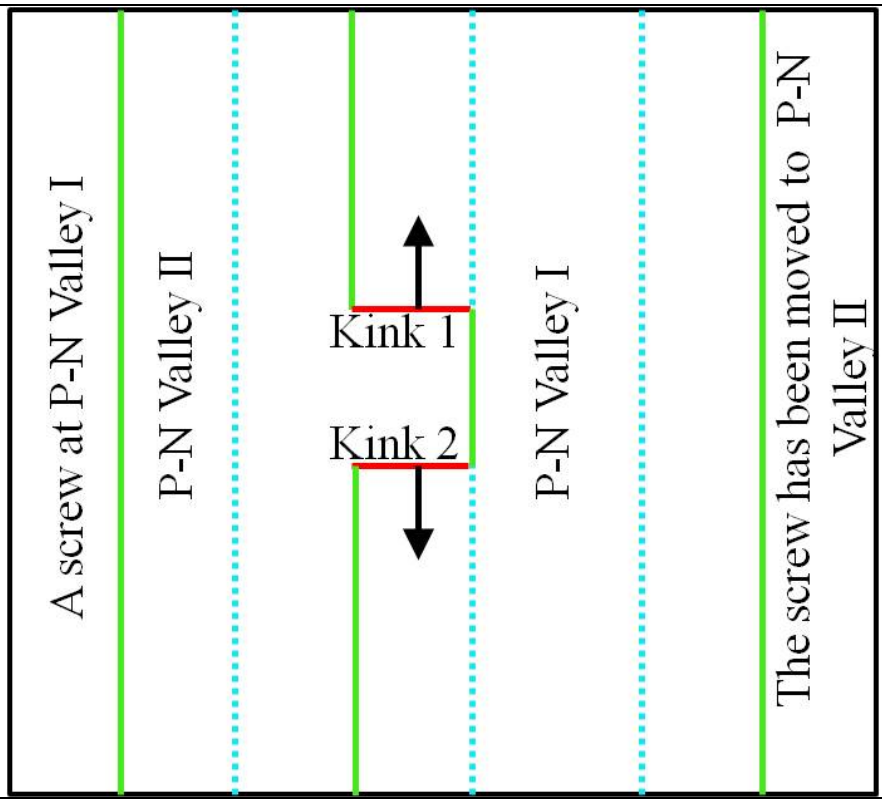

FIGURE 1.1: Schematic of the kink-pair mechanism active in BCC metals that occurs by the cross-slip of screw dislocations across Peierls valleys. [11]

1.3 Grain Refinement Techniques

1.3.1 Bottom-up

Grain refinement is accomplished through a variety of techniques, but here the focus will be on methods that are able to achieve grain sizes in the ultra-fine grained (UFG) and nanocrystalline (NC) regimes. These two regimes cover a large range of grain sizes. UFG materials have a grain size between 1000-100 nm, while NC corresponds to those with grains below 100 nm. There are two broad methods researchers take when refining into either regime. The first is considered bottom-up, where bulk materials are created through the assembly of atoms or powders. Techniques such as inert gas condensation (IGC) [12], electro-deposition (ED) [13, 14], and ball milling followed by consolidation[15] fall into this category. An advantage to these techniques is the possibility to create materials with small grains, below 50 nm, well within the NC regime. Such small grains have been uncovered to have a variety of exceptional and unexpected mechanical properties, as will be discussed later. However, the disadvantage of using these techniques is the small volumes of material produced, along with being susceptible to contamination, and the porosity that exists after processing.

1.3.2 Top-down

The second broad method for grain refinement is known as top-down, where the grain size is reduced by introducing large amounts of plastic strain into a bulk starting material [16]. Because of the large plastic deformation that occurs, these methods are more commonly referred to as severe plastic deformation (SPD) processes [17]. The high strains attained during such processes are capable of refining grains easily into the UFG regime and certain techniques can now reach NC grain sizes, depending both on the specific technique and the material processed. According to Valiev, Islamgaliev, and

Alexandrov [17], to be considered as an SPD process several requirements must be met. The obtained grain structure must: i) have a large distribution of high angle grain boundaries, ii) be uniform throughout the whole sample volume, and iii) contain no damage or cracks. As will be shown later, to account for the final requirement these techniques are usually performed under a high hydrostatic pressure.

A few examples of SPD techniques include accumulative roll bonding (ARB) [18, 19], multiple forging[20], equal channel angular pressing (ECAP)[21], and high pressure torsion (HPT) [22, 23]. Diagrams of ARB, multiple forging, and ECAP are shown in FIGURE 1.2a, FIGURE 1.2b, and FIGURE 1.2c, respectively. ARB processing, FIGURE 1.2a, involves the successive roll-bonding of the same work piece to accumulate strain in the sample and therefore reduces the grain size [18]. This process has the advantage of avoiding the expensive dies such as needed in ECAP or HPT and while most studies are only able to attain grain size in the UFG regime, though some recent papers reported NC grains in ARB Cu [24]. Carpenter et al. have also used ARB to produce Cu-Nb multilayer samples with a layer thickness of 9.0 nm [25]. Multiple forging (MF) is a process similar to open free forging, a schematic of which is shown in FIGURE 1.2b [20]. Here the work piece is compressed along alternating directions while at temperatures of 0.1 – 0.5 T_m, where T_m (K) is the melting temperature.

While the two previous techniques are capable of significant grain refinement, one of the most studied SPD methods is ECAP [21, 26]. Shown in FIGURE 1.2c, a test piece is forced through two channels of identical cross-section that are at an angle, φ, from each other. The amount of strain the test piece undergoes during one pass, $\Delta\varepsilon_i$, depends on this angle and can be calculated by equation 1.4 [26].

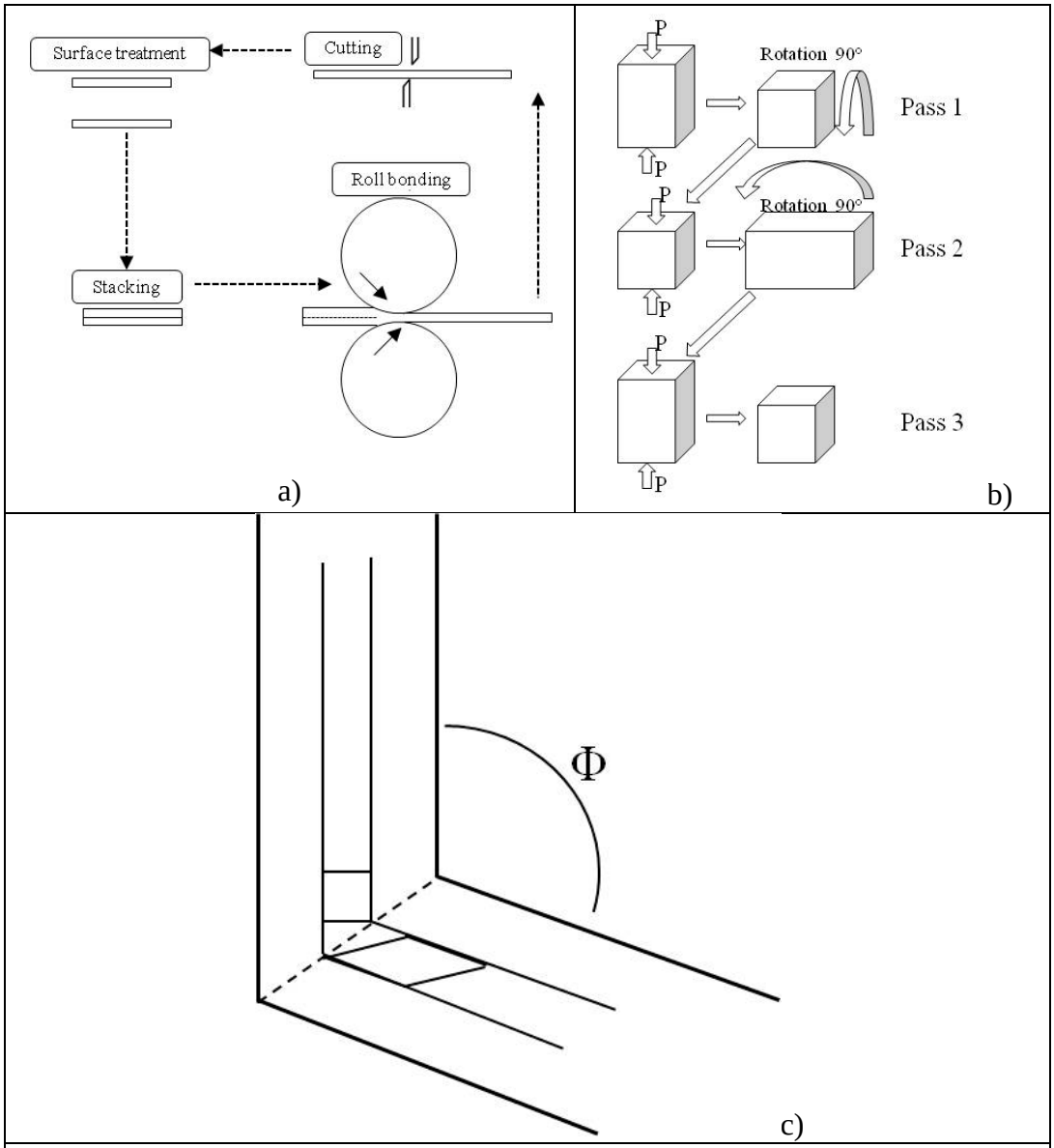

FIGURE 1.2: Illustrations of some typical SPD grain refinement techniques including (a) accumulative roll bonding [18], (b) multiple forging [20], and (c) equal channel angular pressing [26]. All of these techniques involve inducing large amounts of strain into bulk samples.

$$\Delta\varepsilon_i = 2/\sqrt{3} \times cot(\Phi/2) \qquad \text{equation 1.4}$$

For channels that have Φ = 90°, a single pass equals a strain of ~1.15. The total amount of strain, ε_{tot}, is given as $\varepsilon_{tot} = N \cdot \Delta\varepsilon_i$, where N is the number of passes. The resulting microstructure not only depends on the die angle but also on the orientation of the work piece, and different ECAP routes have been developed over the years, all involving rotation of the work piece between consecutive passes [27, 28]. A few typical routes include: no sample rotation between consecutive passes, a 90° rotation about the longitudinal axis between consecutive passes, and a 180° rotation about the longitudinal axis between consecutive passes. The shear plane during deformation changes depending on the route and will result in different final microstructures [28].

1.3.3 High Pressure Torsion

While all these techniques are capable of refining the grain size of bulk metals, for this work HPT is the method of choice. The HPT process involves a combination of high hydrostatic pressure with torsional strain and has its origins in the studies by Bridgman, who discovered that [29];

> "If a bar is twisted while a longitudinal compressive load is simultaneously applied it is possible to twist the bar through much greater angles without fracture than is possible without the compressive load."

In this work he found that steel samples with applied compressive stresses between 225 – 560 MPa showed a doubling of the shear strain and a 50% increase in maximum shear stress, when compared to samples with zero compressive stress. An illustration of the modern HPT set-up is shown in FIGURE 1.3 [30]. A sample ~10 mm in diameter and 1-2 mm thick is positioned between two anvils, which help in achieving the hydrostatic

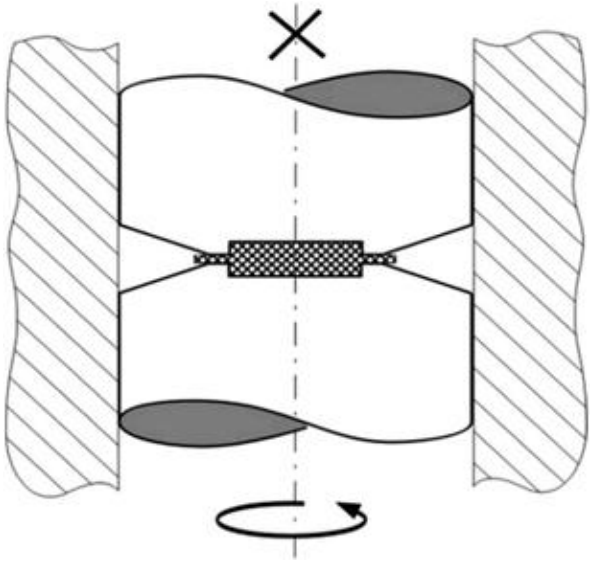

FIGURE 1.3: Schematic of the modern HPT set-up, consisting of two opposing anvils which apply a high pressure and torsion strain to a disk shaped sample. [30]

pressure needed through either an unconstrained or constrained design [31]. For the constrained set-up, the disk sample is placed into an inset on the anvil surface and the walls of the inset apply a hydrostatic pressure on the deforming sample, which prevents the sample from fracturing. The unconstrained method leaves a gap in between the two anvils so that during deformation a small amount of material is extruded from the sample edge. This excess material is no longer being deformed and produces a hydrostatic pressure through back stress acting on the disk. The mechanism for grain refinement during HPT first involves an increase in the number of dislocations that occurs during the initial straining. These dislocations form into cell walls that begin to decrease in width due to annihilation of dislocations with opposite Burgers vectors. Following this annihilation, an excess of dislocations with similar Burgers vectors will remain at the cell wall to form the new grain boundary and smaller grains.

The limit of grain refinement with SPD techniques is related to dynamic recrystallization, which occurs at temperatures, $T_{RX} = 0.4T_M$, where $T_M(K)$ is the melting point of the metal. For example, an FCC metal like Cu has a melting point of 1358 K, making T_{RX} ~407 K, which is close to room temperature. This means that it is likely that the refined grains following SPD processing can go through dynamic recrystallization and even grow at room temperature. In contrast, a refractory metal such as Ta has a melting point of 3290 K, making the T_{RX} value much higher (987 K). This means that grain refinement in Ta following HPT is more stable and capable of maintaining the smaller grain size at room temperature.

High pressure torsion has also been found useful in “bottom-up” NC metal processing as the means for powder compaction. Edalati et al. report on their use of HPT to consolidate NC W and nanocomposites of W/Al, W/Ni and W/Ti, each with grain sizes ~10 nm [32]. This technique enables them to produce nanocomposites with Vickers microhardness ~900 Hv, yet without forming any intermetallic phases between the species. Also, as will be shown later, there is dependence on the induced strain with radial position. This means that materials processed through HPT will contain a grain size gradient within the disk. If it is possible to fabricate specimens at specific radial positions, then mechanical testing of a metal with varying grain sizes can be done by only using one processed sample. While there are some reports of increasing the size of HPT disk samples up to 20 mm in diameter [33], the current HPT processing technology still only produces small volumes of total material. Any samples cut from an HPT disk will either contain a gradient in grain sizes or only millimeters in size and thus too small for

any conventional mechanical testing techniques. This problem can be overcome by utilizing small scale mechanical testing, which will be introduced later.

1.4 UFG/NC Metals

Before discussing small scale testing techniques, one must understand why investigating the mechanical properties of metals with such small grain sizes is of any interest.

1.4.1 Structure

FIGURE 1.4 and FIGURE 1.5 show bright field TEM images and diffraction patterns of the grain structure for metals processed through bottom-up and top-down methods respectively. The grains from ball milled Cu, FIGURE 1.4a [34], have a grain size below 100 nm and the continuous rings in the diffraction pattern show no preferential orientation. Plane view micrographs of electrodeposited Ni, FIGURE 1.4b [35], show an equiaxed grain structure with sizes on the order of 30 nm and also no preferential texture. However, when cross sectional TEM specimens were made from the same samples they showed a columnar structure. The final image, FIGURE 1.4c [36], shows iron nanoparticles fabricated by inert gas condensation. Although this technique is capable of creating particles smaller than 10 nm, most literature reports have used it for producing nanoparticles, not bulk, large volume NC metals. Overall these methods are capable of producing small grains but in small volumes and most such products have a density that is lower than the bulk and fully dense metal. This lower density has a detrimental effect on the NC metals' mechanical properties.

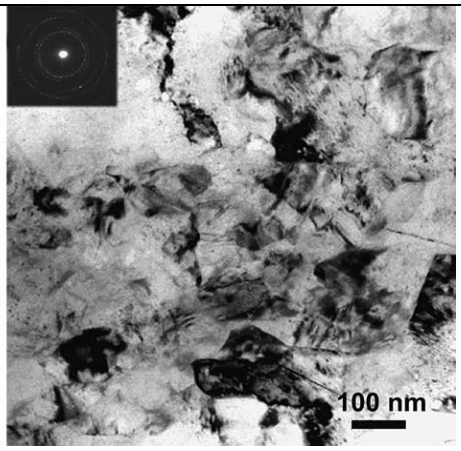

a)

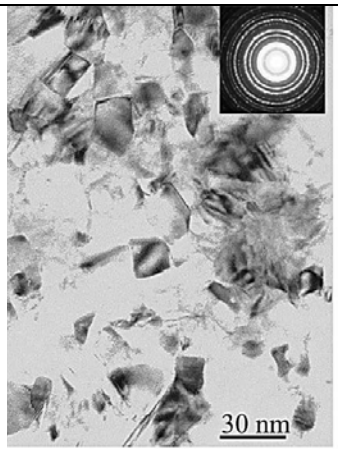

b)

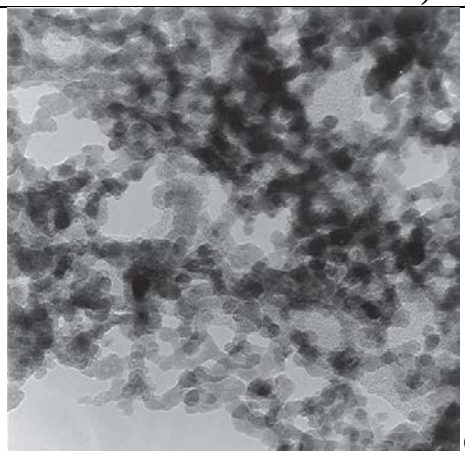

c)

FIGURE 1.4: TEM bright field images showing the grain structure of different bottom-up refinement processes including (a) ball milled Cu [34], (b) Ni by electrodeposition [35], and (c) iron by inert gas condensation [36]. All techniques are capable of fabricating materials with a grain structure well within the NC regime. However this is limited to small total volumes with lower density.

The TEM images in FIGURE 1.5a-d show the grain structure following some common top-down processing methods. One of the most noticeable differences, when compared to the microstructures produced by the previous bottom-up techniques, is that the grain size is larger. The bright field TEM image, FIGURE 1.5a [19], of grains produced by ARB show an equiaxed shape on the order of 500 nm. While individual grains can be observed in this image, the corresponding diffraction pattern shows only individual spots instead of continuous rings. This suggests that the resulting microstructure maintains some texture as a result of ARB, not surprising as it is well documented that rolling processes create specific deformation texture. The image in FIGURE 1.5b shows an equiaxed grain structure following the multiple forging and while the scale bar is 250 nm the grain size appears to be similar to or just slightly smaller than that from ARB [37]. After ECAP processing, FIGURE 1.5c, the grains show an elongated shape where the maximum and minimum diameter of the grains are on the order of hundreds of nanometers [38]. Also, the diffraction pattern shows more individual spots than continuous rings, similar to ARB, again suggesting a deformation texture. For HPT, FIGURE 1.5d [39], while the grains also display an elongated shape on the order of ~500 nm, the transverse diameter of these grains is at or below the transition size for the NC regime. Also, unlike the previous techniques, the diffraction pattern here shows continuous rings, suggesting many small, randomly oriented grains.

1.4.2 Mechanical Behavior

The most notable change in the mechanical behavior of an UFG/NC metal compared to coarse grain metals is the increase in strength due to the Hall-Petch effect [6]. As shown in FIGURE 1.6a, as the grain size for iron decreases from 20000 nm to

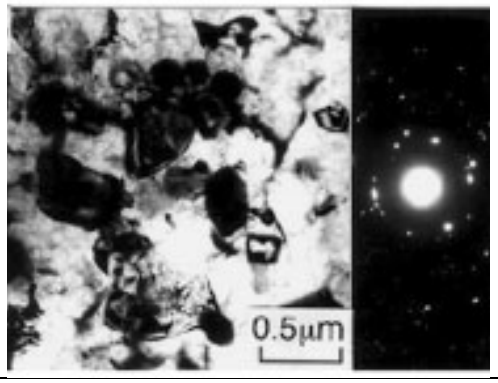

a)

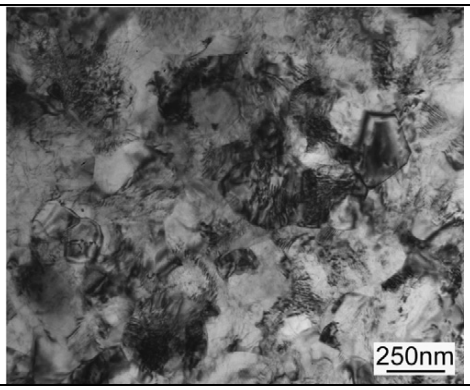

b)

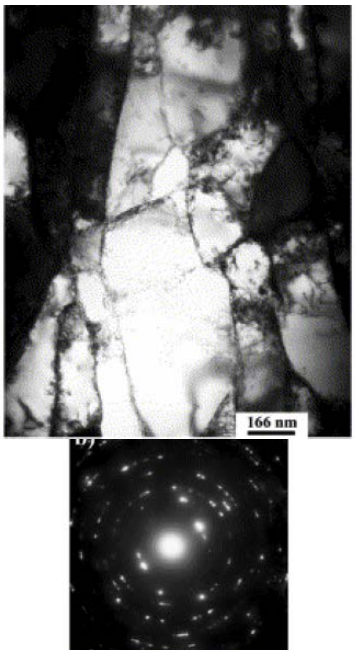

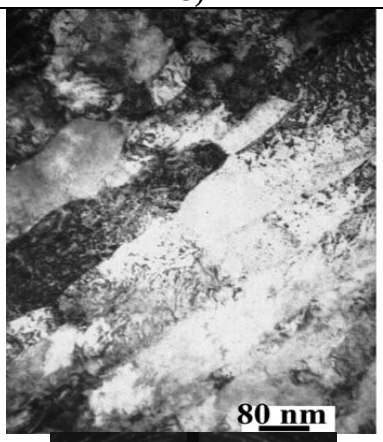

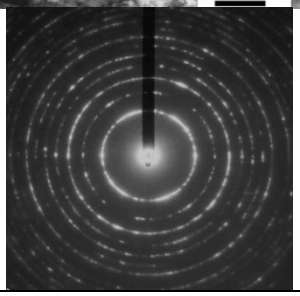

c)

d)

FIGURE 1.5: TEM bright field images showing the grain structure of different top-down refinement processes including (a) ARB [19] (b) multiple forging [35, 37], (c) equal channel angular pressing [38], and high pressure torsion [39]. Grain structure with these techniques show large grain sizes and high angle grain boundaries.

80 nm there is roughly a tenfold increase in the strength [40]. Such high strengths make NC materials extremely attractive for many engineering applications, but as will be shown later there are other unexpected changes in mechanical properties that would hinder some applications. One of these unexpected changes is the transition to an inverse Hall-Petch effect, or decrease in strength with decreasing grain size. As shown in

FIGURE 1.6b, once the grain size for Cu and Pd reached ~ 30 nm the strength begins to decrease [41]. This has been attributed to changes in the deformation processes from dislocation based motion to grain boundary mediated processes.

There are a few other effects an UFG/NC grain size has on the mechanical properties of a metal. These include a reduction in strain hardening during plastic deformation, a loss of ductility, and changes in the strain rate sensitivity (SRS). In coarse grain metals, following the yield point there is a period of increasing stress with increasing strain, and this response is referred to as strain hardening and is due to the multiplication and interaction of dislocations. In a coarse grain metal dislocation multiplication is due to the activation of Frank-Read (F-R) sources [42], where the maximum shear stress (τ_{max}) needed to activate the source is directly proportional to the shear modulus (G) and Burgers vector (b), but inversely proportional to the distance ($2R$) between the pinning points by equation 1.5. As these dislocations move they interact with each other and, when the dislocation density gets high, they impede each other.

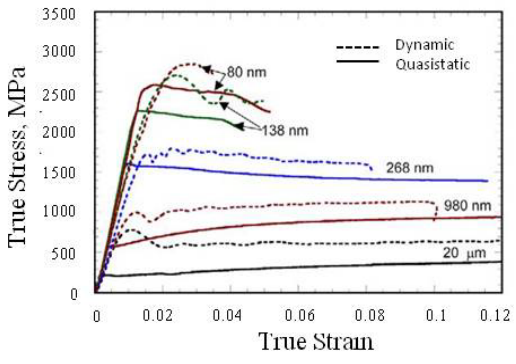

a) b)

FIGURE 1.6: Plots showing the effect of smaller grain size on the strength where the (a) Hall-Petch effect is dominated in the UFG and larger NC regime and the (b) Inverse Hall-Petch effect that dominates at small grains[40, 41].

Once this happens a higher stress is needed to allow the plastic deformation to continue. The rate of this change in stress during plastic deformation is referred to as the strain hardening exponent (n), which is defined in the Holloman equation, equation 1.6, and is usually less than unity. The strain hardening behavior is the mechanism responsible for the cold work strengthening mentioned previously.

$$\tau_{max} = \frac{Gb}{R} \qquad \text{equation 1.5}$$

$$\sigma = K\varepsilon^{n} \qquad \text{equation 1.6}$$

For metals with grain sizes in the UFG/NC regime there is reduced or no strain hardening observed during a tension or compression test, and we can classify these metals as elastic-perfectly plastic. Essentially the exponent $n = 0$ for these materials and has been seen during testing of the most common metal crystal structures, face-center cubic (FCC) [34], BCC [43], and hexagonal close packed (HCP) [44] metals as shown in FIGURE 1.7a, b, and c, respectively. The explanation for this behavior is that the small grains present in these metals do not allow for the large dislocation density needed to impede dislocation motion. As the grains get smaller there is less space for the pinning points inside a single grain, causing the stress needed to activate an F-R source to increase to near the theoretical shear strength of a perfect crystal. Since these stress values are not reached, F-R sources are thought not to be active in these metals. Instead, the mechanism of dislocation multiplication in NC metals is emission and absorption at grain boundaries [45]. Dislocations emitted from grain boundary ledges or triple junctions travel across the grain interior and are then absorbed into the opposite grain boundary. Since few dislocations exist inside such tiny grains there is no opportunity for them to build up and in turn we see much reduced strain hardening. Unfortunately, the

downside of reduced strain hardening in NC metals is the reduction in the amount of plastic deformation the material can withstand. This results in a drastic reduction in the ductility of UFG/NC metals, as shown in FIGURE 1.8a [46] and b [47]. These plots show that the percent tensile elongation of these metals is less than 5.0%. This can also be seen in the stress vs. strain plots in FIGURE 1.6a, where for grain size of 20 μm the maximum compressive strain reaches over 12% but for 80 nm grains the maximum compressive strain is only ~ 5.0%. Such a reduction in ductility or malleability is detrimental to many

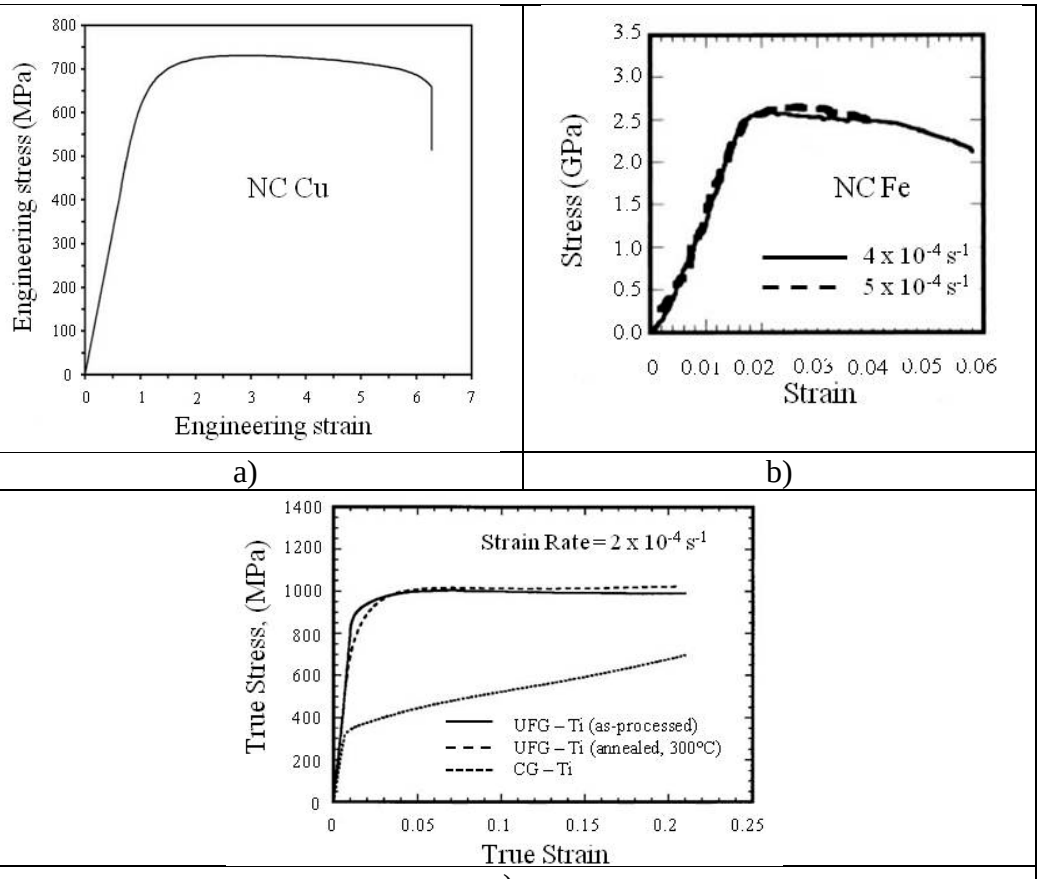

FIGURE 1.7: Examples of the strain hardening observed in NC metals with FCC (a) [34], BCC (b) [43], and HCP (c) [44]structure. The reduced strain hardening seen in NC metals is due to the lack of dislocation build-up inside the grains, instead dislocations are emitted and absorbed at grain boundaries.

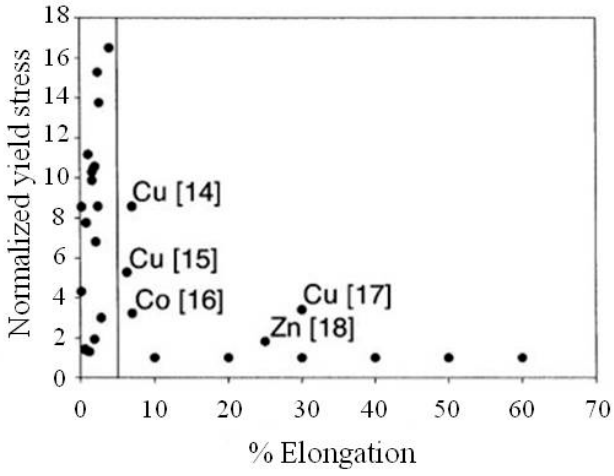

a)

Specimen	d (nm) Sol./Sub.	Total Elongation (%)
As-deposited	251/174	1.5, 1.8
Depos., 100°C	246/202	1.9, 3.9
Depos., 150°C	323/273	6.7, 5.1
As-rolled	133	5.5
As-rolled, 100°C	-	5.8
As-rolled, 150°C	152	7.1
As-rolled, 425°C	>1000	36.6

b)

FIGURE 1.8: (a) Plot showing the reduced ductility present in NC metals, where the % elongation is mainly below 5% for grain sizes in the UFG/NC regime [46]. (b) This graph shows the grain size values and total elongation for ED Cu, reaffirming the reduced ductility for small grain sizes [47].

possible applications that are attractive for NC metals. Koch et al. attributed the loss of ductility to three main aspects of NC metals [46, 48]. The first is the presence of artifacts due to processing, such as porosity or weakly bonded particles. These artifacts are all possible when the materials are processed through bottom-up refinement techniques. The next two reasons Koch also attributes to loss of ductility are directly related to the reduced strain hardening; these being force instability in tension and crack nucleation/propagation instability. Force instability refers to the formation of a neck during tensile plastic deformation which occurs at the early stage of tensile straining for

NC metals, which entails premature failure of the tensile specimen. Crack instability occurs because of the lack of a build-up of dislocations near the crack tip, which in coarse grain metals would act to blunt the crack tip and slow down its propagation. In order to take advantage of the increased strength of NC metals the ductility needs to be improved before these metals could be used in any structural applications.

Current research into improving the ductility of NC metals is taking several routes. One method is to process the material so that there is a second ductile phase. Zimmerman et al. improved the ductility of NC Ni through the addition of a SiC second phase [49]. Comparing pure NC Ni to NC Ni-(0.7 vol%) SiC with a grain size of ~14 nm shows that the pure Ni had only 0.22% elongation while the Ni-SiC specimen increased to ~3.40%. A second method is to have a material with a bimodal grain size, where dispersed throughout the small NC grains are larger "coarse" sized grains. Through cold rolling at liquid N_2 temperatures and annealing up to 200°C for different periods of time, Wang et al. were able to increase the strength of Cu by ~300 MPa while still maintaining

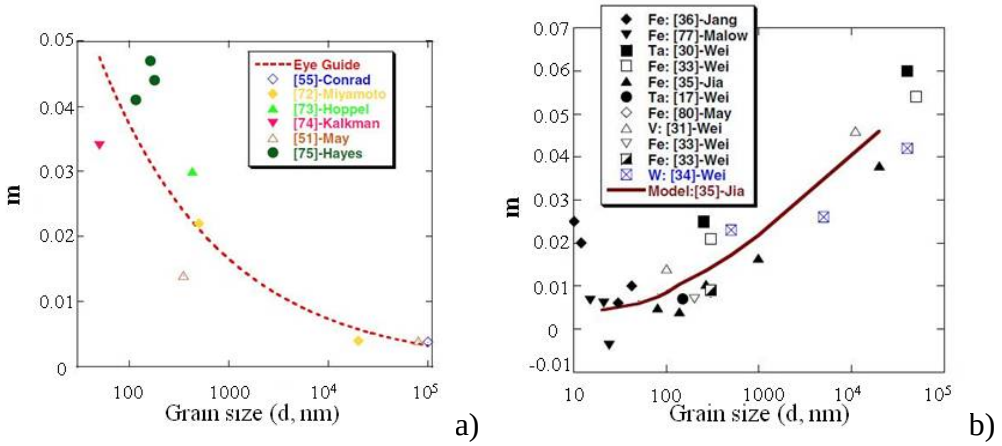

FIGURE 1.9: Plots of the SRS vs. grain size for (a) FCC and (b) BCC metals, where the values increase for FCC and decrease for BCC. This change in SRS is due to changes in the rate controlling mechanisms as the grain size decreases. [11]

30% uniform elongation [50]. The samples with such good combination of strength and ductility showed that the majority of the grains are still in the NC regime but a volume fraction of 25% were large grains (d >1.0 μm). Lu et al. also achieved strengths of 900 MPa for Cu with an average grain size of 400 nm but still maintained 13% elongation-to-failure by introducing nanoscale growth twins [51].

The strain rate sensitivity (SRS, m), a measure of the dependence of the material's strength on the strain rate, is proportional to the Boltzmann's constant (k), and temperature ($T(\mathrm{K})$) and inversely proportional to the shear stress (τ) and activation volume (v^*) required for a specific plastic deformation mechanism, equation 1.7.

$$m = \frac{kT}{\tau \cdot v^*} \qquad \text{equation 1.7}$$

This material property is also affected by a change in the grain size [11, 52]. The plot in FIGURE 1.9a shows that the strain rate sensitivity of Al increases as the grain size decreases into the UFG/NC regimes, a trend that has also been observed for other FCC metals such as copper and nickel [11]. For BCC metals like Fe, Ta, and W, FIGURE 1.9b, the opposite trend is observed [11].

For coarse grain FCC metals the rate controlling plastic mechanisms are cutting of forest dislocations and cross slip, making the length spanned by an active dislocation segment (ℓ) proportional to the spacing between forest dislocations, which scales inversely with the forest density. As the grain size is reduced however, the forest dislocation spacing within a single grain gets smaller, meaning the length (ℓ) transitions to being proportional to the grain size. The activation volume is also directly proportional to this length (ℓ), so as this length decreases the SRS will increase. Therefore the increase in SRS values for FCC metals is related to the length scale necessary for plastic

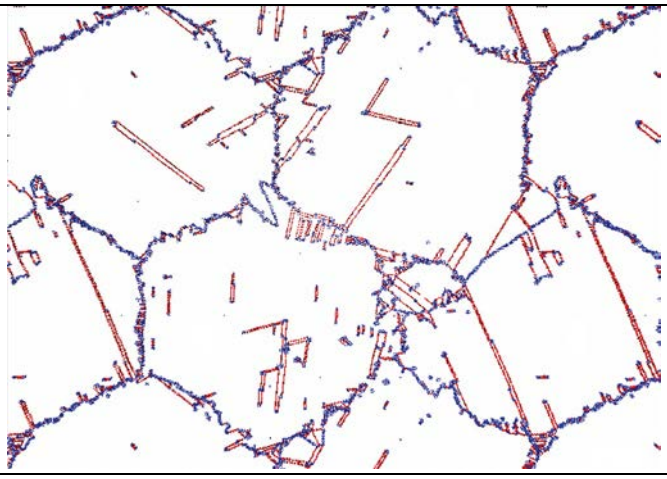

a)

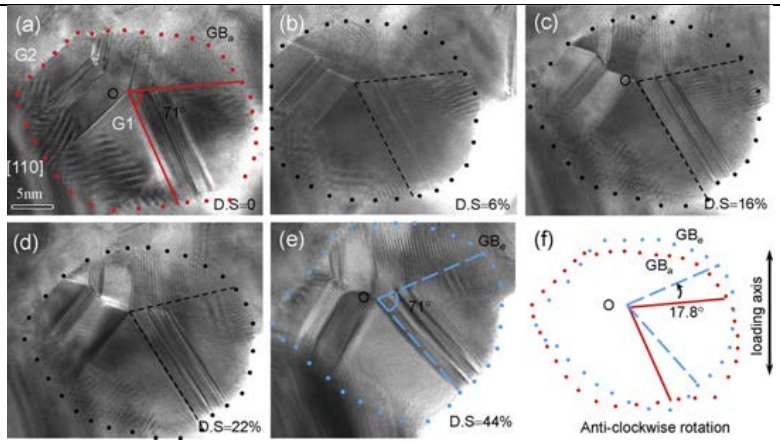

b)

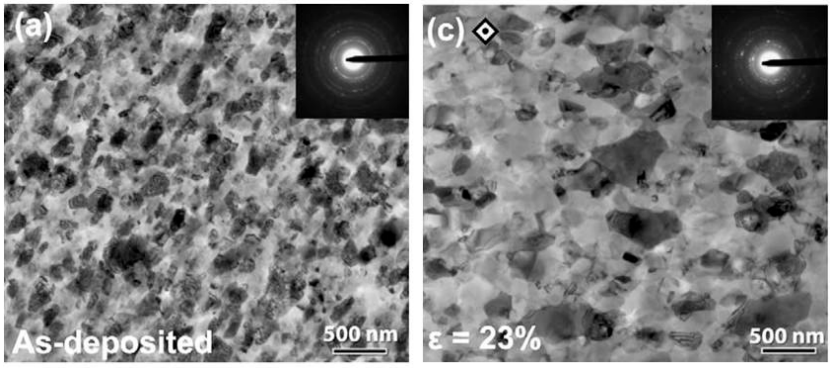

c)

FIGURE 1.10: Images of some of the different deformation mechanisms observed in NC metals, (a) the emission/absorption of dislocations at grain boundaries (through molecular dynamics (MD) simulations) [45], (b) grain rotation under tension as observed within a TEM [56], and (c) coupled grain boundary motion or stress-driven grain growth as observed by TEM [57]. The mechanism in (a) is thought to dominate at UFG and larger NC sizes while the other mechanisms dominate at the smallest grain sizes.

deformation being proportional to the grain size in the UFG/NC regime. For BCC metals, as was mentioned previously, the rate controlling mechanism is the nucleation of kink pairs. Due to the decrease in the width between each kink, at coarse grain sizes the activation volume has been shown to decrease and SRS increases with increasing stress [53, 54]. Due to the Hall-Petch effect, a reduced grain size is translated to an increase in the flow stress, therefore the decrease of SRS in BCC metals is due to the increase in flow stress from grain boundary strengthening.

1.4.3 Deformation Mechanisms

Since the SRS is changing with grain size, there is a chance for the deformation mode of NC metals to change as well [55]. The motion of dislocations in NC metals has been discussed previously, that is, the emission and absorption at grain boundaries, shown in FIGURE 1.10a, where the red lines represent dislocations, partials, or twins in NC Al (45 nm) after ~12% strain [45]. It can be seen that some of these defects originate at a boundary and travel across the grain to be absorbed by another boundary. When the grain size is reduced down to 30 – 20 nm, changes in the deformation behavior have been observed. Mainly, grain boundary mediated deformation processes begin to dominate over the classic dislocation mechanisms, resulting in the inverse Hall-Petch effect, a decrease in strength with decreasing grain size, as mentioned previously [58]. These grain boundary processes include sliding [59], rotation [56], and migration [57, 60]. An example of grain rotation is shown in FIGURE 1.10b, where thin gold films with grain size ~ 20 nm were pulled in tension while being imaged with a TEM [56]. After a total displacement strain of 44% the grain underwent a 17.8° counter-clockwise rotation. The authors suggest that wedge-disclination dipoles [61] were responsible for the rotation but

did not have statistically sufficient information to prove this concept. Another mechanism observed in NC grains is shown in FIGURE 1.10c, where Al thin films with an original grain size of 20 nm increased to 33 nm after 23% strain [57]. The growth is attributed to stress-coupled grain boundary migration, where a tangential shear stress acting on the boundary causes a coupling between the two grains, moving the boundary in the normal direction [62]. As a result one grain begins to grow while the other shrinks in size. While the motion of dislocations in UFG/NC metals is now a widely accepted mechanism, there is still debate over the dominating plastic mechanism at the smallest grain sizes.

1.5 NC BCC Metals

The mechanical properties for NC metals discussed previously have been investigated primarily by testing on FCC metals, while fewer reports have been concentrated on metals with BCC structures. There is an interest in NC BCC metals however, stemming from their behavior under dynamic strain rates, mainly their capacity to deform via adiabatic shear bands (ASBs) [63]. These bands of localized regions of extreme plastic deformation and have been observed in UFG/NC W [39, 64], Ta [65, 66], Fe [67], and V[68], FIGURE 1.11 . Their increased propensity to deform in this manner is explained through Wright's criterion for the formation of ASBs, shown in equation 1.8 [69, 70]. In this equation, χ_{ASB} is the susceptibility of a material to deformation via ASBs and depends on material parameters such as strain hardening exponent (n), strain rate sensitivity (m), and thermal softening ($a = (-\partial\sigma/\partial T)/\rho c$), where σ is the flow stress, T is the temperature, ρ is the density and c is the specific heat. The higher the value of χ_{ASB} the more likely the material will deform via ASBs. For NC materials, $n \sim 0$, so

equation 1.8 can be reduced to equation 1.9, where now the thermal softening is, $\lambda = -(1/\hat{\sigma}_o)(\partial\sigma/\partial T)$, and the density and specific heat are constant with grain size. As mentioned previously, the SRS changes with grain size, specifically for bcc metals it decreases with smaller grain sizes [11]. This decrease in SRS means the susceptibility will increase with decreasing grain size and the material will deform via ASBs at high strain rates [11].

$$\frac{\chi_{ASB}}{a/m} = min\left\{1, \frac{1}{(n/m)+\sqrt{n/m}}\right\} \qquad \text{equation 1.8}$$

$$\chi_{ASB} = \frac{a}{m} = \frac{\lambda\sigma_s}{\rho c m} \qquad \text{equation 1.9}$$

The advantage of a material forming ASBs is the improved performance of kinetic energy (KE) penetrators. Currently, KE penetrators are made of Depleted Uranium (DU) or Tungsten Heavy Alloy (WHA). However, KE penetrators made from

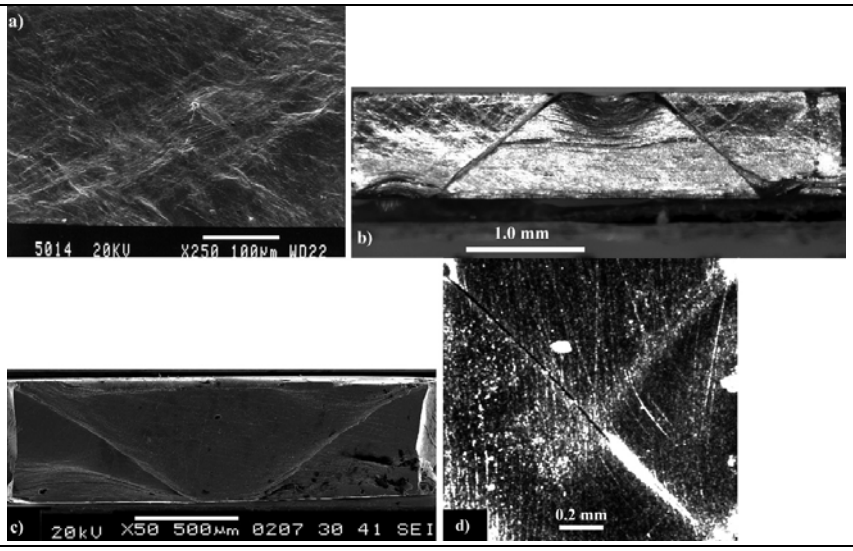

FIGURE 1.11: SEM micrographs of BCC metals after dynamic compression, showing the deformation mode is through formation of adiabatic shear bands. This deformation behavior is attributed to the combination of increase in strength and decrease in both strain hardening and strain rate sensitivity. [63]

DU produce deeper, narrower penetration channels in the target and therefore possess a superior performance over WHA penetrators [71]. This is due to the formation of ASBs in DU penetrators compared to the uniform deformation seen in WHAs. Although DU shows the improved performance there is an effort to find a replacement material to avoid the use of uranium for environmental concerns as explosives of DU are toxic. The ASBs observed in NC BCC metals make them attractive as a replacement for DU. However, for this purpose the poor ductility of NC metals should first be addressed. Materials used in KE penetrators need to retain certain level of ductility to survive the initial launch conditions [70]. So the quasi-static tensile behavior of NC BCC metals must be known if they are to be considered a useful replacement material. At this time no studies about their quasi-static compressive/tensile behavior are known.

Previous reports on the quasi-static testing of NC BCC metals do show the formation of shear bands, although not considered ASBs. Early work by Malow, Koch,

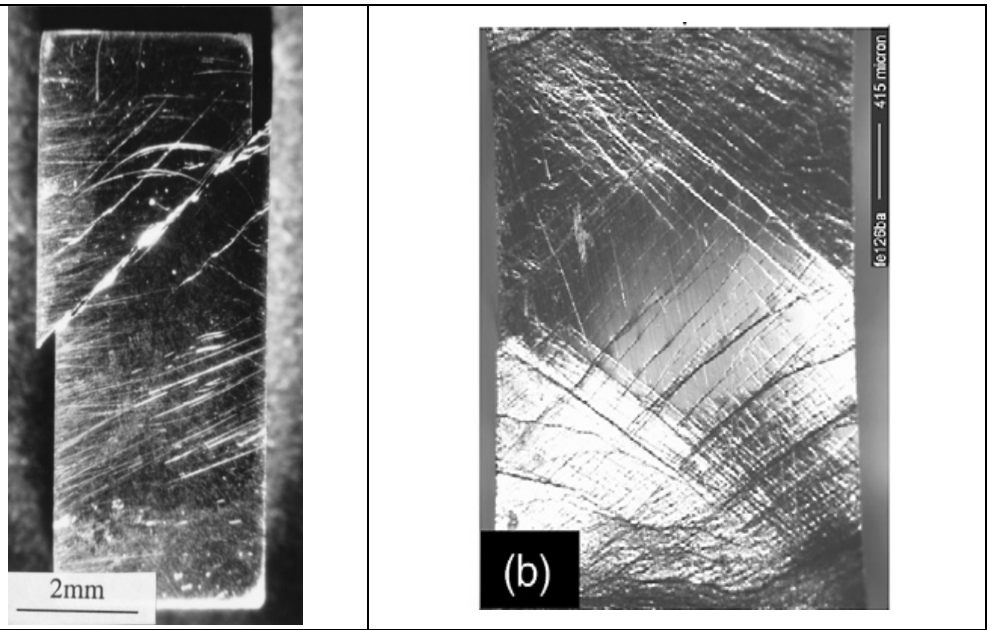

a b

FIGURE 1.12: Optical micrographs showing formation of shear bands in an (a) Fe-Cu alloy [73] and (b) NC Fe specimen under quasi-static strain rates. [40]

Miraglia, and Murty observed quasi-static shear bands in NC Fe, with grain size d = 15-24 nm, processed via mechanical attrition and compaction and tested using automated ball indentation [72]. At the same time, Carsley, Fisher, Milligan, and Aifantis showed quasi-static shear bands in an Fe-10%Cu alloy as well, but the grain sizes here varied from 1.7 μm to 45 nm, FIGURE 1.12a [73]. The author noted that the macroscopic behavior of this alloy was similar to that of metallic glasses but these similarities did not carry to the microscopic level. Although no definitive reason was given for why this material should deform in such a manner it was stated that the free volume at the grain boundaries could be the controlling factor. Another report obtained shear bands for ball milled and consolidated Fe, and the transition to shear band formation occurs once d < 300 nm, FIGURE 1.12b [40]. Transmission electron microscope images show a well-defined band with elongated, textured grains, leading to the proposed deformation mechanism of initial yielding in a large grain followed by rotation of near-by grains [67]. Trelewicz and Schuh also observed quasi-static shear bands in a Ni-W alloy but only at d = 3 nm, which they attribute to arriving at the amorphous limit, causing the metal to behave like a metallic glass [74].

1.6 Focused Ion Beam

The work presented in this dissertation is done solely on HPT processed BCC metals and, as mentioned previously, this SPD technique yields a small volume of material containing a grain size gradient. In order to take advantage of this gradient, mechanical tests must be done on small sample volumes at site specific locations. Techniques such as micro-electro-discharge machining (μ-EDM) are capable of producing specimens on the order of millimeters by melting away the unwanted material

which leaves a rough and undesirable surface on the specimen. To fabricate micrometer sized specimens at site-specific locations, the most effective instrument for fabrication is a focused ion beam (FIB) microscope [75].

1.6.1 Introduction

The use of the FIB as a valuable piece of instrumentation has grown in recent years to include applications like IC circuit repair, TEM lamella preparation, and micromachining [76, 77]. From the outside a FIB looks similar to a conventional scanning electron microscope (SEM), but instead of accelerating a beam of electrons, a FIB uses ions. The increased mass of Ga ions, compared to electrons, means they can be used not only for imaging but also milling of surfaces by means of sputtering. An image of an FEI Nova Nanolab Dual Beam, the microscope used for this work, is shown in FIGURE 1.13. As indicated in the figure, this dual beam instrument combines an SEM

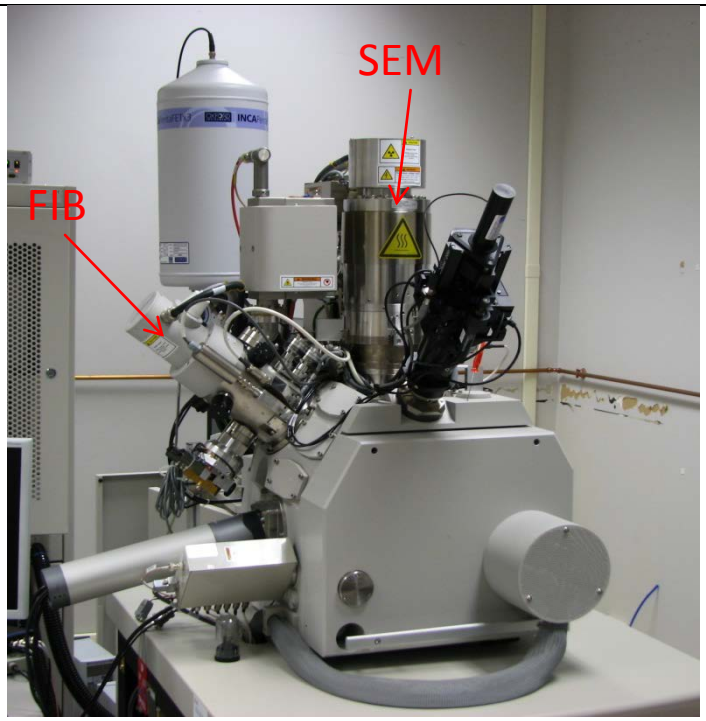

FIGURE 1.13: Image of an FEI NOVA Nanolab Dual Beam FIB, where the electron column is vertical and the ion column is positioned at 52°.

and FIB into one machine. The SEM column is oriented vertical with respect to the specimen stage while the FIB column is positioned at 52° off this vertical direction. Adding the SEM allows imaging of the sample by a method that will not cause damage to the surface of the specimen like the FIB does.

1.6.2 Liquid metal ion source (LMIS)

As mentioned previously, the FIB utilizes an accelerated beam of ions instead of electrons. The most common method for producing an ion beam is through the use of a liquid metal ion source (LMIS). It consists of a filament (substrate), usually made of tungsten, and a reservoir that holds the metal source material [78]. Possible source materials include Bi, In, Sn, or Au, As, and B alloys, but the most commonly used species is Ga because it has a low vapor pressure at its melting point (MP), ($<10^{-8}$ torr at 29.8 °C) and low solubility in (the substrate) tungsten [79].

Production of a stable ion beam can be separated into three parts, i) heating of the source to the melting point of Ga, causing the material to flow towards and "wet" the substrate tip, ii) application of a high electric field (~ 10^8 V/cm) to the tip causing the liquid Ga to form a "Taylor cone", and iii) extraction of Ga atoms from the tip and ionization through field evaporation [81]. The recently evaporated ions at the tip are replaced by excess material from the reservoir. A stable beam consists of singly or doubly charged monomer ions, maintained at a current of ~2.0 μA, which is then accelerated at 1-30 kV toward the sample.

1.6.3 Ion-solid Interactions

When these accelerated ions impact the surface their interaction with the surface atoms can be classified as either elastic or inelastic collisions. The most common types of

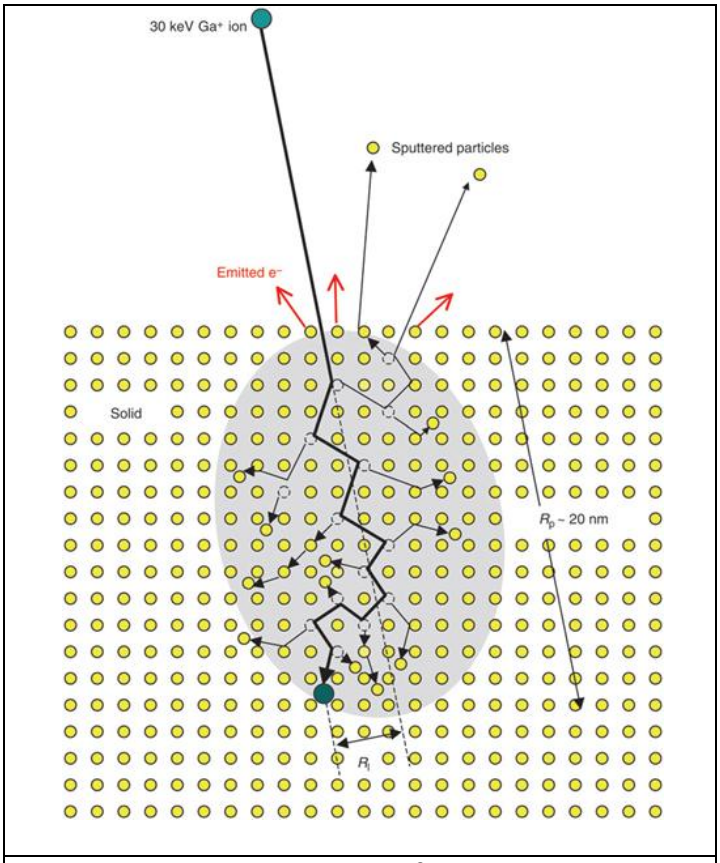

FIGURE 1.14: Illustration of the linear collision cascade occurring in a target material following impact of an incident Ga^+ ion. Also shown in this figure are some of the species produced following a collision. This includes secondary electrons/ions, sputtered atoms, and dislocations/vacancies at the target surface and inside the material. [80]

incident (ion)-target (solid) interactions are illustrated in FIGURE 1.14 [80], where inelastic collisions are represented by the production of secondary electrons (SE), x-rays, or optical photons, and the elastic collisions create sputtered target atoms or defects such as vacancies and dislocations. The SE created during collisions can be collected to produce an image of the sample surface and sputtering of the surface atoms allows for nanometer resolution milling. However, even if the user's intention is only to image the surface, the incident ions will still sputter the surface atoms or at least cause some damage. This damage is often described as a linear collision cascade, where the kinetic

energy of the incident ion is transferred to the target atom at the surface. If the transferred energy is high enough to overcome the binding energy of atoms in the target then these atoms will be ejected from the solid. There are multiple theories that attempt to describe the sputtering yield, number of sputtered target atoms per incident ion, but all of these theories are based on the ratio between the atomic mass (M) and number (Z) of the incident (M_1, Z_1) and target (M_2, Z_2) atoms [79]. The incident Ga^+ ion will continue penetrating into the solid, stopping at a value R_p, the project range, creating a damage layer in the target material. This implantation depth can be calculated using stopping/transmission range of ions in matter (SRIM/TRIM), and though it varies between materials, the average depth is ~30 nm [82]. While shallow, this implantation is a concern because of possible embrittlement or amorphization of the target material, which can affect the mechanical properties [83, 84]. Two separate reports by Bei and Shim investigated the effect of the incident angle and acceleration voltage of a Ga^+ ion beam on the hardness of a Mo-alloy [85, 86]. The results show that the highest hardness values were measured when the ion beam milling occurred at normal incidence and higher accelerating voltages. It should be noted that nanoindentation was used to measure the hardness and the maximum depth only reach 120 nm. Since the implantation depth is ~30 nm it is possible that the hardness values would converge if the indentation depth is greater. The ion beam can also be used for deposition of metals such like Pt, C, or W through the decomposition of a metal-organic precursor gas at the target surface [81]. However, the ion beam always causes damage at the target surface, therefore proper beam parameters like accelerating voltage and beam current must be used for imaging or metal deposition.

1.7 Micromechanical Testing

Small scale, site-specific mechanical testing is used to take advantage of the inherent grain size gradient present in HPT processed metals. These techniques include nanoindentation, microcompression, and *in-situ* SEM microtension. Using these techniques it is possible to probe the bulk material properties of NC metals while only testing a small volume of material. While there has been a large amount of work on nanoindentation and microcompression testing, reports on microtension testing are not as numerous.

1.7.1 Nanoindentation

Nanoindentation is a method of hardness measurement where the user sets a maximum load or displacement value and the instrument records both the load and displacement of a indenter tip simultaneously [87]. The applied loads are on the order of 10^{-6} – 10^{-3} N range, while the displacements can vary from tens to thousands of nanometers depending on the system. This technique was originally developed by Warren Oliver and George Pharr to probe the mechanical properties of materials at the submicron scale, while overcoming the difficulty of measuring the area of the small residual indent [88, 89]. A typical nanoindentation system is comprised of a transducer (coil/magnet assembly) to apply the load and a capacitance gauge to measure the tip displacement. Attached to this assembly is the tip used to indent the surface, and the most commonly used tip is a three sided pyramidal tip known as a Berkovich tip. But spherical, conical, Knoop (primarily for measuring hardness of hard materials such as ceramics and for evaluating the fracture toughness of such materials) and other tips have also been used.

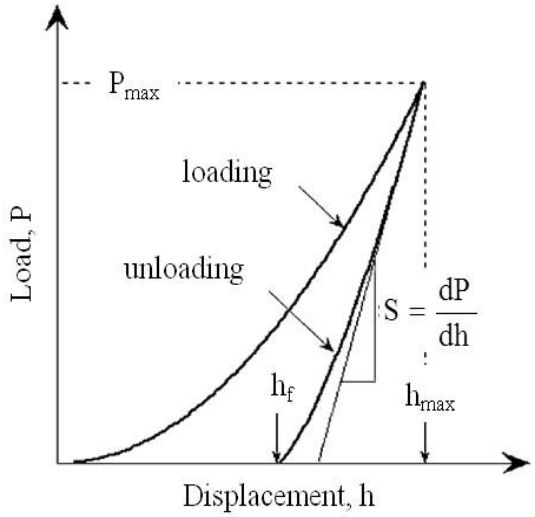

FIGURE 1.15: Schematic of a typical load-displacement curve for nanoindentation indicating where the values for maximum load, maximum depth, and stiffness are obtained. [89]

A typical load vs. displacement curve for nanoindentation testing is shown in FIGURE 1.15 [89]. The important points on this curve are the maximum load (P_{max}), maximum displacement (h_{max}), and the slope of the unloading portion which is the stiffness (S). Using these values the hardness (H) and elastic modulus (E) of the tested material can be determined using equation 1.10, equation 1.11, and equation 1.12, provided that a few tip parameters are also known. These parameters include the tip's elastic modulus (E_i), Poisson's ratio (ν_i), and most importantly the area function ($A(h)$). The contact area of the tip is a function of the tip displacement into the surface and must be calibrated in order to correctly calculate H and E.

$$H = \frac{P_{max}}{A} \qquad \text{equation 1.10}$$

$$S = \beta \frac{2}{\sqrt{\pi}} E_{eff} \sqrt{A} \qquad \text{equation 1.11}$$

$$\frac{1}{E_{eff}} = \frac{1-\nu^2}{E} + \frac{1-\nu_i^2}{E_i} \qquad \text{equation 1.12}$$

The small size scales achievable through nanoindentation have made the technique unique in characterizing the mechanical properties of materials of small volumes such as thin films. There are many reports of its use in testing the mechanical properties of metals [90], thin films [91], polymers [92], metallic glasses [93], even bone and tooth enamel [94, 95]. During film testing it has been shown that the substrate the films are attached to affects the final measured mechanical properties [91, 96, 97]. Also, care must be taken when setting the maximum depth of the indent for softer metals. Nix and Gao developed a model for single crystal specimens, based on the existence of geometrically necessary dislocations during indentation, that shallower indents will produce higher hardness values through Equation 1.13 [98].

$$H/H_o = \sqrt{1+h^*/h} \qquad \text{equation 1.13}$$

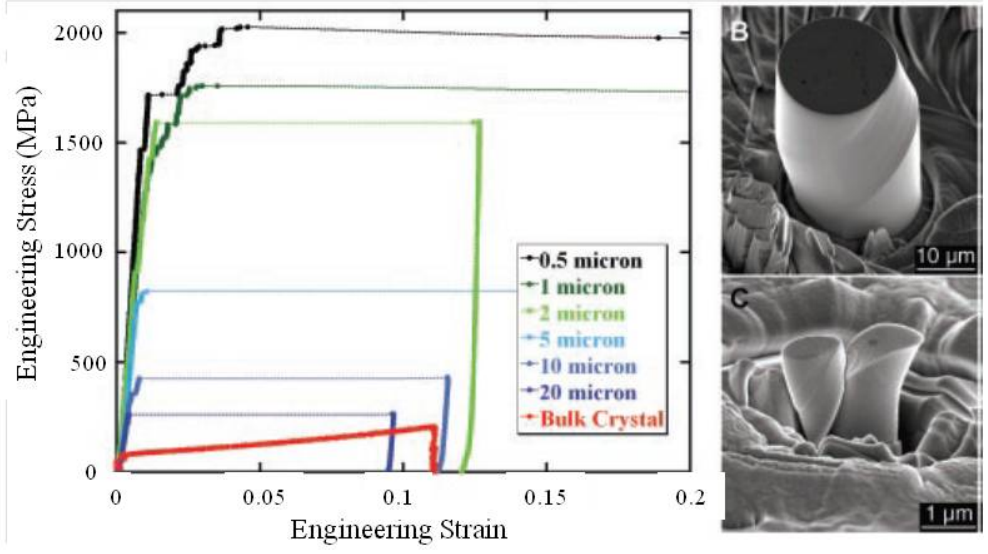

FIGURE 1.16: Microcompression studies on single crystal Ni showing the increase in strength with decreasing sample size and resulting deformation behavior in these pillars. The smaller is stronger effect has become a topic of many research reports since this first report. [99]

In equation 1.13, H is the hardness at an indentation depth, h, and at infinite depth the hardness is H_o and h^* is a characteristic length that depends on the shape of the indenter, the shear modulus and H.

1.7.2 Microcompression

While nanoindentation is convenient and effective at determining the hardness and modulus of small volumes, its downside is the complicated stress field that exists in the material just below the tip. This makes it difficult to determine properties such as strength or determine dislocation dynamics of single crystals that are not affected by the tip shape. The latter has become important due to the increased use of microelectro-mechanical systems (MEMS) in applications where the parts are under stress. Uchic et al. developed a method to determine such material properties through the use of micron scale compression tests [99, 100]. As shown in FIGURE 1.16, pillars from a single crystal Ni_3Al-Ta super alloy with diameters ranging from 0.5 – 40 μm were fabricated using a FIB and then compressed with a nanoindenter, which has a flat punch tip instead of the Berkovich style sharp tip. Their work shows the activation of dominant slip systems corresponding to the crystal structure, but also as the diameter of the pillar decreases there is an increase in the strength.

Such length scale effects have been observed in earlier work on the tensile testing of whiskers by Brenner [101, 102]. In this work the smallest diameter whiskers had the highest strengths, a trend attributed to the number of dislocations present following growth of the single crystal whiskers. Since the first report on the microcompression there have been many reports that used this technique for a variety of materials, although most of the work is focused on the size-effect behavior of single crystal FCC metals (Au[103], Ni [104], Cu , and Al) while only a few on BCC (Mo [105], Ta [106], Nb[107]

) and HCP (Mg , Ti) metals. Greer et al. used microcompression to probe the size scale effects of gold pillars fabricated via FIB milling and micro-fabrication techniques [103]. Their reason for the second fabrication method is the concern of hardening due to Ga^{+} ion implantation in the FIB milled pillars. However, pillars fabricated by both methods showed the strength dependence on diameter which was attributed to dislocation starvation. Bei et al. also looked into the behavior of micropillars but used selective etching to create Mo pillars from a NiAl-Mo composite that do not have any FIB damage [108]. These pillars showed no size effect, instead yielding at near the theoretical strength of Mo, similar to the whisker studies.

While there continues to be studies on microcompression of single crystals in an effort to explain the “smaller is stronger” effect, the technique has seen an increase in use on a variety of materials, including nanocrystalline Ni [109], bulk metallic glass (BMG) [110, 111], shape memory alloys [112], and Cu-Nb multilayered film [113]. The work on BMGs is also focused on the effect of size on the strength but also the deformation mechanism. There is currently a disagreement in the literature over whether such an effect exists in BMGs, and some reports show a constant strength and formation of shear bands at all pillar sizes [110].

Others have reported that the strength does increase, but then plateaus when the pillar diameter is less than ~800 nm, and that there is a transition to homogeneous deformation in the smallest pillars (100 nm) [111]. However, there is a concern with the pillar geometry in the latter reports, specifically the tapered side walls and rounded tops of the pillars affecting the plastic behavior [114]. Zhang et al. showed that in order to perform accurate microcompression experiments, pillars must not have tapered side

walls and ideally should have an aspect ratio of 2 – 3 [115], both obtainable when using the fabrication method developed by Uchic et al [100].

It should be noted that microcompression can be used for more than just investigating the effect of pillar diameter. For example, a pillar made from an NC metal with a diameter greater than 1.0 μm means an individual grain will make up a small portion of the total volume [70]. Since there will be a large number of grains in the pillar the behavior can be considered the bulk response, meaning the test now acts as a scaled down compression test.

1.7.3 Microtension

Of course compression is only one technique used to determine the mechanical properties of materials. To accurately determine yield strength and ductility of a metal, the better testing technique is tension. There is a history of tension testing on millimeter scale and thin film specimens with thicknesses on the order of hundreds of microns [117-119]. Some important aspects of testing specimens at this scale are the specimen preparation, force application/measurement, and displacement/strain measurement [116]. While there are commercially available components for force application and displacement, using this technique to accurately determine properties, such as elastic

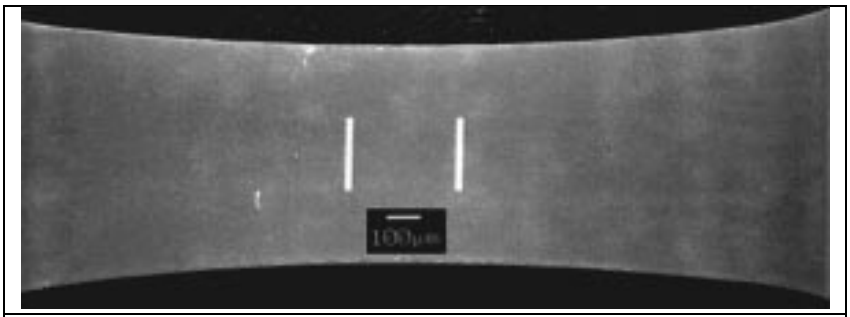

FIGURE 1.17: Imaging showing two gold lines in the gauge section of a millimeter scale tensile specimen.[116] These lines are used a markers as a means for measuring the strain applied during tensile testing.

modulus and yield strength, requires a novel method of the strain measurement. A more effective method is to use a noncontact optical technique developed by Sharpe et al. as a method that tracks the movement of two gold lines located in the gauge section of the sample, FIGURE 1.17 [116]. Tracking these gold lines is done by taking sequential images of the gauge section during testing and using image correlation software to locate and track the lines in each image.

There have been some recent efforts to extend the tensile testing into the micron scale, but not as many as microcompression. Kiener et al. were among the first to report on the size effects of copper single crystals using in-situ SEM tensile testing, shown in FIGURE 1.18a [120]. Their work showed that at high aspect ratios (>5:1) there was no strong size effect but at low aspect ratios (1:1) there was a strong size effect. Kim and Greer used the FIB to machine tensile samples of Au, W, Nb, Mo, and Ta, FIGURE 1.18b [121, 122]. They found that all the materials tested displayed the “smaller-is-stronger” behavior similar to results from microcompression tests. This behavior was more pronounced in Ta and Nb than for W and Mo, since the deformation mechanism was found to be activation of kink pairs this behavior was attributed to differences in the Peierls stress between materials. While the previous reports were able to observe the mechanical behavior of small scale singe crystals in tension, they both calculated the strain on the sample using the cross-head displacement of their set-up. This is an effective means of calculating strain if the entire system compliance can be accounted for, an item that is not discussed in either report. In-situ SEM tensile tests performed on single crystal Ni and a Ni-based super alloy instead monitored the displacement of fiducial markers in the gauge section of the specimen, FIGURE 1.18c [124]. This technique is similar to macroscopic tensile tests that use extensometers, and knowing how these markers move relative to each other

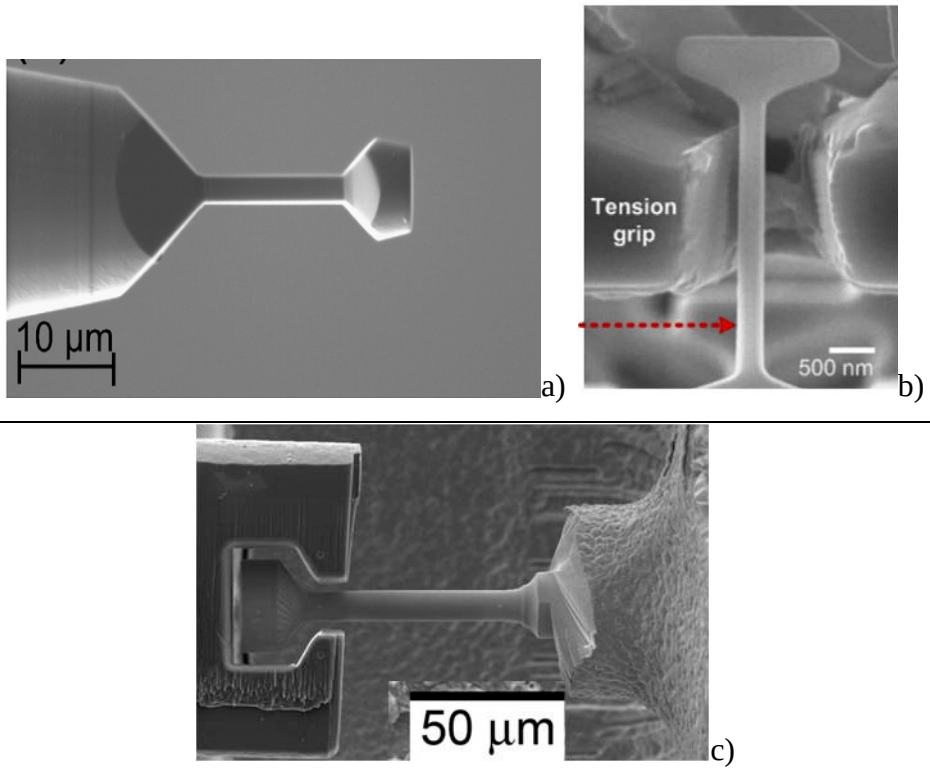

FIGURE 1.18: SEM images of microtension specimens fabricated using the FIB. Similar to microcompression, (a) single crystal specimens were made from Cu [123], (b) Au, W, Nb, Mo, and Ta, [121, 122] to investigate the size effects. (c) A microtensile specimen made from single crystal Ni that uses fiducial markers to measure and to calculate the strain. [124]

during testing allows for a better measure of the strain in the specimen.

1.8 Tantalum

1.8.1 Introduction

The work for this dissertation focuses on tantalum, a body-centered cubic transition metal, also classified as a refractory metal. Historically, the discovery and identification of tantalum began with Charles Hatchett who, in 1802, published his work of chemical analysis on an unknown metal discovered in a mine in Massachusetts [125]. Following many attempts to dissolve and precipitate out the constituent elements he determined that a portion of this metal was insoluble in many acids and had a specific gravity that could not be attributed to any known metals. He called this new element

Columbium after the location where the metal was discovered. Shortly after this discovery a Swedish scientist, Anders Ekeberg, reported on a metal unknown to him that displays similar properties to those reported for Columbium. Due to this metal's insolubility in many acids, and not being aware of the work by Hatchett, he called the metal tantalum after the character Tantalus in Greek mythology, which is also the origin of the English word "tantalize". Columbium and tantalum were thought to be two different metals, due to their different specific gravities, 5.918 for columbium and 7.953 for tantalum, but in 1809 William Hyde Wollaston analyzed both metals and determined them to actually be the same [126]. They were considered the same until the discovery of niobium in the mid 1800s, which was able to account for the difference in specific gravity since the chemical composition of the original columbium metal was both niobium and tantalum. Since the metal studied by Ekeberg was only tantalum the name and discovery of the metal is attributed to him.

There are two main tantalum phases, alpha and beta. Most naturally occurring Ta is alpha phase, which has a BCC crystal structure, while deposition of Ta via magnetron sputtering contains the tetragonal beta phase [127]. As will be shown later, the work in this dissertation only involves alpha-Ta, therefore from this point on, tantalum will refer to the alpha phase; if the other phase is discussed it will be indicated as such. TABLE 1.1 is a summary of some physical and mechanical properties of Ta. Tantalum has an atomic number of 73, making it a group VI element along with vanadium and niobium. Its density is one of the highest at 16.6 g/cm^3; only roughly a dozen elements (i.e. Au, W, Re, Os, Ir, U, etc.) have higher values of density while its melting point, at ~3000°C, is the fifth highest [128]. Mechanically, the elastic modulus is 186 GPa, Poisson's ratio is

0.35, and the strength, while varying depending on processing, is on the order of hundreds of MPa.

1.8.2 UFG/NC Behavior of Tantalum

There are reports of nanoindentation tests on thin films of NC Ta fabricated by magnetron sputtering that show deformation twinning and high hardness when a tetragonal β-Ta phase is introduced [127, 129]. Mathaudhu and Hartwig processed commercially pure Ta through various ECAP routes to obtain a homogenous, equiaxed microstructure and performed tension tests on the resulting samples [130, 131]. Their work showed that while the ECAP process was able to produce the desired microstructure, certain processing routes left textured bands which resulted in localized deformation. Wei et al. also performed quasi-static and dynamic tests on ECAP Ta and showed that ASBs were formed under high strain rates [66]. There is also a greatly improved strength over CG Ta and a decrease in the SRS to m = 0.025 (compared to ~0.04 of coarse-grained tantalum). Both of these changes are in order with expected results for UFG BCC metals. The grain sizes for these ECAP Ta tests were still in the UFG regime, though. Wei et al. continued to refine the grain size of tantalum into the NC

TABLE 1.1: Typical mechanical properties associated with single crystal and coarse grain Ta. [128] Important properties of note for this work are the crystal structure, lattice constant, yield strength, and Young's modulus.

Atomic Number	73
Crystal Sturcture	BCC
Density (g/cm^3)	16.6
Lattice Constant (Å)	3.16
Melting Point (°C)	2996
Yield Strength: Annealed (MPa)	170
Yield Strength: Cold Work (MPa)	655
Young's Modulus (GPa)	186
Poisson's Ratio	0.35

regime by investigating the dynamic behavior of HPT Ta samples taken at different radial positions [65]. Samples of NC Ta taken near the disk center deformed via diffuse bands under high strain rate compression and showed more severe ASBs as the tested samples move closer to the disk edge, indicating that the microstructure has an influence on the deformation mode. Pan et al. used molecular dynamics simulation to study the tensile behavior of NC Ta with grain sizes from 3.0 – 13 nm [132]. These simulations showed a markedly reduced elastic modulus (135 GPa), along with evidence of the inverse Hall-Petch effect, and deformation mechanisms that depend on grain size. At a grain size of 6.5 nm they observed grain rotation and sliding while at 13 nm there was only dislocation motion.

1.9 Summary and Motivation

Grain size refinement of metals into the UFG/NC regimes is possible through both bottom-up (mechanical attrition, inert gas condensation, electrodeposition, and so on) or top-down (ECAP, ARB, HPT, etc.) techniques [13, 17, 133]. At these grain sizes, metals show greatly increased strength due to the Hall-Petch effect, along with a reduction in strain hardening capacity and therefore decreased ductility [6]. The reduced strain hardening is due to the fact that it becomes increasingly more difficult for the dislocations to accumulate in the grain interior, and instead dislocations are emitted from and are absorbed at grain boundaries [55]. Changes in strain rate sensitivity are also observed in these regimes, where for FCC metals the SRS increases with decreasing grain size while in BCC metals the opposite is true [11]. The deformation behavior also transitions from being dominated by dislocation motion to grain boundary motion processes. These processes include grain boundary sliding [59], rotation [56, 134], or coupled grain boundary motion [57]. When grain boundary motion begins to dominate,

which occurs around grain size ~10 – 20 nm, the strength of NC metals begins to decrease to yield an inverse Hall-Petch effect [135, 136].

Most of the work done to determine the mechanical properties of NC metals is on FCC metals like Cu, Al, or Ni. The few reports on UFG/NC BCC metals have focused on their behavior under dynamic compression. At high strain rates (~10^3 /s) these metals show an increased propensity to deform via adiabatic shear bands [63, 66, 68, 137, 138]. This behavior has been observed for UFG/NC Fe, W, Ta, and V processed by both bottom-up and top-down methods. Materials that form ASBs under dynamic compression show improved performance in KE penetrators over homogenously plastically deformed metals [71]. Therefore, NC BCC metals are a possible material replacement for DU, but their quasi-static behavior must be quantified. KE penetrator materials must display at least small amounts of ductility and no shear band formation at lower strain rates to survive initial launch conditions [70]. Unfortunately, there is not a lot of work that reports on the quasi-static behavior of truly NC BCC metals.

The goal of this dissertation is to quantify the effects of grain size on the quasi-static mechanical properties of NC Ta. A bulk Ta sample will undergo grain size refinement via HPT processing to produce a disk sample that contains a grain size gradient [31]. Site specific mechanical properties are determined by micromechanical testing techniques, such as nanoindentation and microcompression/tension, and related back to the underlying microstructures. Nanoindentation studies will provide hardness and modulus profiles of the disk by following the Oliver-Pharr technique [88, 89]. Microcompression/tension is used as a scaled down “bulk” testing technique instead of investigating a strength dependence on pillar size like the majority of literature reports [139, 140]. The main goal for this work is to identify a microstructure (i.e. grain size,

shape, etc.) that displays homogeneous deformation and some tensile ductility while at quasi-static rates, but displays ASBs at dynamic rates. UFG/NC Ta is chosen for this work because it has a high density, shows ASB behavior at high rates and, in the case of coarse grain sizes, displays higher ductility than other BCC metals [141]. One more justification for this choice is the high melting point of Ta, which allows reduction of grain size into the truly NC regime as the T_{Rx} is higher.

CHAPTER 2: EXPERIMENTAL METHODS

2.1 High Pressure Torsion

HPT processing was carried out at room temperature on a tantalum disk ~12 mm in diameter and 1.2 mm thick under a confining pressure of 5.0 GPa for a total of five turns (N =5). A schematic of the processed disk is shown in FIGURE 2.1a, where X is the disk radius, h is the thickness, and $d\theta$ is the angle of rotation. If $d\theta$ is small, then the length $dl = Xd\theta$, and the induced strain can be defined as, $d\gamma = dl/dh = Xd\theta/dh$. For $d\theta = 2\pi \cdot N$, where N is the number of rotations of the platen, the values for the strain can be calculated using equation 2.1, or the von Mises equivalent strain in equation 2.2 [31].

$$\gamma = \frac{2\pi N \cdot X}{h} \qquad \text{equation 2. 1}$$

$$\varepsilon_{VM} = \frac{2\pi N \cdot X}{\sqrt{3} \cdot h} \qquad \text{equation 2. 2}$$

FIGURE 2.1b shows how the induced strain in the disk changes with radius for N = 5, following equation 2.2.This plot shows that for the disk dimensions, at X = 1.0 mm an equivalent strain of ~15 is attained after completing the rotations, while at X = 5 mm the strains reach ~90. It is easily seen that positions further from the center will have a higher induced strain than positions closer to the center. Since a higher strain causes more grain refinement it is possible to have a grain size gradient across the disk radius. This gradient is seen in the channeling contrast images of an HPT W disk processed under

similar conditions, FIGURE 2.2. The large grains at the center, FIGURE 2.2a, break down into smaller grains closer to the edge, FIGURE 2.2b and 2c.

Using a diamond saw, the HPT processed Ta disk was sectioned into one half, FIGURE 2.3a, and one quarter piece, FIGURE 2.3b, for specimen preparations for microtension, microcompression and nanoindentation, respectively. The quarter disk and a 1.0 x 1.0 mm piece of Al with a similar thickness were mounted on a 1.0 inch tall, 0.75" diameter Al puck using super glue. The Al and Ta were mechanically polished together to ensure they were at the same height on the puck. Polishing was done using diamond lapping films starting at a surface finish of 30 μm and stopping at a finish of < 1.0 μm. The half disk of Ta was also mechanically polished using diamond lapping films down to a surface finish of 1.0 μm and sent out in order to have tension pre-forms milled into the surface via micro-electro discharge machining (μ-EDM), which will be described later.

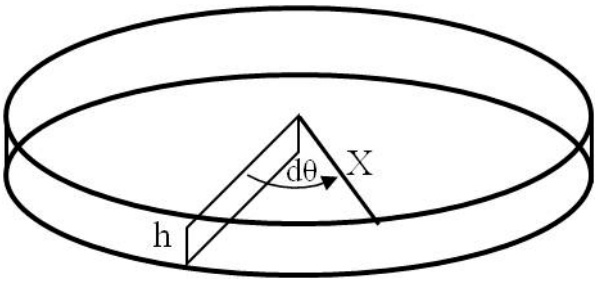

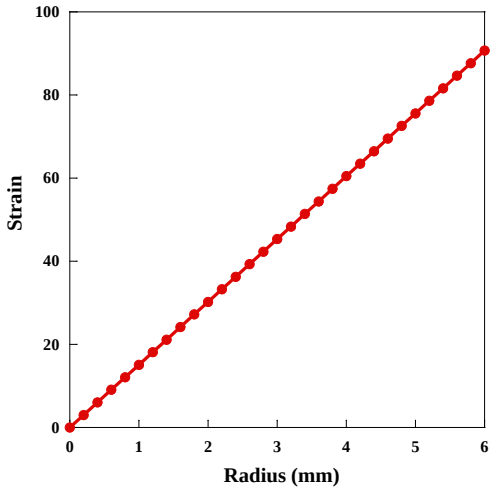

a) b)

FIGURE 2.1: (a) Schematic of the HPT processed disk with the parameters needed to calculate the induced strain, most importantly the dependence on the radius X. (b) Plot of the induced strain vs. radius using equation 2.2, where the increased strain suggests a grain size gradient.

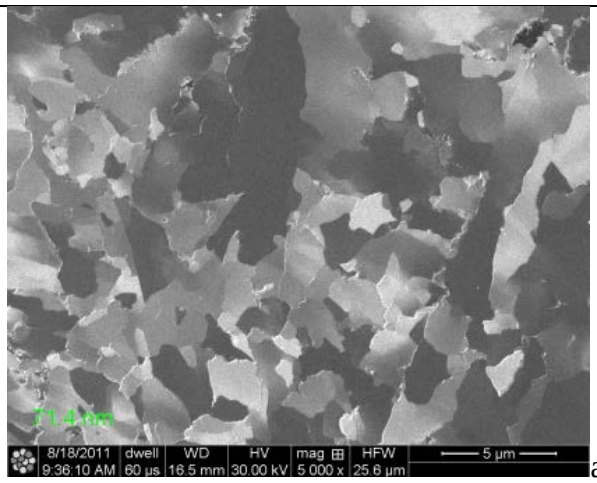

a)

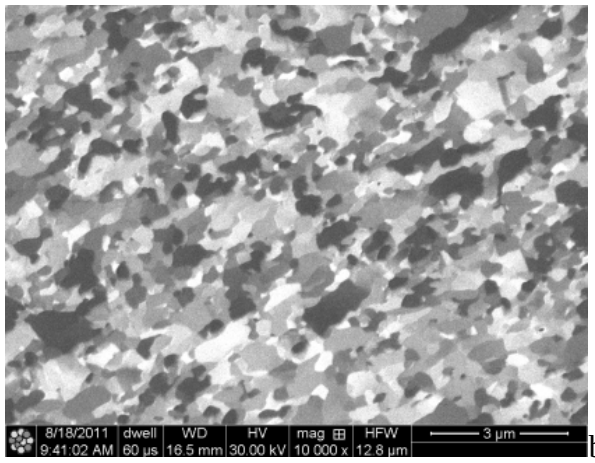

b)

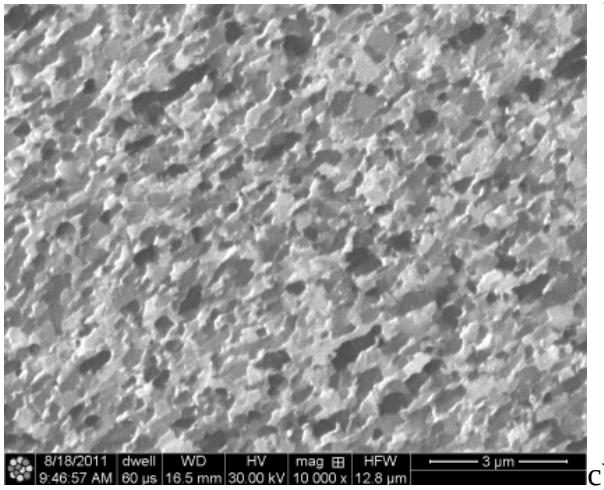

c)

FIGURE 2.2: FIB ion channeling images of W processed by HPT under similar conditions as the Ta. (a) Near the disk center showing large, coarse grain sizes. (b) At a medium radial position containing smaller UFG sizes. (c) Near the disk edge, showing even smaller NC grains. If mechanical tests can be performed at these individual locations then the grain size effect can be determined.

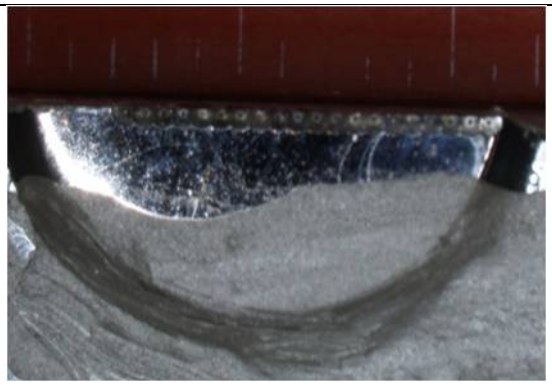

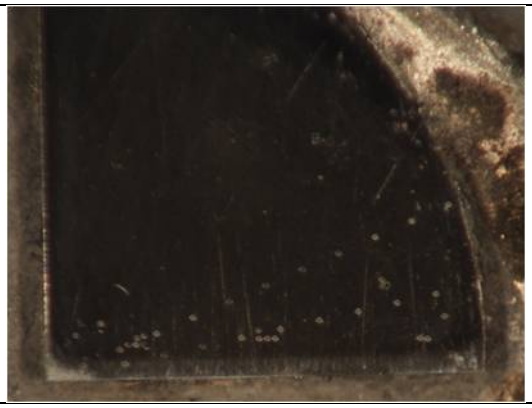

a) b)

FIGURE 2.3: Optical micrographs of the (a) half disk sample used for fabricating tensile specimens, and (b) the quarter disk sample used for nanoindentation and microcompression.

2.2 Microstructure Analysis

In this work, the two main microstructure features of interest are the deformation texture and grain structure (size, shape, grain boundary types) because these can greatly affect the mechanical properties. The techniques used to investigate these two features are synchrotron x-ray diffraction (SXRD) and transmission electron microscopy (TEM).

2.2.1 Transmission Electron Microscopy

The TEM analysis was done using a JEOL JEM-2100F with an accelerating voltage of 200 kV at multiple positions, X = 3.0, 5.3, and 5.9 mm, along the disk radius. All TEM lamellas were prepared using an FEI Nova NanoLab i600 Focused Ion Beam (FIB), and the final thinning was done at 5 kV. In order to account for possible changes in the grain shape due to HPT processing, at each location lamellas were prepared at orientations parallel, perpendicular, and normal to the torsion straining. This will give a 3-D representation of the grains produced by HPT. Grain size measurements were made from the TEM micrographs by first tracing well defined grain boundaries. Using these traces, ImagePro© software models each grain as an equivalent ellipse, shown in

FIGURE 2.4, and measure the maximum diameter (d_{max}), minimum diameter (d_{min}), and area (A_{grain}) of each grain [60]. From these measurements, the area fraction (A_{frac}), area weighted average diameter (d_{awa}), and cumulative area fraction distribution were calculated using equation 2.3, equation 2.4, and equation 2.5 respectively. The total number of measured grains for each location is: 250 at X = 5.9 mm, 230 at X= 5.3 mm, and 60 at X = 3.0 mm.

$$A_{frac} = \frac{A_{grain}}{A_{tot}} \qquad \text{equation 2. 3}$$

$$d_{awa} = \frac{\sum \left(d_{max} \cdot A_{grain} \right)}{A_{tot}} \qquad \text{equation 2. 4}$$

$$A_{cum} = \frac{\sum A_{frac}}{A_{tot}} \qquad \text{equation 2. 5}$$

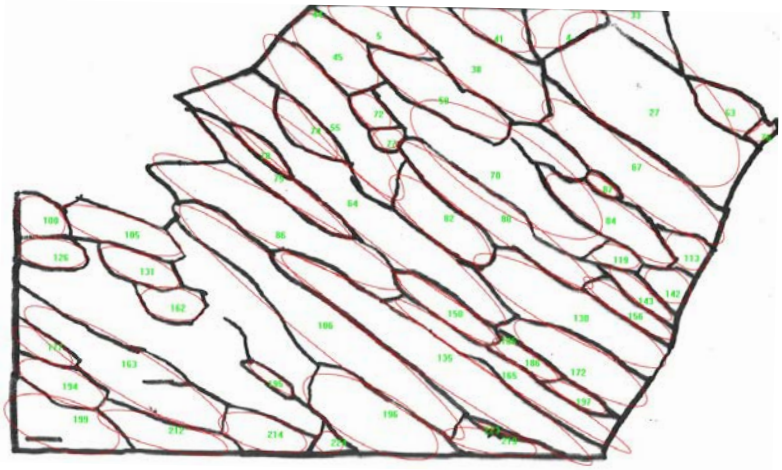

FIGURE 2.4: Image of the grain tracings used to determine the grain size from TEM images. Black lines represent the traced grain boundaries which determine specific grains, which are then estimated as an equivalent ellipse in red. From these ellipses the values for maximum/minimum diameter and grain area are measured.

2.2.2 Synchrotron X-Ray Diffraction

The resulting deformation texture following HPT was quantified using SXRD at the Advanced Photon Source in Argonne National Laboratory, beamline 11-ID-C, shown in FIGURE 2.5a [142, 143]. This beamline provides a 115 keV beam, with wavelength λ~0.01079 nm, and a spot size of 150x150 μm and 2-D detector, making it possible to perform site-specific texture analysis in transmission mode at multiple locations. FIGURE 2.5b and c show the stage and the sample orientation of this system, respectively. The incident beam is parallel to the χ-axis of the stage, FIGURE 2.5b. Since the deformation mode during HPT can be considered to be simple shear, texture measurements should be made on the shear plane, i.e., the *z*-*x* or *z*-*y* planes in FIGURE 2.5c. However the interest is how the texture changes with radial position so the sample is rotated 90° about the stage φ-axis, making the sample's *z*-axis parallel to the beam and the *x*-*y* plane is then the measurement surface. Measurements were done at multiple positions along both the *x*- and *y*-axis and while tilting the sample about the ω-axis from 0 – 45° in 5° steps. Debye-Scherrer patterns were recorded at each position and tilt angle using a 6 second exposure time.

With the Materials Analysis Using Diffraction (MAUD) software, grain size estimates and reconstructed pole figures were calculated [144, 145]. To determine instrumental broadening and peak shape functions, the previously described SXRD analysis was first done on a CeO_2 standard sample. The grain size values in MAUD are still calculated from the peak broadening using the Scherrer equation, $D = (K\lambda)/(\beta \cos\theta)$ [146], here D is the crystallite domain size (or the coherent domain size), β is the full width at half max (FWHM) in radians, λ is the wavelength, K is a constant, and θ is the diffraction angle

(Bragg angle). However, instead of a FWHM value, MAUD calculates an integral breadth for β after subtracting out instrumental broadening effects [147].

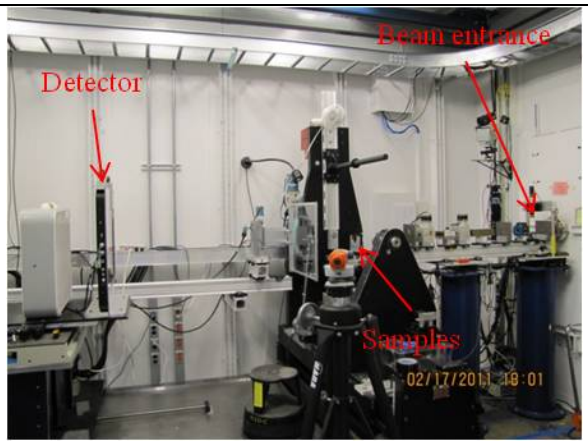

a)

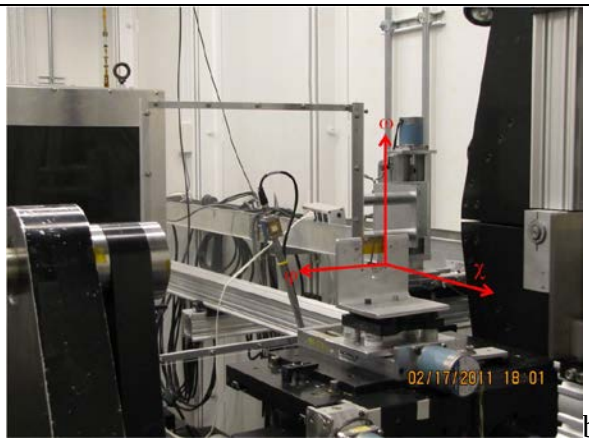

b)

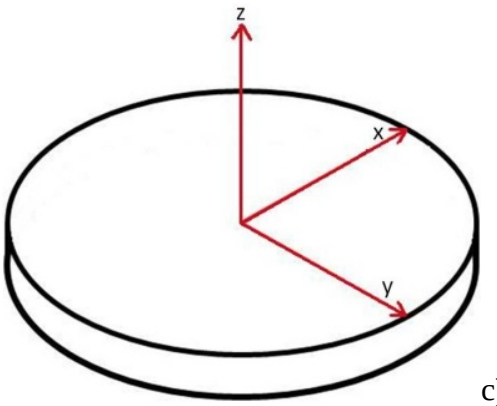

c)

FIGURE 2.5: (a) Image of the bay at beamline 11-ID-C at APS, the 2-D detector is at the left hand side, meaning the beam propagation direction is from right-to-left. (b) Image of the stage and sample holder with the stage ω-χ-ϕ-axis indicated in red, rotation is about the ω-axis. (c) Schematic of the Ta disk to be measured with the sample x-y-z-axis, where the beam is incident along the z-axis and measurements are taken along x-y plane.

2.3 Nanoindentation

In a typical nanoindentation test, the user has control over the maximum load (P_{max}) or displacement (h_{max}) and the time to load. If the system is operated in the constant stiffness mode (CSM) then the user can also define a target strain rate during the test. This is possible due to CSM's addition of a small ~2.0 nm, 45 Hz oscillation to the indenter tip during loading, allowing for a measurement of the displacement rate of the tip ($\dot{h}$), which can give a measure of the strain rate ($\dot{\varepsilon}$) at each point by equation 2.6 [148]. The ability to indent at a prescribed strain rate is advantageous when attempting to get strain rate sensitivity measurements via indentation.

$$\dot{\varepsilon} = \dot{h}/h \qquad \text{equation 2. 6}$$

Nanoindentation hardness, elastic modulus, and strain rate sensitivity of HPT Ta are obtained with respect to position on the disk. Tests were performed at multiple locations on the disk starting near the center and moving toward the edge. The location of a test is indicated by its distance, X, from the original disk center, for example X = 3.0 mm means that the test was performed 3.0 mm away from the center. All the tests were performed using an MTS XP Nanoindenter system with a Berkovich tip with the XP CSM Standard Hardness, Modulus, Tip Cal method. It allows the user to define the maximum depth of the indent as well as the target strain rate during loading.

2.3.1 Hardness and Modulus

A tip area function calibration was performed on the Berkovich tip by running a set of 25 indents, maximum depth of 2000 nm at a rate of 0.05 s^{-1}, on a fused silica standard. To obtain the stiffness values the system is operated in CSM mode during these

tests. With the known stiffness, material modulus (72 GPa), and Poisson's ratio (0.35) values, the area vs. displacement can be plotted using equation 1.11 and fitted to a polynomial of the form in equation 2.7 [89].

$$A = \sum_{n=0}^{8} C_n \left(h_c\right)^{2-n} \qquad \text{equation 2.7}$$

This calibration gave values within 1.0 GPa of the accepted elastic modulus and hardness for fused silica. Indents to measure the hardness and modulus were done on the Ta sample moving from the center (X ~ 1.0 mm) to the edge (X ~ 6.0 mm) in 0.5 mm intervals performing ten indents at each location. Indents were performed at a target strain rate of 0.05 s^{-1} up to a maximum depth of 2000 nm. The Oliver-Pharr method was used to calculate the hardness and elastic modulus from the unloading curve [88, 89].

2.3.2 Strain Rate Sensitivity

Measurements for the strain rate sensitivity (SRS) were performed at locations X ~ 1.0, 3.0 and 6.0 mm. At each location, a set of 20 indents was conducted at target strain rates of 0.01, 0.05, and 0.1 s^{-1}. Oliver-Pharr Hardness measurements were taken for each set. Plotting ln (H) vs. ln $(\dot{\varepsilon})$at each location gives the SRS by using equation 2.8, where H is the hardness, $\dot{\varepsilon}$ the target strain rate, and m the SRS. The slope of the line for this plot is m [11]. Once the SRS is calculated it was used to calculate the activation volume, v^*, at each location using equation 2.9, where k_B is the Boltzmann constant and T = 300 K is the temperature [11]. When reporting the activation volume the common b^3 convention is used. For this reporting method, b is the Burgers vector for Ta which can be calculated from, $b = a/2\langle 111 \rangle$ where the lattice parameter (a) is given in Table 1.1.

$$m = \frac{\partial \ln H}{\partial \ln \dot{\varepsilon}} \qquad \text{equation 2.8}$$

. $$v^* = \frac{3\sqrt{3} \cdot k_B T}{H \cdot m} \qquad \text{equation 2. 9}$$

2.4 Microcompression

Following the HPT processing the Ta disk is only 12 mm in diameter and 1-2 mm thick and the grain size varies with radial position. The small sample size and the grain size gradient are difficult to take into account for any conventional style compression test. Scaling down the compression specimen diameter to the order of micrometers and by using a nanoindenter the tests can overcome the issues mentioned above [99]. The small scale tests have the advantage of being able to perform tests at site-specific locations which ensures that each specimen contains a homogeneous grain size. If each specimen has a different grain size then the effects of the grain size on the mechanical properties can be established through the use of only one HPT processed disk.

2.4.1 Fabrication of pillars

Fabricating these small specimens was done using an FEI Nova Nanolab 600i Focused Ion beam (FIB) microscope. However, since milling using a FIB is not a fast process, making a single compression pillar could take an entire day. This is not efficient since the user must be present during the entire process. It is advantageous to create some form of automation to mill pillars at specific locations and with user determined diameter. As will be discussed later, researchers at the Air Force Research Laboratory (AFRL) have created a script dubbed “AutoMike” for thinning pillars, but this is only one part of the milling process and it only runs at one location at a time. Here, scripts have been written that allow for minimal user input during all parts of the milling process and perform these

actions at multiple locations. Called “AutoFrancis”, this script is more user friendly since it allows milling of pillars with diameters of 2.5, 5, 10, or 20 μm without changing any of the base code. Also, it can accommodate up to 20 separate milling locations for either the rough milling or “AutoMike” thinning in one run. An overview of the “AutoFrancis” program is given in Appendix B. Together these features make pillar fabrication more efficient due to utilization of time when the machine would normally not be able to run, such as overnights and weekends. Following the process described below, pillars were milling on the Ta disk starting at the disk center (X~1.0 mm) out to the edge (X~ 6.0 mm) at intervals of 0.5 mm. The final pillars had a diameter of 5 – 10 μm and an aspect ratio of 2.0, in keeping with the suggestion of Zhang et el. [115].

Fabricating compression specimens is a two-step process that begins by milling rough pillars into the material of interest. For this step, the ion beam is at 30 kV and 21 nA while the sample is tilted so that its surface is at normal incidence. A circle is milled

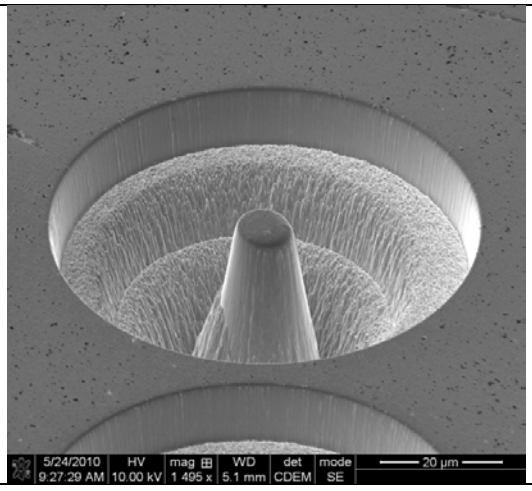

a)

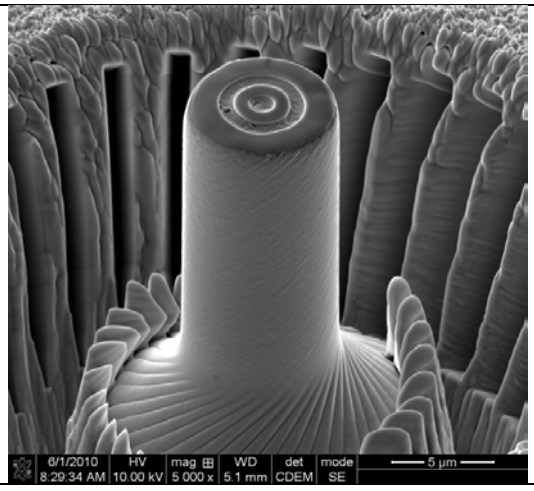

b)

FIGURE 2.6: SEM micrographs of an (a) rough milled and (b) thinned pillar. The well around the rough pillar must be large enough to accept the flat punch during compression and the vertical lines behind the thinned pillar are a result of the lathe process.

into the surface with the following dimensions, an outer diameter (OD) ~65 μm and inner diameter about two times that of the desired pillar diameter. The depth of this milling should be enough to allow the base of the final pillar to be visible with the SEM beam but not so much as to give this rough pillar a large aspect ratio. The SEM micrograph in FIGURE 2.6a shows a finished rough pillar. It is to be noted here that the pillar should not be tested in this form since ion milling at normal incidence leaves a 1 – 2° taper on the side walls. This taper would result in changes to the stress state inside the pillar if tested now. The taper must be removed and a pillar such as displayed in FIGURE 2.6b should be the final form of the pillar for testing.

Thinning the rough pillar is the second step and is done by using the "AutoMike" program mentioned earlier [100]. It is run first at a beam current of 0.92 nA to get a pillar with the desired height but with a slightly larger diameter and then at 93 pA to remove the damage layer from the previous thinning and get a pillar with the correct diameter. A more detailed explanation of the thinning process will be given later, but briefly, it works similar to a lathe technique. First it mills away a small portion of the sidewall to the desired pillar dimensions, followed by a sample rotation and repeated milling until the specimen is complete (see Figure 2.6b). In order for "AutoMike" to function, however, the pillar must have the proper fiducial mark for the image matching.

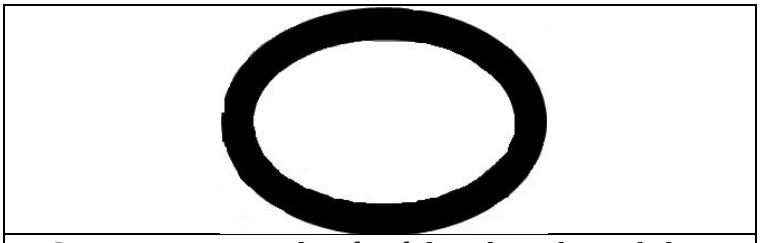

FIGURE 2.7: Example of a fiducial mark used during the image matching process of the pillar thinning script

To create the fiducial, the ion beam is used to deposit a ~250 nm thick Pt cap on the top of the rough pillar. If this cap is ~10 μm in diameter then this can be done at 30 kV and 0.28 nA. The reason for the Pt is that it helps improve the contrast of the fiducial during image recognition. Next, the circle fiducial is milled into this cap with the following dimensions: OD = ½ of the final pillar diameter, and ID = OD – 0.5 μm. So for example, a pillar that has a final diameter of 5.0 μm has a fiducial with an OD = 2.5 μm and ID = 2.0 μm, like the fiducial seen in FIGURE 2.7.

Before thinning the user must make sure that the FIB stage tilt is set to 0°, which is 52° with respect to the ion beam. The thinning process starts by capturing an image of the pillar with the ion beam and pattern recognition software locates the fiducial. Once located, the script calculates the distance between the screen and fiducial center, and the stage moves to make these two locations coincide. The image capture process continues until there is an error of ~ 1.0 μm between the locations. After positioning correctly, a cutting box is inserted at a location determined by the desired pillar diameter, which is set in the "AutoFrancis" script. It should be noted that the size of the cut box in the y-direction, which determines the pillar height, must have the sample tilt accounted for. Since the specimen is at 52° with respect to the ion beam the height of the cut box is given by $y_{box} = y_{pillar} \times \sin(52)$. Once the milling is finished the FIB stage performs a compucentric rotation of 10° and the program repeats itself starting with the image capture. In total, the stage rotates 42 times to allow for thinning of the entire circumference leaving a pillar like the one shown in FIGURE 2.6b. SEM is used to measure the pillar diameter and height.

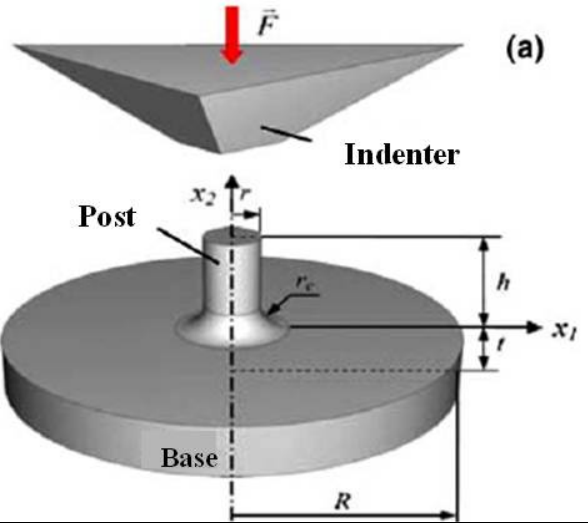

FIGURE 2.8: Schematic of the microcompression testing, where the flat punch indenter is used at the top platen and the pillar base is the bottom platen [115].

2.4.2 Testing

Compression tests were done using the same XP system as the nanoindentation tests but the Berkovich tip was replaced with a flat punch tip which is used as the top compression platen while the pillar base acts as the bottom platen. A schematic of the testing set-up is shown in FIGURE 2.8 [115]. A 20 μm diameter flat punch and a custom "XP CSM Post Compression" method was used for the testing. This method allows the user to define the specimen dimensions (nm), loading rate (mN/s) and maximum depth (nm). The system records the load (mN) vs. displacement (nm) of the tip during testing.

Since it is not possible to observe the tip-pillar contact before loading it is important to improve the alignment and accuracy of the tip placement before testing. This begins when the sample is loaded into the XP stage. Unlike newer XP systems, such as the Agilent G200, the stage on this system does not have any sample height adjustment once positioned in the stage. In fact, the standard operating procedure for this stage is to first turn it upside down to sit on calibrated foot pegs and drop the sample through a hole.

However, this procedure cannot be done with samples that have completed pillars due to the risk of damage to the specimens. Instead, the puck with the Ta and Al pieces was placed into a slot on the XP stage and the sample height is adjusted by eye to be close to the correct sample height, the sample surface should be even with or lower than the stage foot pegs or the tip could be damaged during stage movements.

Once mounted the “Microscope-to-Indenter” calibration step is done on the Al piece mounted next to the Ta disk. Since both samples were polished together they will be at the same height, thus improving the chances of contacting the top of the pillar. At the end of this calibration the user is asked to position the cross-hair at the center-most indent. To move the cross-hair to this position but before ending the calibration, we select the “Remove Backlash” option, found by a “right” mouse click. If the center indent does not return to the cross-hair, we need to redo the positioning and backlash removal until the cross-hair stays on the center indent. This might not need to be done on newer XP systems, such as a G200, since it has a piezo-stage instead of the screw driven stage on the older model. This process improves the accuracy of the tip location during testing, reducing the chance of only the edge of the tip hitting the pillar, which could cause the pillar to buckle during plastic deformation. After alignment, locate the pillar to be tested and repeat the “Remove Backlash” procedure until the cross-hair remains on the pillar’s center. This can take a few minutes but is helpful for improving the indent accuracy.

Once a location is determined, the user defines the batch parameters for compression. Most of the batch parameters may be left at their default values but there are a few that need to be decided by the user. The first is the distance to move in the x and/or y direction to find the sample surface. These values must be large enough to span

the radius of the well surrounding the pillar, and moving in either direction by 35 – 50 μm is usually sufficient. Another parameter that must be changed from its default values is the allowable drift rate, the smallest rate, in nm/s, that the machine must register before the test starts. A drift rate of 0.1 nm/s was used for all microcompression tests. The pillars were compressed at a loading rate of 0.15 mN/s, making the strain rate ~10^{-4} /s, to a maximum depth that would equal ~8% strain. For example, a 10 μm tall pillar and a maximum depth of 800 nm would translate to ~ 8% strain. The final step is setting the location, though at this point only one test position at a time is possible. Compression tests on multiple pillars must be set up individually following completion of the previous test.

2.4.3 Data Analysis

During compression the systems records the load (mN) vs. displacement (nm) of the nanoindenter tip. This data is then used to obtain the true stress vs. strain plots. From the displacement data (Δl) and the original pillar height (l_o), engineering strain is calculated from equation 2.10. Since it is not possible to measure the instantaneous height of the pillar during testing the engineering strain is converted to true strain by equation 2.11. From the load (P) values and pillar area ($A = \pi r^2$) the engineering stress is calculated from, equation 2.12, and converted to true stress by equation 2.13 [1].

$$\varepsilon_{Eng} = \Delta l / l_o \qquad \text{equation 2.10}$$

$$\varepsilon_{True} = ln\left(1 + \left(\Delta l / l_o\right)\right) \qquad \text{equation 2.11}$$

$$\sigma_{Eng} = P / A \qquad \text{equation 2.12}$$

$$\sigma_{True} = \sigma_{Eng}\left(1 - \varepsilon_{Eng}\right) \qquad \text{equation 2.13}$$

Since there is no method to observe these pillars during a compression test and light microscopes do not have the resolution to see features on this scale, electron microscopy was used to observe the effects of testing. Following compression, SEM images were taken to observe any "macroscale" deformation behavior. However, the scale achieved by SEM images still only gives the bulk deformation behavior of the material. To observe the microstructural response to loading, and therefore determine the deformation mechanisms, TEM images must be taken of the tested pillars. Fabrication of a TEM lamella from a pillar was done using the FIB, first milling the entire pillar to a thin plate, ~5.0 μm wide and 1.0 μm thick, then lifting-out this plate and attaching it to a Cu TEM grid. The plate was thinned to electron transparency using the FIB, where the final thinning was done at 5.0 kV and 81 pA to remove any damage layer. TEM analysis included bright field (BF), dark field (DF), and select area diffraction patterns (SADP) of the tested pillars. Also, a NanoMegas ASTAR system at Drexel University was used to determine the orientation of the grains in these TEM lamellas [149]. This system uses a JEOL JEM 2100 microscope with a LaB_6 tip in nanobeam diffraction mode (i.e. spot size ~10 nm). At a single spot on the lamella, a single crystal diffraction pattern is created, captured by a CCD camera, and then analyzed to determine the grain orientation at this spot. The analysis is accomplished by matching the diffraction pattern to a bank file of expected single crystal diffraction patterns for the material. The beam was scanned over an area on the lamella ~715 x 520 nm with a 6.5 nm step size, allowing for the build-up of an orientation map, similar to those seen in Electron Backscatter Diffraction (EBSD).

2.5 Microtension

Tensile tests must be done in order to properly determine the ductility, elastic modulus, and strength of NC Ta. However, due to the reduced dimensions of the HPT disk and the inherent grain size gradient, smaller tensile specimens and a custom built testing stage are needed. All of the tensile specimens are fabricated on the half disk of HPT Ta and testing is done via *in-situ* testing system in a scanning electron microscopy.

2.5.1 Fabrication of specimens

FIB milling was used to fabricate the tensile specimens from HPT Ta. Like the compression tests, HPT tensile specimens were fabricated at various radial positions. Although the material of interest is HPT Ta, there is a limited amount of this material. Therefore, thin foils, ~15 μm thickness, of coarse grain Ta were first used to characterize the *in-situ* SEM stage, sample design, and testing parameters.

Tensile specimen fabrication from the Ta foil or HPT Ta follows similar steps. However, the description below is concerned only with specimens from HPT Ta. These specimens begin by using μ-EDM to remove bulk regions of material, leaving only rectangular posts. This machining process uses a thin wire “tool” and material “part” that act as a cathode and anode of an electrical circuit. Both are submerged in a dielectric material, commonly deionized (DI) water, and an electrical current is passed through the wire. When the tool and the part are positioned in close proximity to each other, and provided that the part material is conductive, an electrical discharge, or spark, passes between them. This spark causes heating at the part surface to temperatures above the melting point of the material. This melted material is ejected, leaving behind a small channel on the order of the wire diameter. The HPT Ta posts are machined along the cut edge of the HPT disk starting at the center, out to the edge, as shown in FIGURE 2.9. An

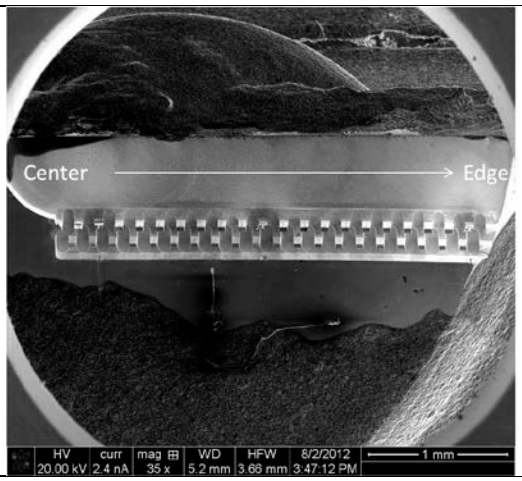

FIGURE 2.9: Low magnification SEM image of the HPT Ta half disk showing the μ-edm milled post along a single disk radius that act as precursors to the final tensile specimens.

SEM image of an individual post is shown in FIGURE 2.10a, which is ~100 μm tall, 55 μm wide, and 35 μm thick. μ-EDM helps reduce the amount of time spent making these specimens, since large area, bulk material removal with the FIB would take days, making *in-situ* SEM testing impractical.

The next step in tensile specimen fabrication is to thin the μ-EDM posts down to the desired gauge thickness. This was done using the FIB, and with the help of scripts similar to those used for compression pillars. The tension scripts used to fabricate specimens are part of "*AutoFrancis*". To start, a ~1.0 μm thick protective layer of platinum is added on to the top of the μ-EDM post. Into this layer a bull eye fiducial is milled with the following dimensions: outer circle: OD1 =5.0 μm, ID1 = 4.0 μm and inner circle: OD2 = 1.5 μm, ID2 = 0 μm. An example of this fiducial is shown in FIGURE 2.10b. Running the scripts, "*roughCutTension*" and "*tensionthinning*" thin the post in two steps. The first is a rough, fast milling at 30 kV and 21 nA to create a plate

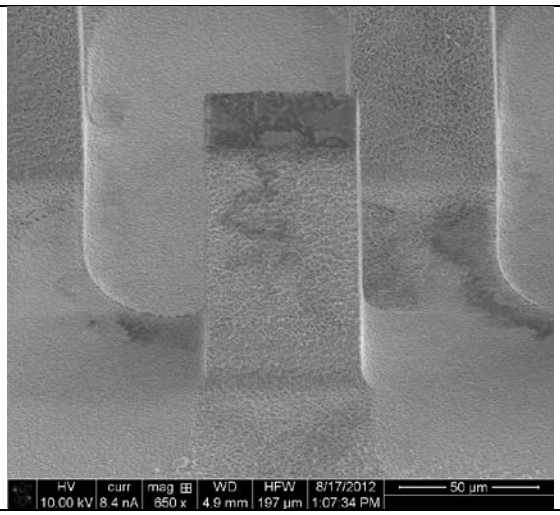

a)

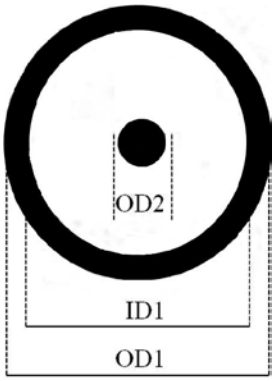

b)

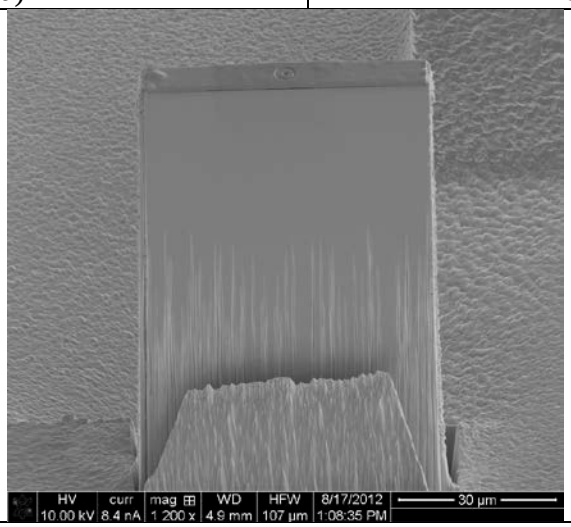

c)

FIGURE 2.10: (a) SEM image of a single µ-edm post that is approximately 55x35x100 µm. (b) The fiducial used during image matching of the thinning process, here OD1 =5.0 µm, ID1 = 4.0 µm, and inner circle: OD2 = 1 µm. (c) A final thinned plate that has a thickness that is equal to the desired specimen gauge thickness

with twice the desired gauge thickness. The second step is a finer, slower thinning process at 30 kV and 9.0/2.7 nA to end with a plate of the final desired gauge thickness, like that shown in FIGURE 2.10c. Regardless of which thinning script is used, the steps to achieve the final product involve tilting the stage by ± 1.5° about the normal to the ion beam to remove the inherent taper and positioning the milling boxes in reference to the location of the fiducial.

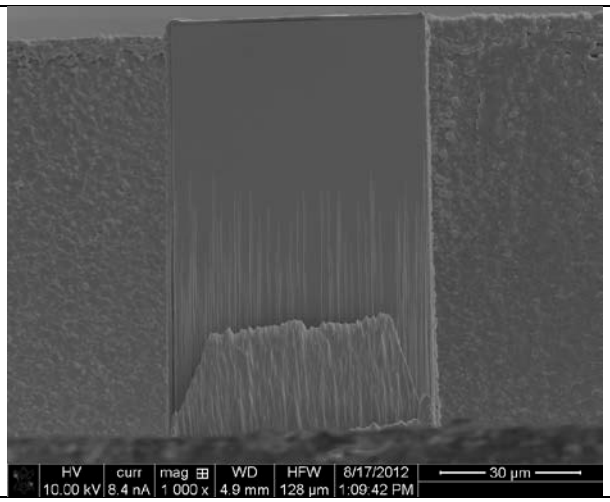

a)

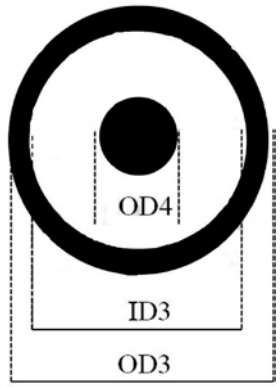

b)

c)

FIGURE 2.11: (a) SEM image of the thinned plate in plane-view for the final dog-bone milling (b) The fiducial used during image matching of the final milling process, here OD1 =5.0 µm, ID1 = 4.0 µm, and inner circle: OD2 = 1.5 µm. (c) An example of the bitmap used to mill the "dog-bone" shape into the plate. This bitmap corresponds to the stabilized free end and curved gauge section specimen.

Once the plate is at the desired thickness, it is positioned in plan-view with respect to the ion beam, shown in FIGURE 2.11a. A fiducial, like the one shown in FIGURE 2.11b, is milled onto the thinned plate by first depositing an 8.0 x 8.0 µm Pt pad that is 1.0 µm thick. Two concentric circles are milled into this pad where the first circle has the dimensions, OD3 = 5.0 µm, ID3 = 4.0 µm, and the second circle has OD4 = 1.5 µm. Milling the final tensile specimen was done by inserting a bitmap of the desired "dog-bone" pattern over the thinned plate, where only the white regions are milled. An example of a bit-map with a ~14 µm fillet radius and a ~200 µm radius on the gauge section is shown in FIGURE 2.11c, this is only half of the final specimen because the

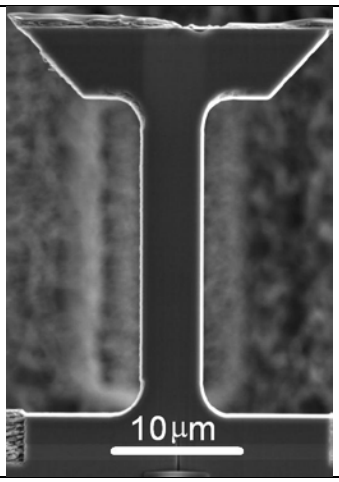

a)

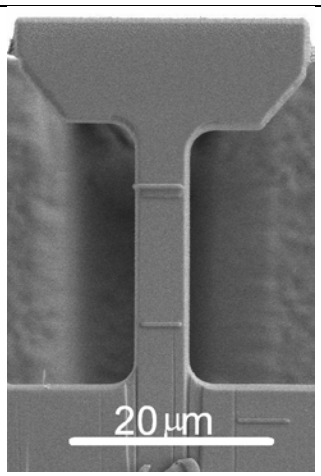

b)

c)

FIGURE 2.12: SEM images showing the three tensile specimen designs used for Ta foil testing, the successful design will be used for the HPT Ta specimens. (a) Specimen with no stabilization on the free end and a straight gauge section. (b) Specimen with the addition of a stabilizing free end but still a straight gauge section. (c) Specimen containing both a stabilized end and ~200 μm curve on the gauge section.

script again tilts ± 1.5° about the normal to the ion beam to make sure there is no taper to the gauge section. Rotating the bitmap in FIGURE 2.11c by 180° about its horizontal axis mills the other half. Final specimen gauge widths available by using this script are: 2.5, 5.0, 8.0, and 15 μm. For this work the gauge thickness was kept constant at 8.0 μm in order to determine a specimen geometry that reliably produced deformation and failure inside the gauge section. Examples of the attempted geometries are shown in FIGURE 2.12a-c, where the main differences between them are: there is a thicker grip portion on the free end between FIGURE 2.12a and FIGURE 2.12b, and FIGURE 2.12c has the addition of a slight curvature to the gauge section.

In order to measure strain accurately there must be a way to measure the extension of the gauge section during testing. It is possible to calculate the engineering strain from displacement measurements but the system compliance must be removed to

get accurate values. As a more direct strain measurement Pt markers were deposited onto the gauge section using the electron beam. Platinum deposition from the electron beam is not as efficient as the ion beam, but this way damage to the sample is minimized. The markers were all ~1.0 μm thick but were either with varying line widths, or a grid of 100 nm diameter circles. All markers were deposited using a 10 kV, 8.4 nA electron beam.

2.5.2 Testing

An *in-situ* SEM testing stage was designed by Dr. Brian Schuster and Dr. William Sharpe Jr. to be used inside the FIB chamber. A diagram of this stage is shown in FIGURE 2.13a. It consists of an aluminum frame, sample positioning motors, linear actuator, and load cell. Three individual attocube© piezoelectric motors control sample positioning in the x, y, and z directions. All three motors step via a stick-slip mechanism but the x-axis has a maximum travel distance of 5.0 mm and step size of ~ 50 nm, while the y- and z-axis only have a 2.0 mm maximum travel and a 25 nm step size. The linear

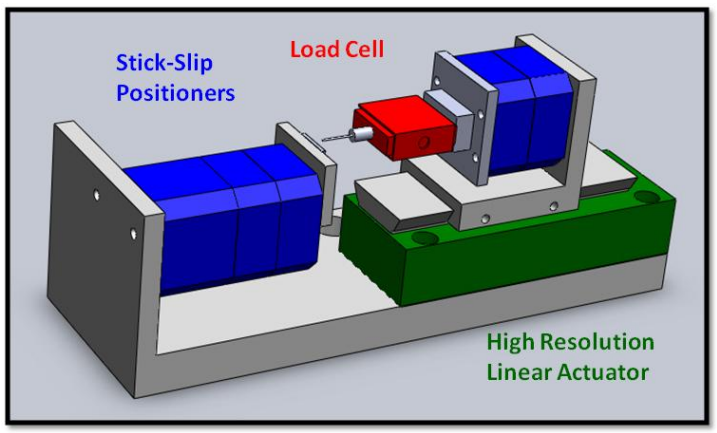

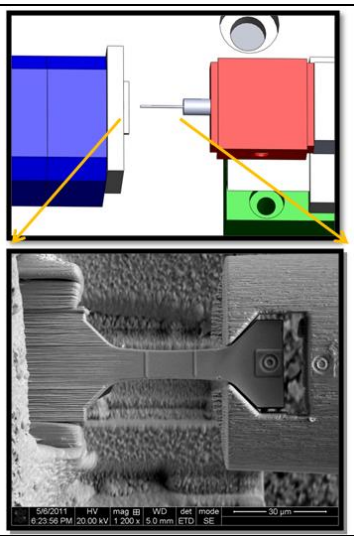

a) b)

FIGURE 2.13: (a) Solid works diagram of the *in-situ* SEM stage design, includes the piezo positioners (blue), load cell (red), and high resolution linear actuator (green). (b) Close up view on the grip-specimen portion of this stage, where the SEM image on the bottom shows a specimen loaded into a finished grip.

actuator is a high resolution nanopositioning stage from PI© with 38 μm of total travel and a resolution of 1.0 nm. Sitting on top of this linear actuator is a Futek© S-beam strain gauge based load cell, with a maximum load capacity of 100 g and resolution of 0.1 g.

These three components make up the bulk of the *in-situ* set-up but there must be a way to grip the specimen during the test. To do this, a tungsten needle was attached to the load cell, a schematic of which is shown in the top image of FIGURE 2.13b. At the end of this needle a grip is milled using the FIB through the entire thickness, FIGURE 2.13b bottom. This grip must be made specific to the tensile specimens, and specifically it must be wide enough to allow the free end of the specimen to pass through and the angled portion must match the angled section on the specimen. The script "*Tensilegrip*" will mill the angled portions to fulfill the latter requirement but the user must remove the rest of the material manually. To run this script, a bull eye fiducial must be created so that the center point is ~40 μm from the end of the needle. This fiducial has the same dimensions as the one used for the final specimen milling, FIGURE 2.11b.

Testing begins by positioning the free end of the specimen in the grip using the attocubes©. Using the x positioner, the specimen was moved into contact with the grip until the initial preload (L) is $0.5 \leq L \leq 1.0$ g. Once the specimen is loaded in the grip the actuator moves to apply the load. The actuator is controlled through a LabView program, shown in FIGURE 2.14, which allows the user to define the total number of data points, time of test in seconds, and actuator starting position and ending position. Number of points and time of test should be enough so that the step size over the total travel of the actuator is ~1.0 nm/sec. Parameters for tests performed in this work are summarized in TABLE 2.1, where tests lasted 1, 2, or 3 hours and the corresponding

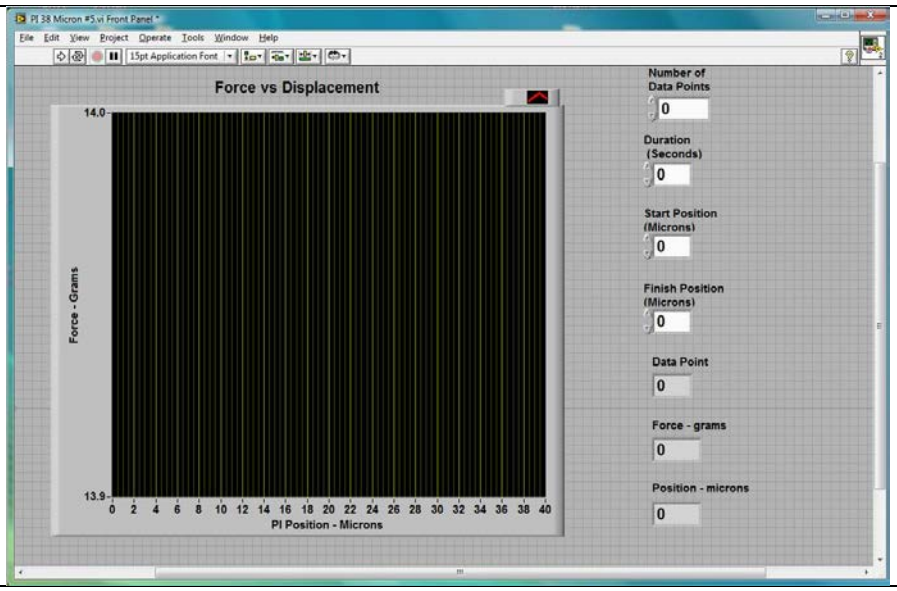

FIGURE 2.14: Screen shot of the LabView VI front panel used for *in-situ* tension testing. The user inputs values into the boxes for number of points, duration of test, and starting/finish position.

number of points and total travel make the step size ~2.0 nm/sec. During testing the LabView program records and outputs the load (grams), actuator position (μm), and time (sec).

To allow for the strain to be calculated, sequential SEM images of the gauge section, which contain the deposited Pt markers, were taken during testing. In order for accurate strain calculation there must be a high contrast between the Pt markers and the tensile specimen material. Proper contrast is achieved by altering electron beam imagingconditions such as the accelerating voltage, beam current, detector, dwell time, and resolution. Accelerating voltage and beam current were kept at either 5.0 kV/0.40 nA or 2.0 kV/81 pA. At these beam conditions both the Everhart-Thornley (ETD) and Through- the-Lens (TLD) detectors were used for imaging since they also affect the final images. Resolutions of 1024x884, 2098x1768, and 4096x3900 were used to determine the locations of the markers which allows for the most effective analysis during digital image correlation (DIC). The dwell time must be set at a level that allows for decent

signal acquisition by the detector but keeps the total imaging time short, and this has been set at 3.0 or 10 μs.

Once the proper beam conditions were determined, sequential image capture can be done by two methods. First, the software that controls the FIB has the ability to record images at set intervals under the present beam settings and to automatically save each image. This works nicely for resolutions of 1024x884 and 2098x1768 but will not function at the highest resolution. Also, there is no means to adjust the aspect ratio of the scan area, meaning there is still a large area of the scan that is not of the specimen. Time spent scanning across those regions is wasted since it is of no interest and the final images must be cropped down to include only the gauge section. Image capture software from 4Pi is used, which is a third party system that allows greater control over the image resolution and aspect ratio. Using this imaging software it is possible to cut the scan area down to include only the gauge section while still maintaining a resolution of 4096x1024 over this area, cutting down on the overall scan time at a specific dwell time. Unfortunately, this software does not have the ability to automatically capture and save sequential images. This means that the user would have to manually capture and save each image, and hence the tests span hours. Therefore, this would be an inefficient use of time. Using AutoIT, a freeware BASIC-like scripting language designed for automating Windows based actions, the image capture process can be automated [150]. AutoIT can

TABLE 2.1: Parameters used for tensile testing, each row corresponds to the necessary parameters need to achieve an actuator step size of ~2.0 nm.

Time (sec)	Number of Points	Travel (μm)
3600	10000	10
7200	20000	15
10800	30000	30

perform basic user actions, such as mouse clicks and keystrokes, to capture the SEM images and save them with the correct name. The AutoIt script used for image capture, via the 4Pi system, during testing is shown in Appendix B. As a note, regardless of the method for image capture the images must be saved in an 8-bit Tagged Image File Format (TIFF) because the grayscale levels improve the future data analysis.

2.5.3 Data Analysis

During testing the load on the tensile specimen is recorded, so it is easy to calculate the engineering stress (σ_{Eng}), in GPa, by using equation 2.14, where the load *(L)* is in grams, the gauge width (*w*) and thickness (*t*) are in microns and the constant, C = 9.8067 is used to convert grams into milli-newtons. From these values the true stress (σ_{True}) can be calculated by equation 2.15, but first the engineering strain (ε_{Eng}) must be calculated by a DIC program.

$$\sigma_{Eng} = (L \cdot C / g)/(w \cdot t) \qquad \text{equation 2.14}$$

$$\sigma_{True} = \sigma_{Eng}(\varepsilon_{Eng} + 1) \qquad \text{equation 2.15}$$

The DIC program used here is a suite of MATLAB© based codes developed by researchers at the Johns Hopkins University and is freely available through the MathWorks website [128, 151]. The goal of the DIC process is to produce a plot of strain vs. image number, but it first begins by extracting the capture time from each image which will be used later to match with the stress measurements. Strain measurements from the images were done by two different methods, both involve image correlation

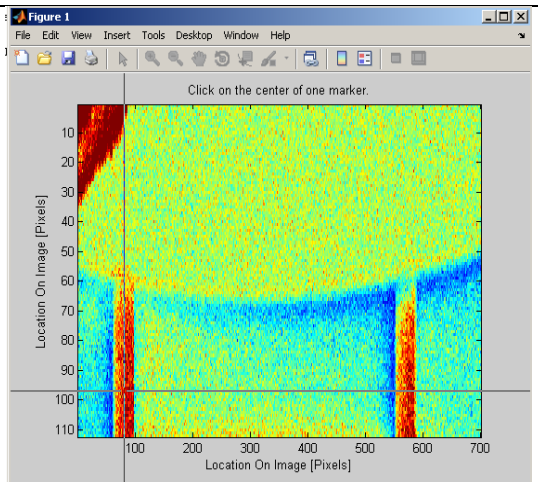

a) b)

FIGURE 2.15: Screens shots taken during the DIC strain analysis showing (a) the intensity map of the capture image and (b) the line profile. The peaks in (b), which represent the Pt markers, will be tracked between images to calculate the strain in each specimen.

tracking of intensity peaks and require that the displacement of the peaks between images is less than 10 pixels [152]. For the specimens with line Pt markers, a line profile tracking method is used. An intensity map of the image is displayed, where the dark red regions represent the markers, FIGURE 2.15a. A single line intensity profile is chosen by the user, FIGURE 2.15b. The data is fit to a gaussian function and the location of each peak is recorded, giving the distance between the peaks.

The program then cycles through each image locating, fitting, and recording the peak positions. From these positions the DIC software is able to build up a table of the engineering strain vs. image number for the test. The second method of calculating strain is to create a grid of points over the gauge section that will be tracked between images. This method works well for the circle Pt markers. Tracking of these points was done by determining a starting intensity value for each point from the first, reference image. On the next image a grid is formed around each point and the new intensity values are

matched to the reference value to determine any displacement. After analyzing all images a plot of true strain vs. image number is produced.

The final step of the tensile data analysis is to match the corresponding stress and strain values. Each point in the strain analysis corresponds to an SEM image and each image is time stamped during testing. Therefore, the MatLab program simply zeros all the time values and finds the corresponding strain and stress measurements for a given time. Since there are fewer strain measurements, this is the limiting factor in the number of total data points acquired during testing.

2.6 Ta Foil Microtension Results

Due to the limited amount of processed Ta available following HPT and the time needed to fabricate each tensile specimen, it is not effective to use this material to determine proper testing conditions. Instead, specimens fabricated from a 5000x5000x0.015 mm annealed Ta foil were used for determining the proper testing conditions. These conditions include the specimen design, e-beam settings, resolution, and magnification.

2.6.1 Specimen Design

Three different designs were used to determine which would provide specimens that reliably failed in the gauge section between the Pt strain markers. The main difference between these designs is the stabilization on the free end and amount of curvature in the gauge section. For the first design, which had no stabilization or curvature, the free end bent while in the grip. Adding a thicker section to the free end of the specimen, while still maintaining a straight gauge section, did not work either, as the specimen broke at the grip-specimen contact region, FIGURE 2.16a. The additional

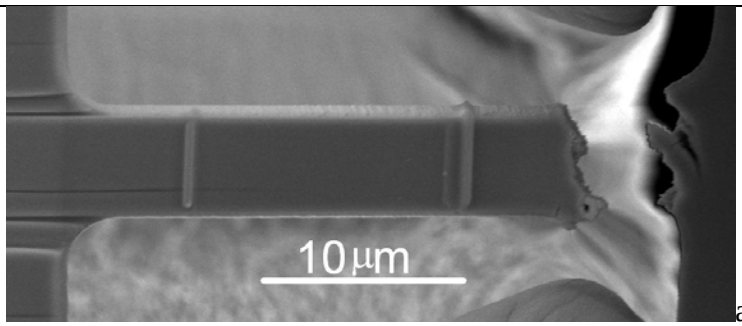

a)

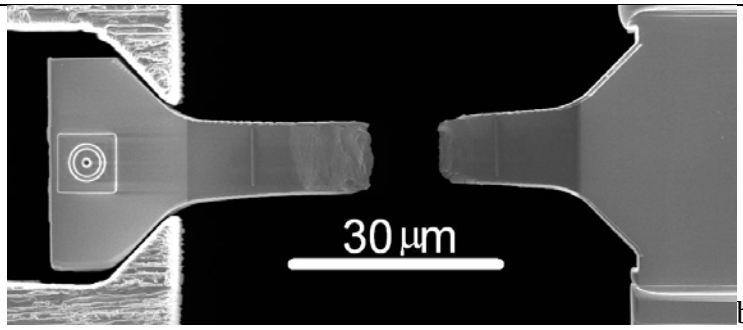

b)

FIGURE 2.16: SEM images of example tensile specimen designs showing (a) a failed design that had a stabilized free end and straight gauge section and (b) a successful design with a stabilized free end and curved gauge section. The second design geometry is used for all subsequent tensile tests.

stabilization may help but changes must be made to the gauge section to assure the highest stress occurs in the middle of this section. Taking guidance from the design used for metallic glasses, a ~200 μm radius of curvature was added to the gauge section. FIGURE 2.16b shows a failed sample with the addition of this curvature, which indicates that the specimen following this design fails in the gauge section between the Pt markers. This final design was used for multiple tests on the Ta foil and a Pd based metallic glass. All specimens of such design failed in the gauge section, and therefore, this design is used for all future tensile specimens.

2.6.2 Parameters for Accurate DIC

Accurately testing these tensile specimens requires reliably measuring the load and calculating the strain. Since the load measurements are made using the Futek© load cell, it is not difficult to calculate the stress values. Obtaining the strain values is more

difficult, as the tracking of Pt gauge markers must be done using DIC post-test. Effective DIC tracking is dependent on high quality SEM images, which starts with the Pt marker dimensions and the e-beam imaging parameters. Best DIC tracking is achieved when the contrast between the tensile specimen material and markers is high, so the end goal for the images is to have high intensity at the Pt markers and low intensity elsewhere. The SEM micrographs in FIGURE 2.17 show the effects of different marker dimensions, as defined in the FIB software. At various e-beam imaging parameters, deposition of all markers was done using the e-beam at 10 kV/8.4 nA to a max height of 1.0 μm. FIGURE 2.17a shows an image of 500 nm wide lines under imaging conditions of 2.0 kV/210 pA. While there appears to be two bright vertical strips at the marker positions, the line profile during DIC showed multiple peaks. Measuring the actual marker width gives ~800 nm, which is too wide to effectively run the DIC. Decreasing the line width to 200 nm and imaging at 2.0 kV/210 pA and 5 kV/0.40 nA, FIGURE 2.17b and c respectively, shows high brightness values over the whole image, which would be ineffective for DIC. However, it was noticed that the contrast/brightness would change once contact between the tensile specimen and grip was made at the start of testing. Using the previously defined marker dimensions, a specimen was put under a small amount of pre-load (~0.5g) and imaged at 5 kV/0.40 nA, shown in FIGURE 2.17d. This image shows a greatly improved contrast between the marker and specimen, but attempts to run the DIC matching had sporadic success. The actual width of these markers is ~400 nm, but reducing this dimension and imaging at 5 kV does improve the matching.

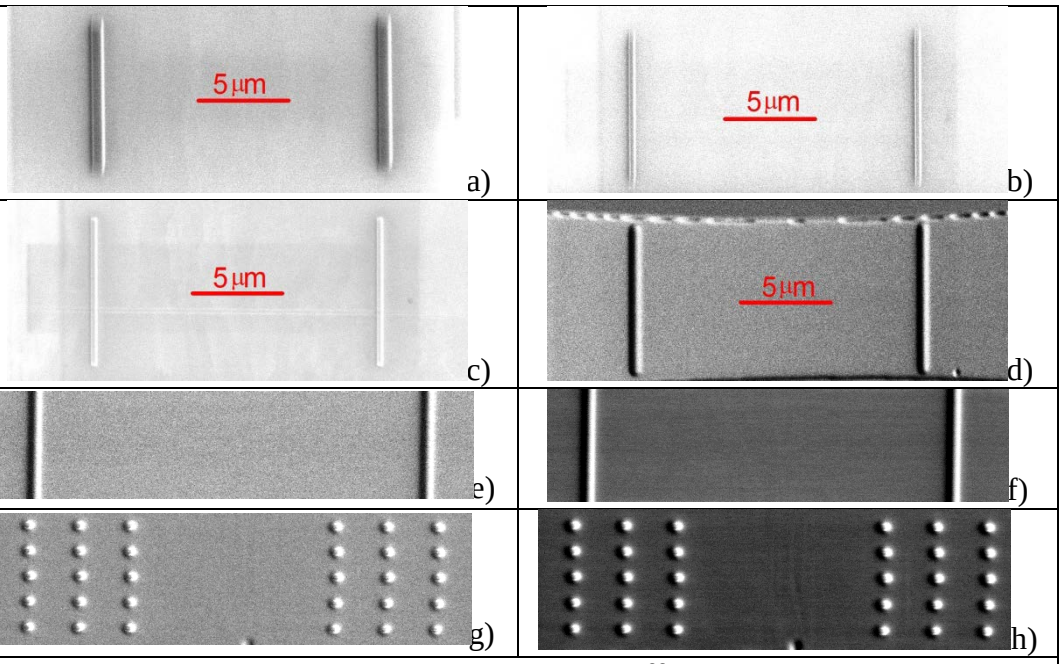

FIGURE 2.17: SEM images used to determine effective Pt marker dimensions and electron beam parameters for imaging. (a) 500 nm wide lines imaged under 2.0 kV/210 pA. (b, c) 200 nm wide lines imaged at 2.0 kV/210 pA and 5 kV/0.40 nA respectively. (d) 200 nm wide lines again imaged at 5 kV/0.40 nA but now under a ~0.5g pre-load that improves the contrast. (e – h) Line and circle markers imaged at 5 kV/0.40 nA and 10 kV/8.4 nA respectively. These final images achieved the best contrast and improved the ability to complete the DIC peak matching for tensile strain.

To determine if continuing to reduce the width improves the performance, Pt lines were used. The FIB software does not define a width for the line feature but observations give a thickness of ~400 nm, surprisingly close to that of the 200 nm wide patterns. FIGURE 2.17e and f show images of line Pt markers taken at 5 kV/0.40 nA and 10 kV/8.4 nA respectively. These line markers under either beam condition are effectively and accurately matched in each image, surprising considering that the marker size is similar to the 200 nm defined markers. This improvement in matching is attributed to the beam scanning during deposition. The beam follows a serpentine pattern during deposition of a rectangular pattern, but for a line pattern the beam only moves along one direction (i.e., vertical). The serpentine scan results in two lines for each marker that show up as

separate peaks during the line scan while the line scan creates only a single line. The final images, FIGURE 2.17g and h, show 100 nm diameter circle markers at 5 kV/0.40 nA and 10 kV/8.4 nA respectively. As a note, all images were taken using the Everhart-Thornley (ETD) detector to take advantage of the "shadowing" effect. The microscope does have an additional detector, Through-the-Lens (TLD), but the DIC did not work properly for images taken using this detector. From this study the most effective marker dimensions were determined, and therefore, all the specimens shown from now on will have either line or circle markers that are ~1.0 μm thick and imaging will be done at 5 kV/0.40 nA using the ETD.

Other factors influencing the image quality, and consequently the DIC matching, are image resolution and magnification. These two parameters affect the physical distance on the specimen represented by each pixel. FIGURE 2.18a and b shows true stress vs. strain plots for tests on specimens where the resolution is kept constant at 1024x884 but the magnification was set to 3500X and 5000X respectively. The plot for 3500X, FIGURE 2.18a, is not ideal. Strain values were first calculated to be negative and the scatter between successive strain points is ~0.002. A small number of pixels spanned the width of the markers for this test, meaning the physical area represented by each pixel was large. This means the scatter here is most likely due to shifts in the individual pixel representing the peak intensity during the DIC line profile scan.

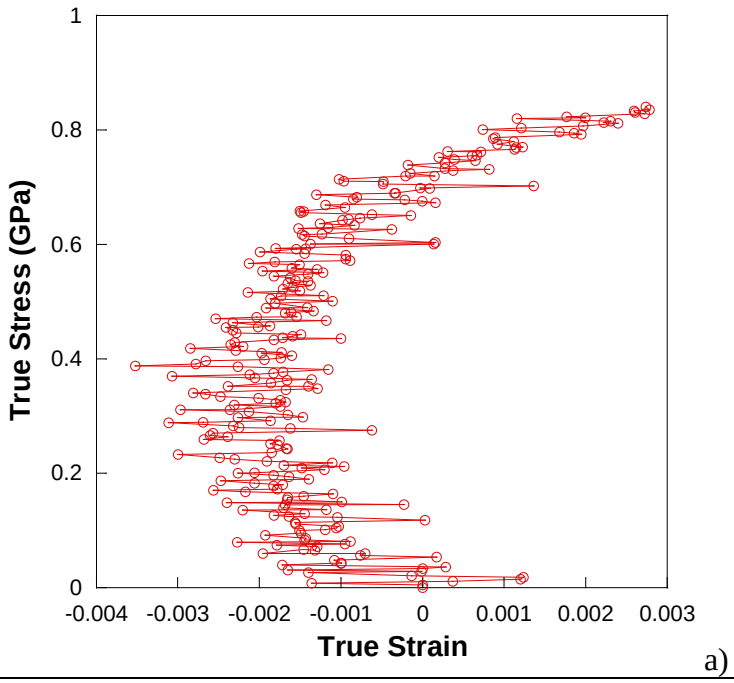

a)

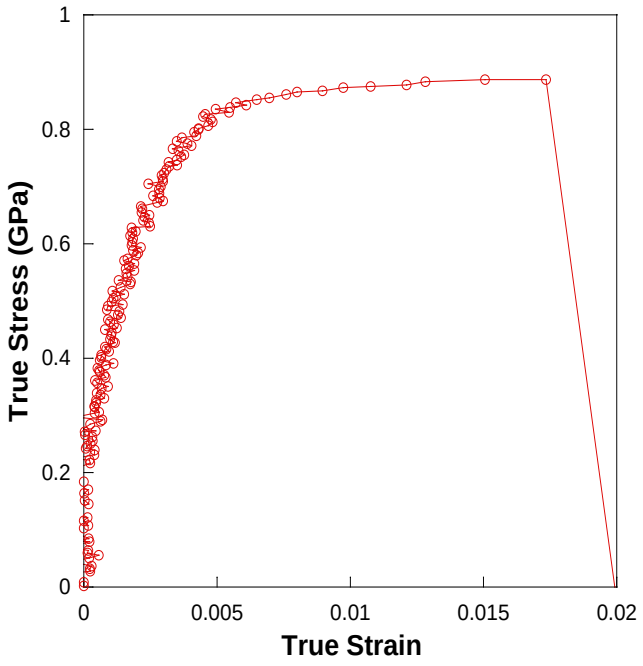

b)

FIGURE 2.18: True stress vs. strain curves for Ta specimens where the SEM images were taken at the same resolution, 1024x884 but changing the magnification from (a) 3500X to (b) 5000X. At the lower magnification the scatter in the strain values is due to the limited number of pixels spanning the width of a Pt marker. A great improvement in the curve is seen when the magnification is increased, allowing for a smaller physical distance to be represented by each pixel.

Increasing the magnification to 5000X increases the number of pixels that span the marker, decreasing the physical distance each one represents. The true stress vs. strain plot, FIGURE 2.18b, shows that increasing the magnification greatly improves the strain matching. Unfortunately, this is the limit to the magnification level as at any higher magnification the markers will no longer be in the field of view. Therefore, further improving the strain matching must be done by changing the image resolution.

A higher resolution also means a smaller portion of the specimen is represented in each pixel, which results in a more accurate DIC strain matching. It should now be noted that the dwell time must be long enough to get a decent signal to noise ratio during scanning, and is usually set to 3.0 or 10 μs. For these dwell times, imaging at a higher resolution means an increase in the total time to take an image, making it more likely to miss critical plastic events during testing. FIGURE 2.19a shows a true stress vs. strain plot for a specimen that was tested with the same imaging parameters as FIGURE 2.18b. Unlike the previous test, this plot shows scattering in the strain data, suggesting these parameters are not optimum. For the next test, the magnification is kept the same but the resolution is increased to 2048x1768, giving the plot shown in FIGURE 2.19b. This increase in resolution greatly improved the quality of the strain data, as there is less scatter in the data and the elastic modulus is measured as 170 GPa, close to the accepted modulus of 186 GPa for bulk tantalum.

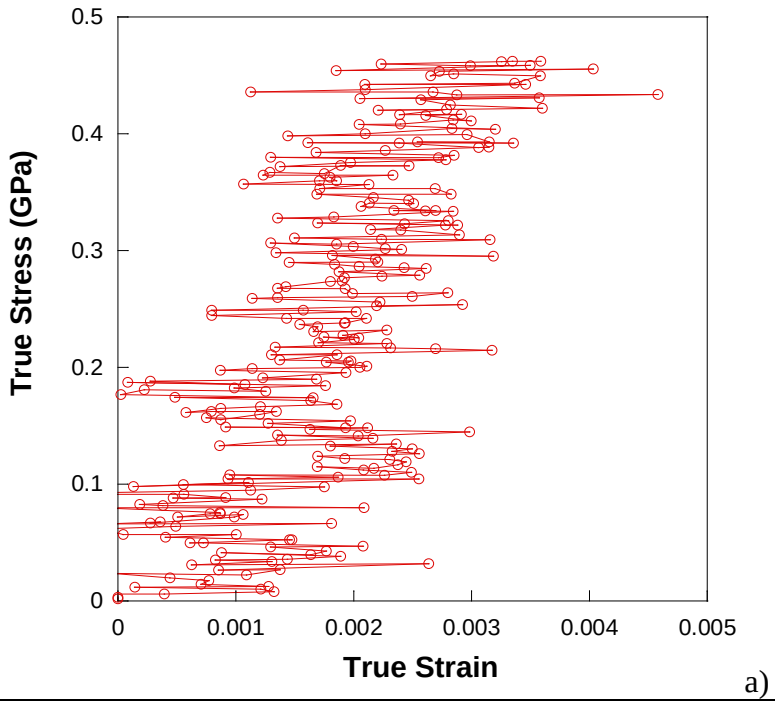

a)

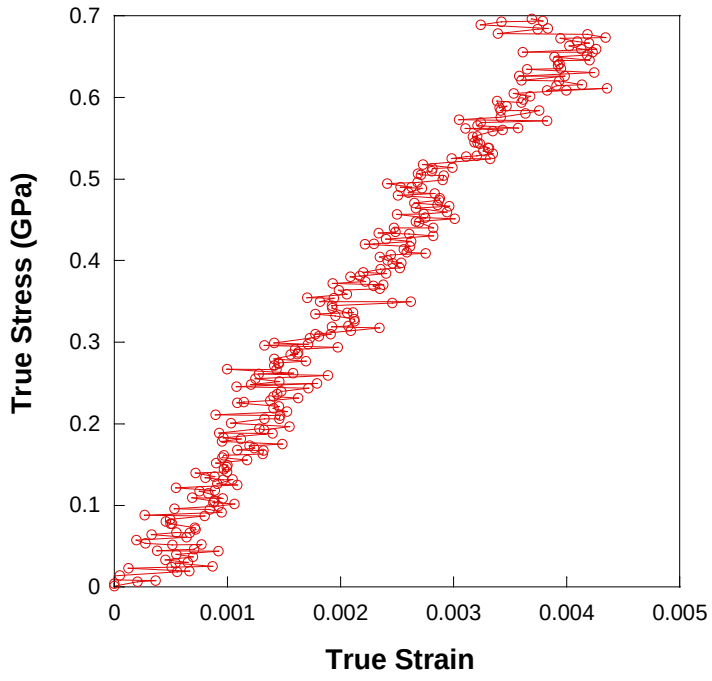

b)

FIGURE 2.19: True stress vs. strain curves for an elastically tested Ta specimen where images were taken at 5000X but the resolution was changed from (a) 1024x884 to (b) 2048x1768. The lower resolution shows a linear curve but too much scatter in the strain data. Increasing the resolution greatly reduces this scatter but the elastic modulus is still low.

Increasing the resolution to the next allowable level, 4096x3986, presents a few technical difficulties. The first is that at this resolution the time to acquire an image is two minutes, mostly due to the excess area scanned that is not part of the gauge section. At a magnification of 5000X a majority of the image area still consists of open space or specimen regions that are not the gauge section. It would be advantageous to be able to control the aspect ratio of the scan to only include the gauge section. The second problem is that the automatic image capture software provided by FEI does not work at this resolution.

To overcome these two problems, a third party imaging software from 4Pi was used to acquire high resolution SEM images with a reduced scan area that only includes the tensile gauge section. To automate the image capture, a script was written for AutoIT [150], which uses a Basic type language to perform simple user actions in Windows based programs. The program written for the image capture is shown in Appendix B, FIGURE B. 12.

Using this new image capture software, a specimen was tested using the following parameters. The specimen design was the type defined in section 2.6.1, where the free end was stabilized, and the gauge section had a 200 μm radius of curvature, and lines were used for the Pt markers. Imaging was done with the e-beam settings at 5 kV/0.40 nA, magnification at 5000X and the resolution set to 4096x1024. The result from this test is shown in FIGURE 2.20a and b. Here the true stress vs. strain plot shows a well-defined elastic regime that transitions to plastic deformation following yielding. In this plot the elastic modulus is measured as 189 GPa. Also from this plot, the yield stress is determined to be 725 MPa with ~1.0% tensile elongation. The accurate determination of

the elastic modulus confirms that these are the optimum conditions for accurate tensile testing.

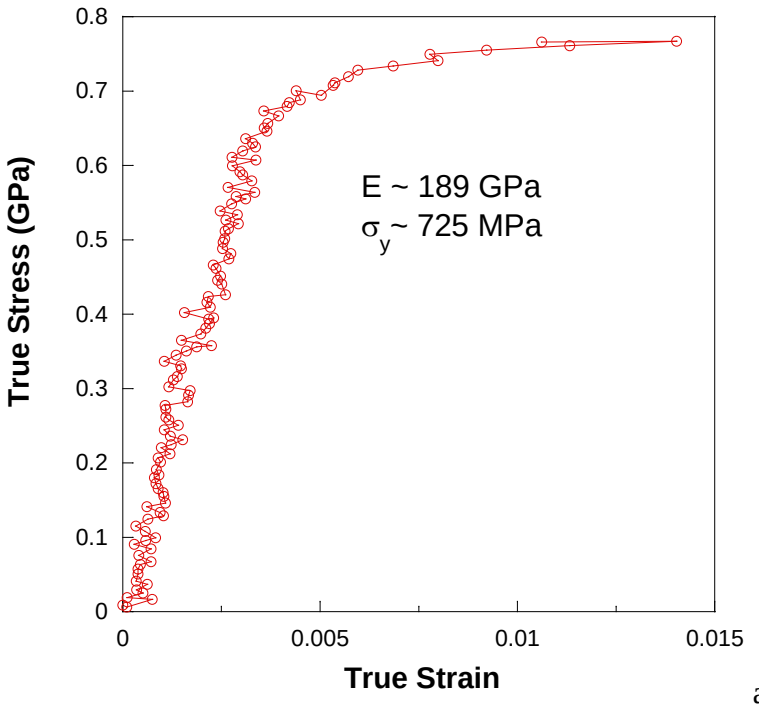

a)

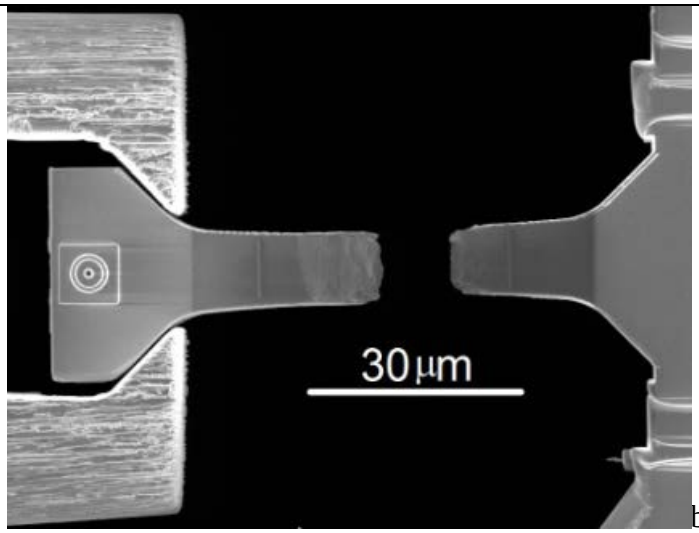

b)

FIGURE 2.20: (a) True stress vs. strain curve for a Ta specimen imaged at 5000X and a resolution of 4096x1024. These conditions produced a curve that shows a clear elastic region with a modulus near the accepted value and a transition to the plastic region near 700 MPa. (b) Failed specimen tested under the above conditions showing failure in the gauge section.

2.7 Summary

A Ta disk that is ~ 12 mm in diameter and 1 – 2 mm thick was processed by HPT under 5 GPa and N = 5 platen turns, producing a grain size gradient that varies from UFG to NC as the radial position on the disk increases. In order to quantify this grain size gradient, both TEM and SXRD based texture analysis are done on the disk. TEM lamellas were taken in three different orientations, with respect to the HPT torsion strain, at multiple radial positions to allow for a 3-D representation of the grain shape and structure. Grain size measurements at each location were also made from these TEM images. With only small volumes of processed material, the effects of grain size on mechanical properties were determined using microscale mechanical testing techniques. These techniques included nanoindentation, microcompression, and microtension. Nanoindentation was used to determine the changes in hardness, elastic modulus and strain rate sensitivity with position. Using a FIB microscope, microcompression pillars with diameters ranging from 5 – 10 μm were fabricated at multiple positions. These pillars were compressed using a nanoindenter system outfitted with a flat punch tip at quasi-static strain rates (10^{-4}/s) up to strains of 8 – 12%. Following testing, the resulting deformation behavior was observed using SEM images. TEM lamellas were also taken of these tested pillars to observe the plastic deformation mechanisms in NC Ta. Microtensile specimens with 8.0 μm wide gauge sections were also fabricated using the FIB and tested with a custom built *in-situ* SEM testing stage. For this testing set-up sequential SEM images of the specimen gauge section which are then used to calculate the strain during testing.

Due to the limited volume of HPT processed Ta, testing on Ta foils was done to determine proper testing specifics such as specimen design, Pt marker dimensions, and imaging parameters. An effective specimen design includes both a longer grip portion for stabilization and a curved gauge section to localize the stress between the Pt markers. These markers allow for the best DIC matching when they are thin lines or small diameter circles and imaged under e-beam settings of 5 kV/0.40 nA with a dwell time of 10 μs. Using these parameters, the elastic modulus for the coarse-grain polycrystalline Ta foil specimens was measured as 189 GPa, which is within 3.0 GPa of the accepted modulus. These parameters give acceptable results of the mechanical properties of the specimens and, therefore, are used when testing NC Ta or any other desired material.

CHAPTER 3: MICROSTRUCTURE AND TEXTURE ANALYSIS

3.1 Introduction

As was discussed previously, during HPT processing the induced strain varies with the position in the disk, following equation 2.2 [31]. Due to this fact, there is the possibility for a grain size gradient in the disk. The focus of this chapter is to present and discuss the results obtained from TEM and SXRD studies which were focused on the grain structure and texture analysis respectively. Using the FIB, TEM lamellas were taken from multiple positions on the disk and at each location along orientations parallel, perpendicular, and normal to HPT strain direction, allowing for a three-dimensional representation of the microstructure. Using a JEOL 2100F microscope, BF/DF images and SAED patterns were obtained. Site specific, through thickness texture analysis can be accomplished by utilizing the small spot size and high energy of the synchrotron x-ray source at Argonne National Laboratory. Two-dimensional Debye-Scherrer patterns were collected at multiple locations and sample tilt angles. The MAUD software was used to calculated the reconstructed (110) pole figures and crystallite sizes. This analysis will give a good description of the disk's microstructure, which can then be used to explain the observed mechanical properties presented in the following chapters.

3.2 Microstructure Analysis

3.2.1 X-Ray Analysis

FIGURE 3.1a and b show the 2-D Debye-Scherrer (D-S) patterns taken at ω = 0° for locations X = 1.0 and 5.4 mm, respectively. At X = 1.0 mm, only the {200} diffraction ring is not continuous. At the same sample orientation, the D-S pattern from X = 5.4 mm shows that all diffraction rings are continuous. This change in intensity indicates there could be a texture change within the disk but pole figures must be calculated to determine this quantitatively. Line profiles from the D-S patterns taken at ω = 0° for locations X = 1.2, 3.2 and 5.4 mm are shown in FIGURE 3.1c. The measured peaks are indexed and labeled and all correspond to the allowed reflections for BCC Ta, showing that no phase transformation to a body-center tetragonal (BCT) or other phases occurs during processing.

Using MAUD the (110) pole figures for X= 1.2 mm and X = 5.4 mm were calculated and are shown in FIGURE 3.2a and b respectively. These show that there is a weak shear deformation texture formed during HPT processing. For X = 1.2 mm the maximum texture intensity, $\mathbf{I}_{\mathrm{Max}}$ = 2.26 mrd, here mrd stands for multiples of random distribution where 1.0 mrd is considered a random texture. This weak texture is surprising considering that texture from ECAP processing can reach levels of greater than 5.0 mrd [153] and the strains achieved during HPT are much higher. The (110) pole figure measured at X = 5.4 mm shows a similar shear texture to the previous location, but here $\mathbf{I}_{\mathrm{Max}}$ = 2.4 mrd. This slight increase in texture strength can be expected due to the increase in strain between the two locations, but is still considered a weak texture. Previous texture measurements on HPT processed Cu also show this shear deformation

texture and gives I_{Max} = 2.58 mrd at the farthest radial position measured [33]. These results show that a strong texture does not form during HPT and that there is no change between positions.

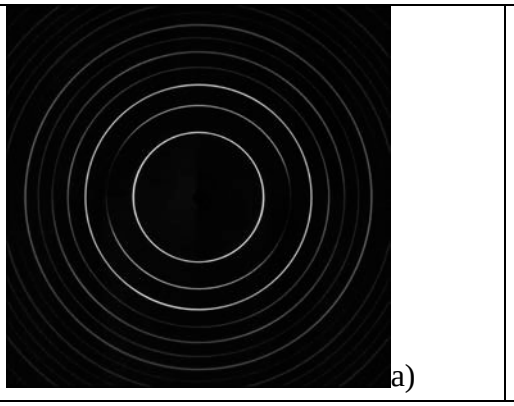
a)

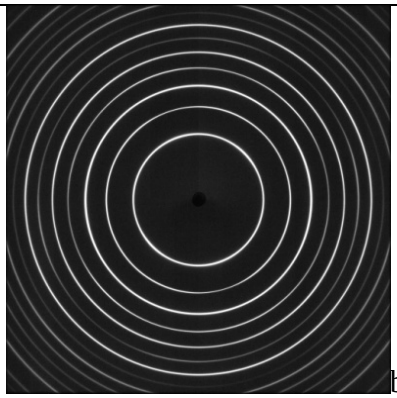
b)

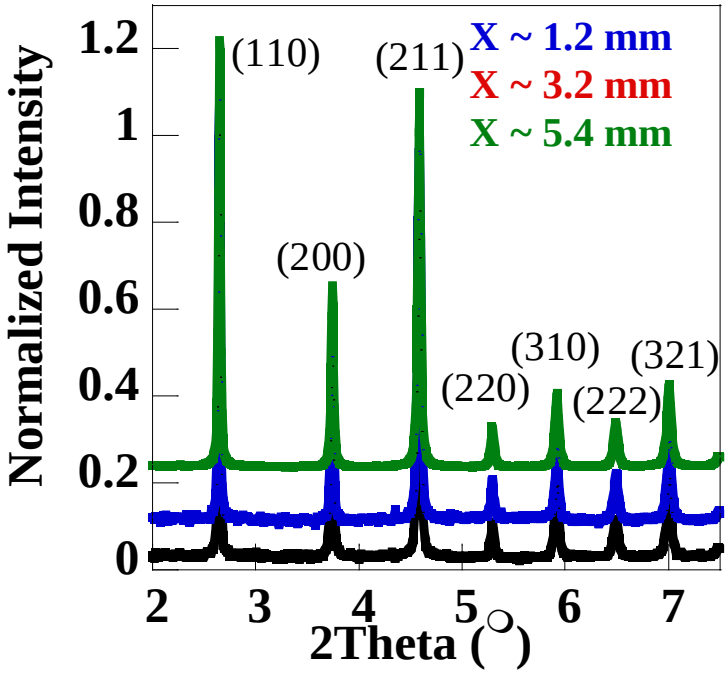

c)

FIGURE 3.1: 2-D Debye-Scherrer patterns for (a) X = 1.0 mm and (b) X = 5.4 mm at a stage tilt of ω = 0°. For X = 1.0 mm, the second ring shows some intensity changes but most of the rings are continuous. At X = 5.4 mm all the diffraction rings show continuous rings. (c) XRD line profiles taken from the 2-D patterns for ω = 0° at locations X = 1.2, 3.2, and 5.4 mm. All peaks are indexed as BCC Ta, indicating that no pressure or strain induced phase change occurs.

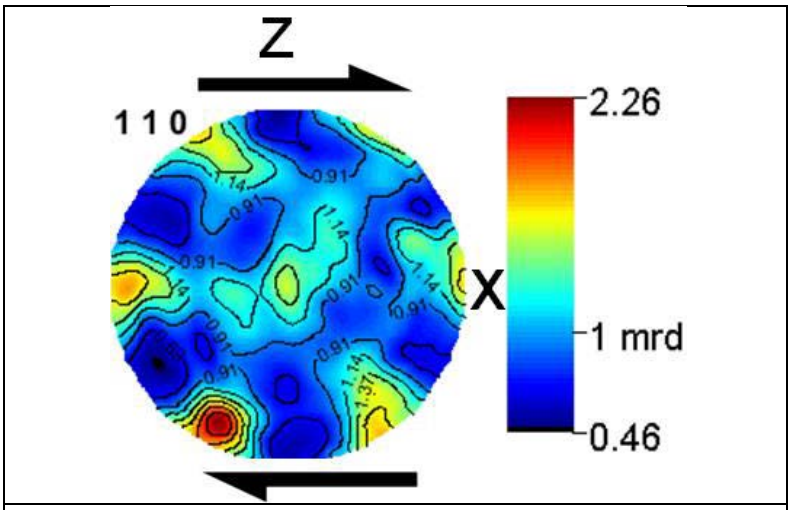

a)

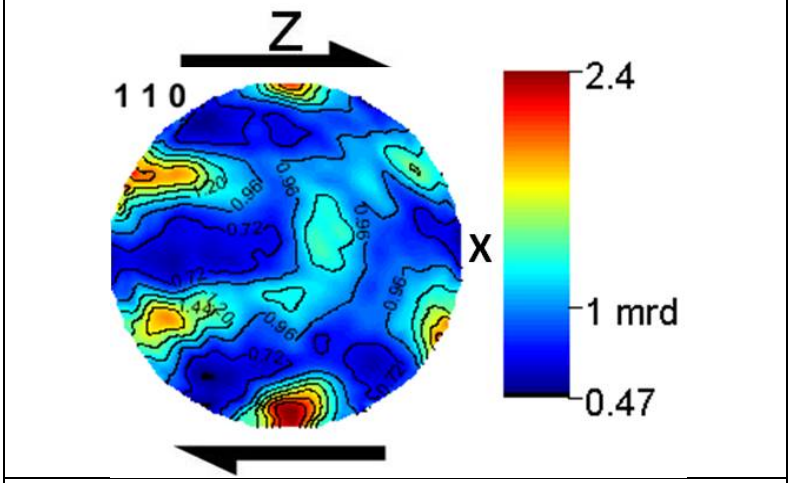

b)

FIGURE 3.2: (110) pole figures for z-x plane of HPT processed Ta at (a) X = 1.2 and (b) 5.4 mm calculated from MAUD. Both locations show similar intensity patterns and low texture intensity, ~ 2.0 mrd, considering the high strains achieved during HPT.

3.2.2 TEM Analysis

FIGURE 3.3a – f show BF and DF TEM images with inset SAED patterns from X = 5.3 mm. From these images it is easy to see how the HPT processing affects the grain shape. Lamellas taken along the normal and torsion direction are elongated along the

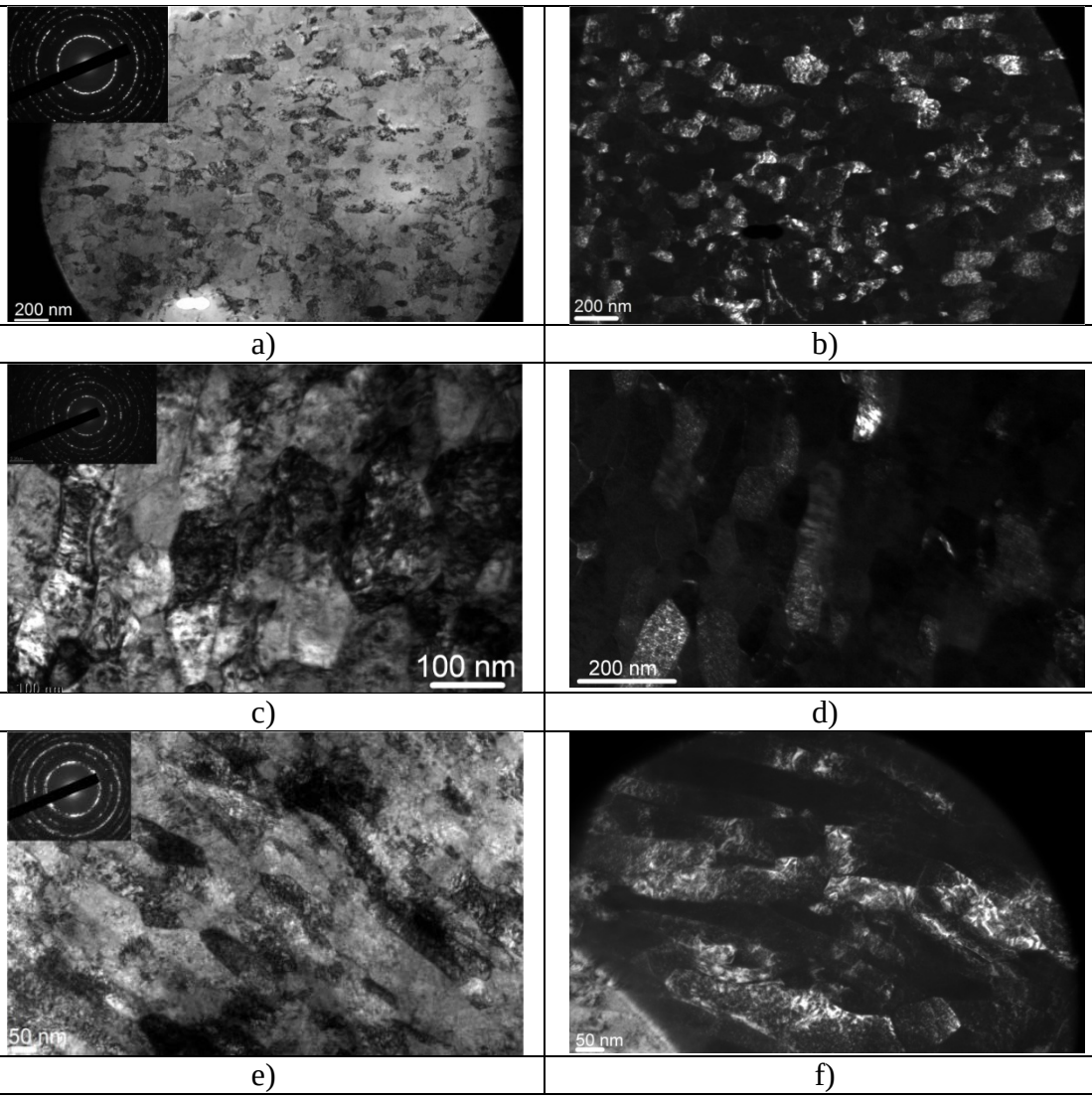

FIGURE 3.3: TEM images from lamellas taken at X = 5.3 mm. (a,c,e) Bright field and inset SAED patterns for radial, normal, and torsion orientations respectively. (b,d,f) Corresponding dark field images from the same bright field orientations. These show how the grain shape changes with respect to the HPT torsion strain, where along the direction of strain (ie. normal and torsion) the grains are elongated.

direction of strain during HPT, FIGURE 3.3c – f. However, in the radial orientation the grains are smaller and equiaxed, FIGURE 3.3a and b. The effects of the processing are also seen in the TEM images for X = 5.9 mm, FIGURE 3.4a – f. Regardless of the location where the lamella was taken, the grains show well defined boundaries, evidence of high angle type boundaries, and a heavily dislocated grain interior due to the extreme

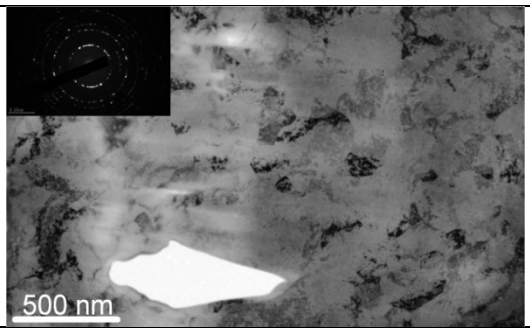

a)

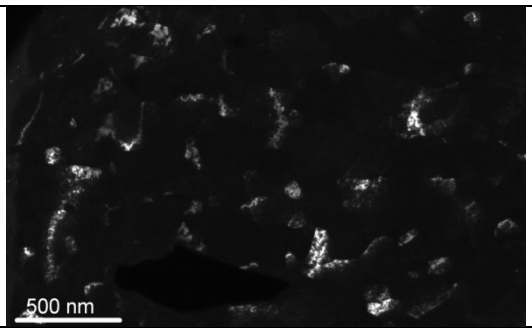

b)

c)

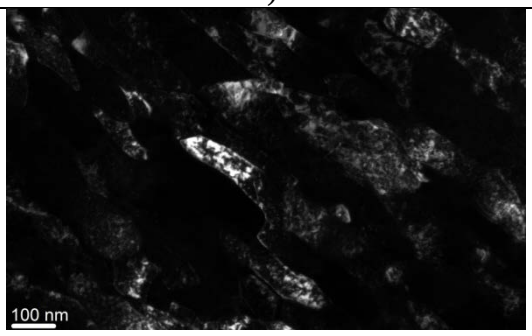

d)

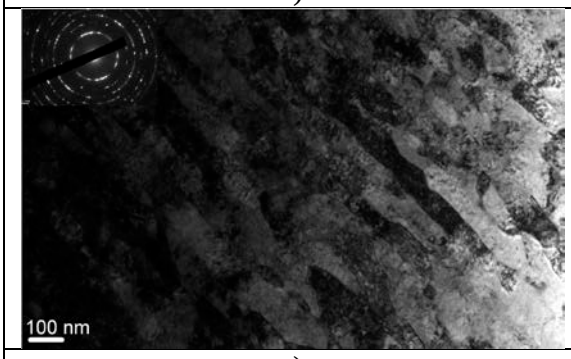

e)

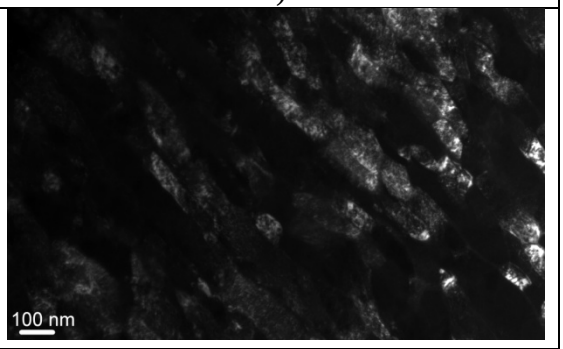

f)

FIGURE 3.4: TEM images from lamellas taken at X = 5.9 mm. (a,c,e) Bright field and inset SAED patterns for radial, normal, and torsion orientations respectively. (b,d,f) Corresponding dark field images from the same bright field orientations. These also show how the grain shape changes with respect to the HPT torsion strain, where along the direction of strain (ie. normal and torsion) the grains are elongated.

deformation during HPT [39]. The inset SAED patterns show mostly continuous rings for all locations, which suggests a small grain size and high angle grain boundaries in these lamellas. A few diffraction rings, {110} and {200}, show intensity changes which suggests there could be a slight texture in the grains. The diffracted beam from the {211} ring was chosen to acquire the corresponding DF images, FIGURE 3.3b, d, f and

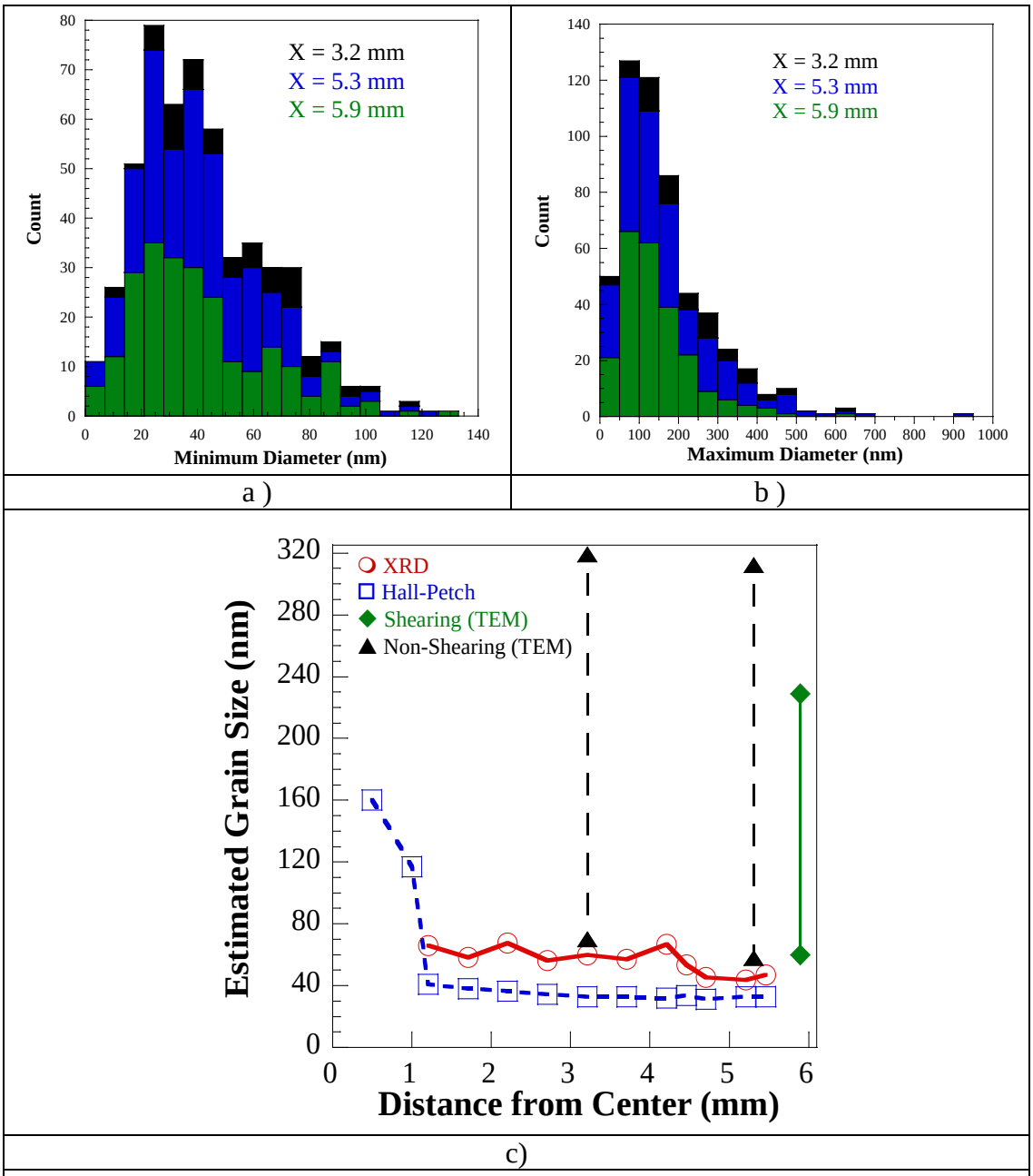

FIGURE 3.5: Grain size histograms for (a) minimum and (b) maximum diameters for locations X = 3.0, 5.3, and 5.9 mm. (c) Area weighted average grain sizes for the same locations. The minimum diameters for all measurements are consistently below 100 nm at all positions but the maximum diameter appears to shrink at the disk edge.

FIGURE 3.4 b, d, f. Individual grains are observed contributing to the overall image, indicating that the transmitted beam encountered separate orientations between grains. These images also show the heavily dislocated structure inside the grains at all locations and orientations.

3.2.3 Grain size

FIGURE 3.5a and b show grain size histograms for the minimum and maximum diameter respectively at all measured locations. The plot for minimum diameter shows that, in this orientation, the grains are well within the NC regime for each location. Values for the maximum diameter give mainly sizes in the UFG regime. However, these plots do not easily show the difference in grain size between regions. Measurements for grain size obtained from the TEM images, XRD peak broadening, and hardness values are plotted together in FIGURE 3.5c. The red curve corresponds to the XRD crystallite sizes calculated using the MAUD program. These measurements show the decrease in grain size with increasing radial position and are consistently in the NC regime. Grain size estimates from the hardness values correspond to blue curve in FIGURE 3.5c, also showing a reduction with increasing position. The vertical lines in this plot represent the area weighted average grain size for the minimum and maximum diameters at X = 3.0, 5.3, and 5.9 mm. With these plots the change in grain size between each location can be seen. The minimum diameters in each region are comparable for all techniques, varying from 40 – 70 nm, but for the elongated direction there is a decrease in the diameter at the disk edge. For the locations X = 3.0 and 5.3 mm the average area weighted grain size is 310 – 320 nm, but at X = 5.9 mm this value drops to ~230 nm. FIGURE 3.6, which shows the cumulative area fraction plots for each location, gives a better idea of how the grain size changes with position. A given ordinate value for this plot represents the percentage of grains that have a measured area fraction smaller than the corresponding

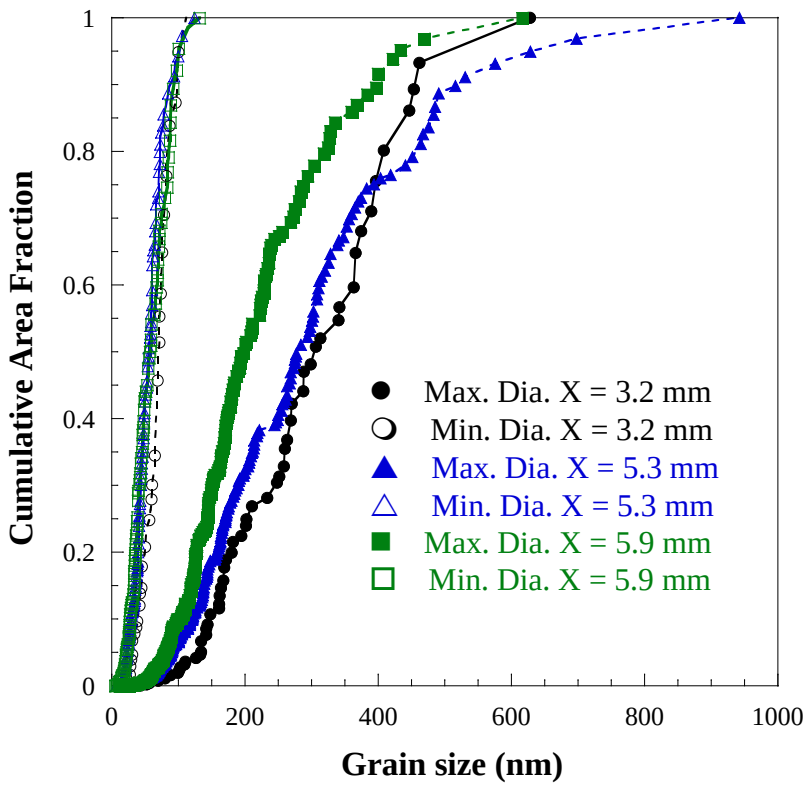

FIGURE 3.6: Cumulative area function plots for the minimum and maximum diameters at all measured locations. Again all the minimum diameters show similar grain sizes while the maximum diameter shows a shift toward smaller sizes at X = 5.9 mm. The shift to smaller grain size could affect the mechanical properties of NC Ta.

grain size value along the abscissa. Again, these plots show that the minimum diameter is fairly consistent at all locations. A basic "T-test" shows that at X = 5.9 mm, half of the measured grains have a maximum diameter smaller than 197 nm. However, at X = 3.0 and 5.3 mm the maximum diameter values at a cumulative area fraction of 0.5 increase to 300 and 280 nm, respectively.

3.3 Summary and Conclusions

The TEM and SXRD analysis presented above shows the results of the HPT processing. X-ray studies show that only BCC Ta is present in the disk, meaning any observed mechanical behavior can be related back to the expected behavior for BCC

metals. Texture analysis and calculation of (110) pole figures show a similar shearing texture at all measured locations on the disk. These pole figures have a low level of maximum texture intensity, ~2.5 mrd, where 1.0 mrd is considered random. The consistency between locations is evidence of the homogenous deformation strain direction during HPT processing.

Due to the consistent strain direction, all locations show an elongated grain shape, where the elongated (maximum) diameter is along the direction of HPT strain and is in the UFG regime. Perpendicular to the HPT strain the grain diameter is well within the NC regime. The different measurement techniques show that this minimum diameter is fairly consistent between all locations, 60 – 70 nm. However, area weighted average measurements taken from TEM images show that at the disk edge there is a drop in the maximum diameter by ~80 nm. The cumulative area fraction plots also confirm this, where a shift toward a smaller size is observed for the position at the disk edge, meaning the grains in this region are more equiaxed than the closer positions. This change in the grain size and shape could influence the resulting mechanical behavior.

CHAPTER 4: MICROMECHANCIAL TESTING RESULTS

4.1 Introduction

HPT processing only produces a small volume of material, making it difficult to use conventional testing techniques to determine mechanical properties. Also, as was shown in the previous chapter, there is a microstructure gradient present in the disk. It would be advantageous to perform tests on small volumes to ensure a homogeneous grain size and decrease the total amount of processed material needed. This can be accomplished using micromechanical techniques like nanoindentation, microcompression and microtension. This chapter is focused on presenting the results of these testing techniques.

Since tests will be performed at multiple locations on a single sample, determination between tests will be done by indicating the position (X) where that test was done. For nanoindentation studies, the interest is in how the values for hardness, elastic modulus, and strain rate sensitivity change with position over the entire disk. However, results for microcompression and microtension are separated into two main regions of the HPT processed disk, $X < 5.3$ mm (non-shearing region), and $X > 5.3$ mm (shearing region). The main reason for this separation is the transition to localized plastic deformation, in the form of shear bands, for both tension and compression at locations $X > 5.3$ mm. Reasons for this transition along with some other observed mechanical behavior like evidence of microplasticity, a reduced elastic modulus, and an increased

presence of a tension-compression asymmetry are investigated but will be presented in the next chapter.

4.2 Nanoindentation Results

4.2.1 Hardness

FIGURE 4.1 shows the hardness and modulus profile along the radius of the disk. Hardness values are low near the center of the disk, ~2.5 GPa at X ~1.0 mm, and this is expected since the grains should still be considered either coarse or in the upper UFG regime. Farther away from the center however the hardness begins to increase rapidly up to ~4.5 GPa at X ~ 2.0 mm, suggesting that in this region the grains are in the NC regime. Past this point on the disk the hardness saturates, and this occurs because of saturation in the grain refinement [154]. Also shown in FIGURE 4.1 are the elastic modulus values at each position. There is scatter in the modulus data but an overall trend with position is observed. The average modulus value from nanoindentation for HPT processed Ta is 170 GPa, lower than the bulk value of 186 GPa.

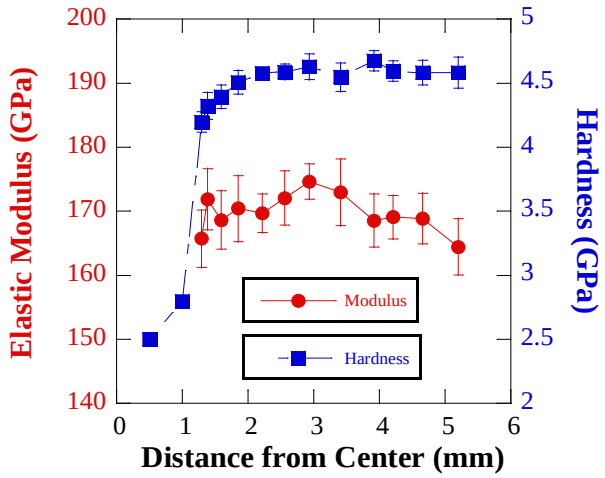

FIGURE 4.1: Nanoindentation hardness (blue) and elastic modulus (red) profiles of the HPT processed disk. The hardness values start low but increase up to a saturation value of ~4.5 GPa. Modulus values do not show any major trend, instead average at ~ 170 GPa, lower than the accepted modulus for Ta.

4.2.2 Strain Rate Sensitivity

FIGURE 4.2 shows a plot of ln(H) vs. ln($\dot{\varepsilon}$) for each location, here the slope of the line is the SRS. At the two closer radial positions, X = 1.0 and 3.0 mm, the SRS values are calculated as m = 0.027 and 0.0203 respectively. Both of these are lower than the value for coarse grain Ta, m = 0.060, measured by Wei and coworkers [66], but it is expected for BCC metals with smaller grain size. For X = 5.3 and 5.9 mm, where the grains should be in the NC regime, the SRS drops to m = 0.0092 and 0.0062 respectively. Using these values the activation volumes were calculated and are reported in TABLE 4.1. The values are reported using the convention of b^3, where b is the Burgers vector. For X = 1.0 and 3.0 mm values are $v^* = 6.22$ and $7.9b^3$ respectively. This is a difference of only $1.7b^3$ in the activation volume between the two locations. The positions

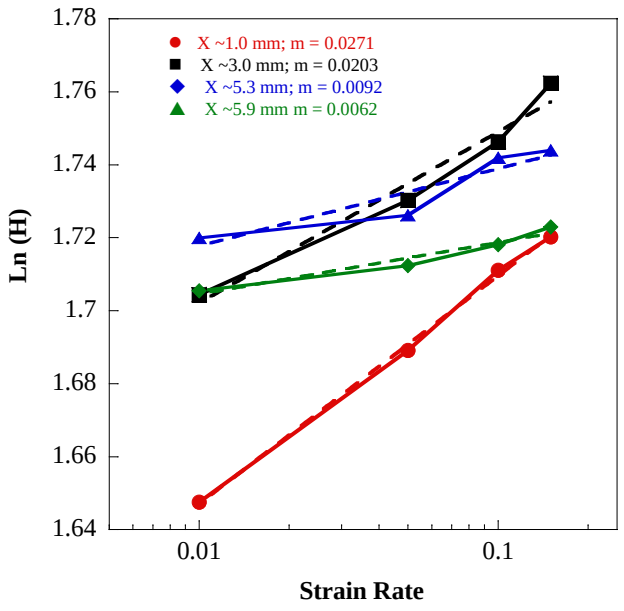

FIGURE 4.2: ln(H) vs. ln$(\dot{\varepsilon})$ plots for SRS measurements at positions X = 1.0, 3.0, 5.3, and 5.9 mm. The SRS values are calculated using equation 2.4 and are reported on the plot with the corresponding position. These values decrease with larger radial positions, starting at m = 0.02 and falling to m = 0.0062.

TABLE 4.1: Values for the SRS and activation volume for locations X = 1.0, 3.0, 5.3, and 5.9 mm. The SRS values decrease with increasing radial position, which corresponds to smaller grain sizes, and is expected for NC BCC metals.		
X (mm)	SRS	Act. Vol (b^3)
1.0	0.0271	6.22
3.0	0.203	7.931
5.3	0.0092	17.631
5.9	0.0062	26.613

X = 5.3 and 5.9 mm give much larger activation volumes $v^* =$ 17.6 and 26.6b^3.

4.3 Non-shearing Region: X < 5.3 mm

4.3.1 Microcompression

True stress vs. strain plots for pillars in the region $1.0 \leq X \leq 5.3$ mm are shown in FIGURE 4.3a. These plots show a consistent 0.2% offset yield strength of 1280 ± 95 MPa. This is three times that of coarse grain Ta and twice that of ECAP Ta measured previously [66]. These strengths are close to the expected yield strength when comparing to the hardness values in this region. FIGURE 4.3b and c shows SEM micrographs of a pillar tested in this region to ~8% and 16 % strain respectively. Even after compression to this level the pillar shows only homogeneous deformation. All other pillars in this region displayed this behavior; therefore, this region will be referred to as the non-shearing region. FIGURE 4.4a and b shows a BF with inset SAED pattern and dark field image respectively for non-shearing pillar that was fabricated at X = 5.3 mm. The grains in this pillar are elongated because the lamella was taken along the torsion direction of the disk and is therefore not a result of testing. The inset diffraction pattern in this image shows mainly continuous rings after testing, similar to the SAED pattern from the as processed material, FIGURE 3.3e. There is no noticeable difference when comparing the grains in

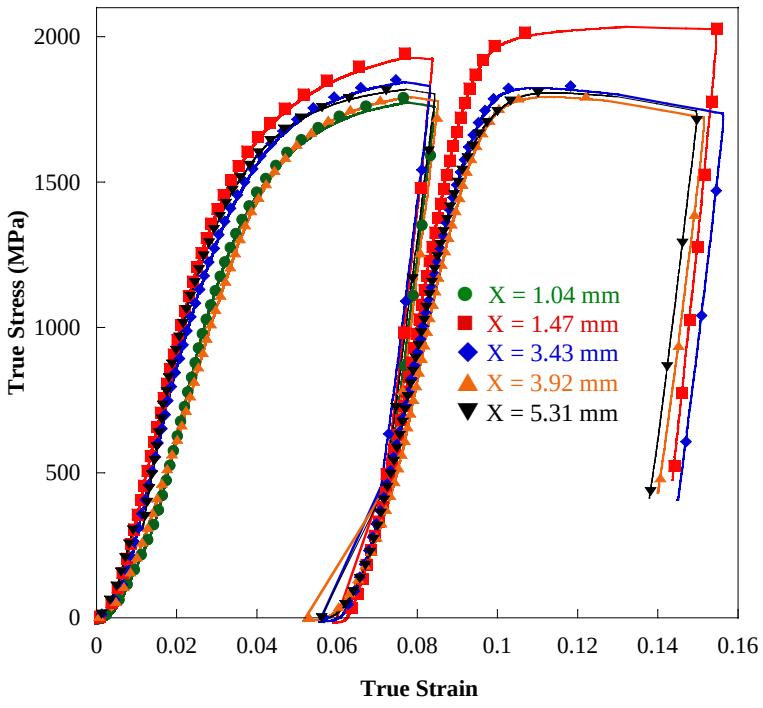

a)

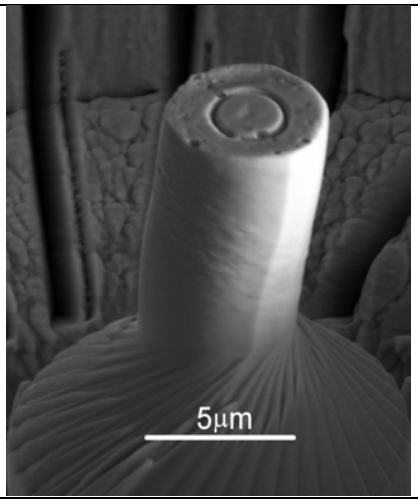

b)

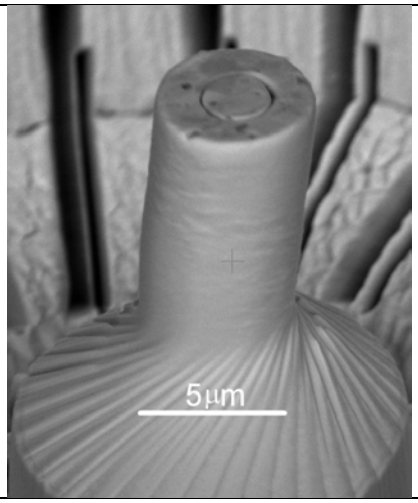

c)

FIGURE 4.3: (a)True stress vs. strain curves from pillars tested in the region $1.0 \leq X \leq 5.3$ mm. These curves show limited strain hardening and have a fairly consistent yield strength for all locations. (b,c) SEM micrographs of a single pillar in this region compressed to strain levels of ~8% and ~16% respectively. This pillar showed only homogeneous deformation, suggesting that classic dislocation motion is the main carrier of plastic deformation in this region.

FIGURE 4.4a and b to the as processed material in FIGURE 3.3e, f. This suggests that the plastic deformation in the non-shearing region is accommodated by classic dislocation motion.

4.3.3 Microtension

This section is concerned with the tensile behavior of specimens in the region on the disk of radial distance X < 5.3 mm. FIGURE 4.5a shows the true stress vs. strain curve for a specimen fabricated at X = 3.21 mm. The 0.2% yield strength for this test is 1340 MPa, a high tensile strength for Ta compared to its coarse grain behavior. However, this specimen only showed ~0.3% tensile elongation, which is low considering the extraordinarily ductile behavior of coarse grain Ta [141]. The elastic modulus for this test is 165 GPa, which like the nanoindenter data is lower than the bulk Ta modulus. The lack of plastic deformation is evident in FIGURE 4.5b, which shows an SEM image of the failed specimen. There is no evidence of a neck forming prior to fracture, suggesting a brittle failure for this specimen. An SEM image of this specimen at a higher magnification, FIGURE 4.5c, shows that the failure surface is straight, without any neck

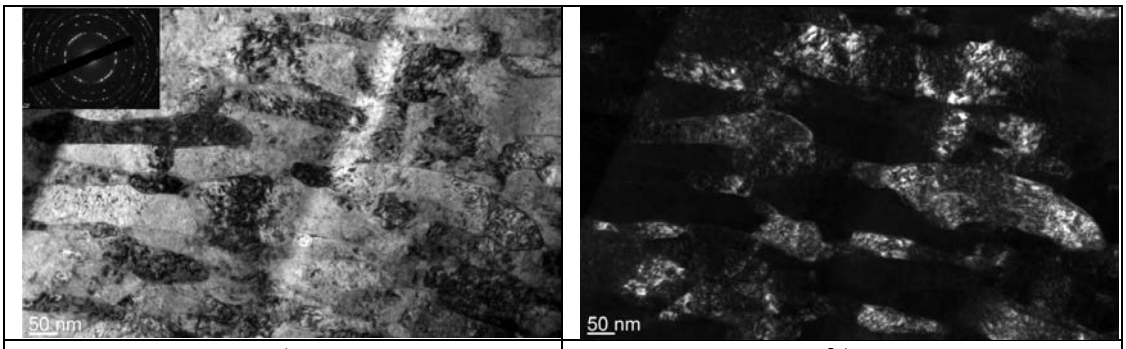

a) b)

FIGURE 4.4: (a) Bright field and (b) dark field TEM images of a homogeneously deforming pillar. These grains appear similar to the as processed material, suggesting that dislocation motion is still dominant. The elongated grains are due to the lamella being taken along the torsion direction of the disk.

formation and tension cracks have formed parallel to the fracture surface.

The true stress vs. strain curve for a specimen fabricated at X ~ 4.0 mm, FIGURE 4.6a, shows a different tensile response. This specimen yields at a lower stress, 1084 MPa, but displays a large increase in the ductility of up to 4.0% elongation. The relatively ductile behavior is evident by the slight neck forming between the markers on the failed specimen, shown by the SEM image in FIGURE 4.6b. However, this neck quickly becomes unstable and the specimen fractures in a manner similar to brittle failure. A higher magnification SEM image of the failed surface, FIGURE 4.6c, shows a straight and relatively flat surface, but the tensile cracks are no longer parallel to this surface. Instead they are curved, making an angle with respect to the loading direction of ~58° near the specimen edge that increases to ~70° near the middle.

SEM images of the fracture surfaces for the non-shearing specimens are shown in FIGURE 4.7a and b. While the stress vs. strain plot for the specimen at X = 3.2 mm suggested a brittle failure, the fracture surface in FIGURE 4.7a shows evidence that plasticity occurred in local regions. This microplasticity is also observed for the specimen fabricated at X = 4.0 mm, FIGURE 4.7b, which is not surprising since it displayed ~4.0% total elongation. These images suggest that dislocation motion may still be active during plastic deformation of specimens in this region.

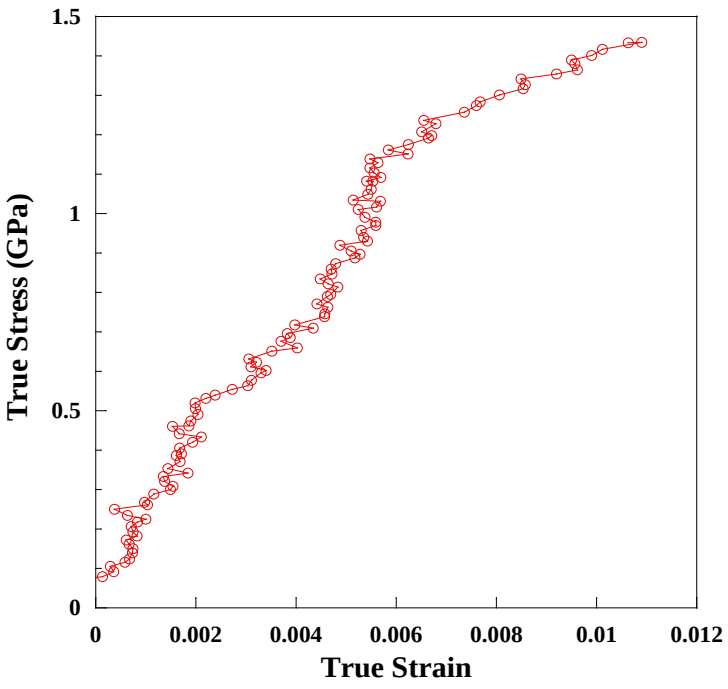

a)

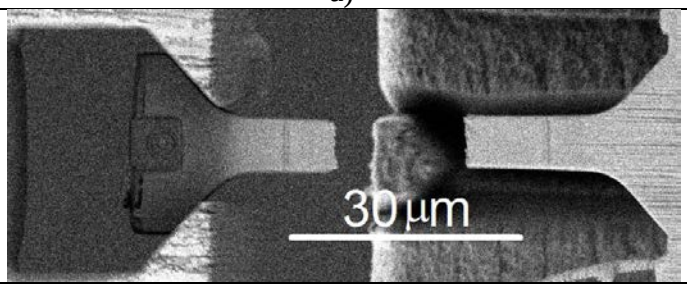

b)

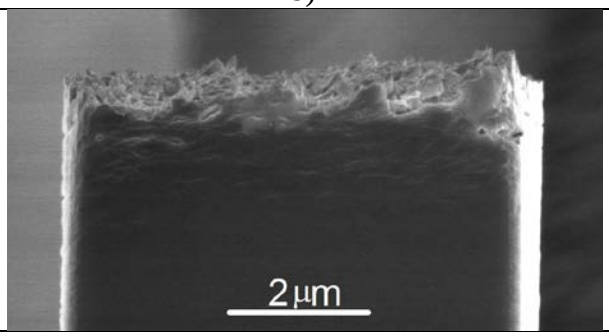

c)

FIGURE 4.5: (a) True stress vs. strain curve for an HPT Ta tensile specimen fabricated at X = 3.2 mm. The elastic modulus is greatly reduced but the strength has increased compared to coarse grain Ta. (b) SEM image of the failed specimen following fracture showing a brittle type failure in the gauge section. (c) A higher magnification SEM image of the failed specimen edge, showing a straight edge and tensile cracks that are perpendicular to the loading direction.

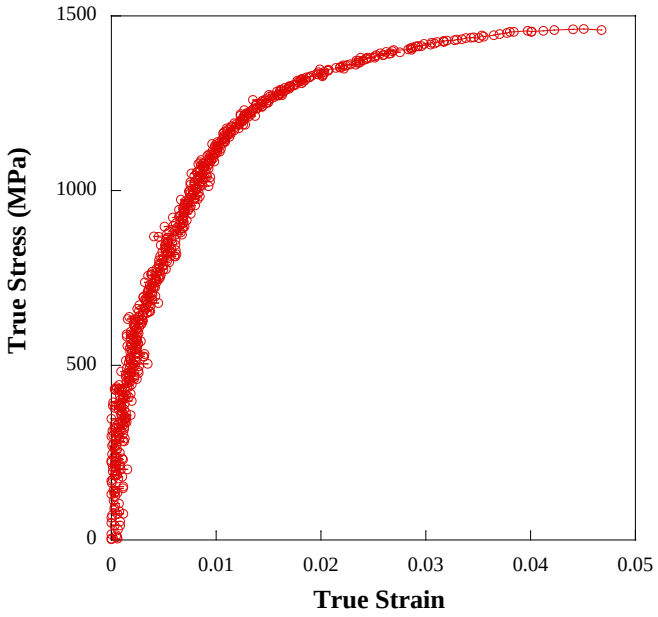

a)

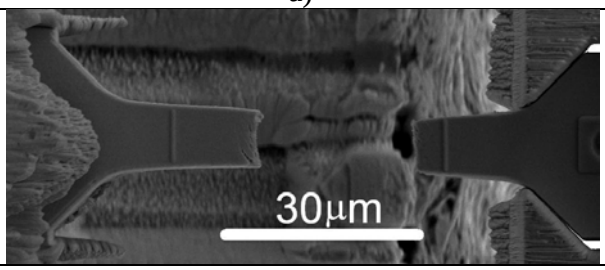

b)

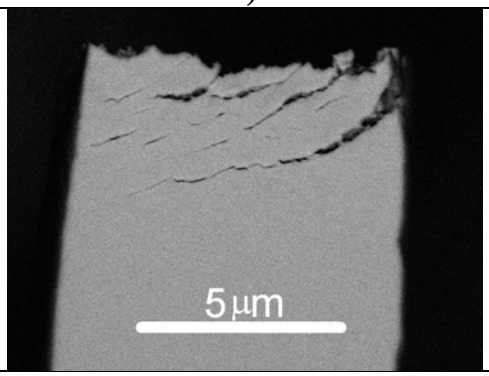

c)

FIGURE 4.6: (a) True stress vs. strain curve for an HPT Ta tensile specimen fabricated at X = 3.9 mm. There is substantial ductility in this specimen. (b) SEM image of the failed specimen following fracture showing a slight neck forming in the gauge section. (c) A higher magnification SEM image of the failed specimen edge, showing a straight edge but tensile cracks that are forming off at an angle with respect the loading direction.

4.3.4 Tension-Compression Asymmetry

Since both compression and tension tests were completed in this work it is possible to investigate the presence of an asymmetry between the yield strengths. FIGURE 4.8 shows tension and compression curves for the region X = 3.2 – 3.4 mm (red) and X = 4.0 mm (black). There is a qualitative difference between the curves, but this could be due to the difference in the elastic portions. For X = 3.2 – 3.4 mm the 0.2% yield strengths in tension and compression are 1340 and 1283 MPa respectively. Only a 4.2% difference is calculated here, which could be attributed to deciding on the elastic regime to use for yield strength measurement on the compression curves as in the compressive curves, a significant contribution to the strain comes from the machine compliance. Therefore we believe that no considerable tension-compression asymmetry, as a result of a material response, is present in this region. However, specimens fabricated at X = 4.0 mm do display an asymmetry, where the tensile yield strength is 1084 MPa and the compressive yield strength is 1446 MPa, a 25% increase for compression.

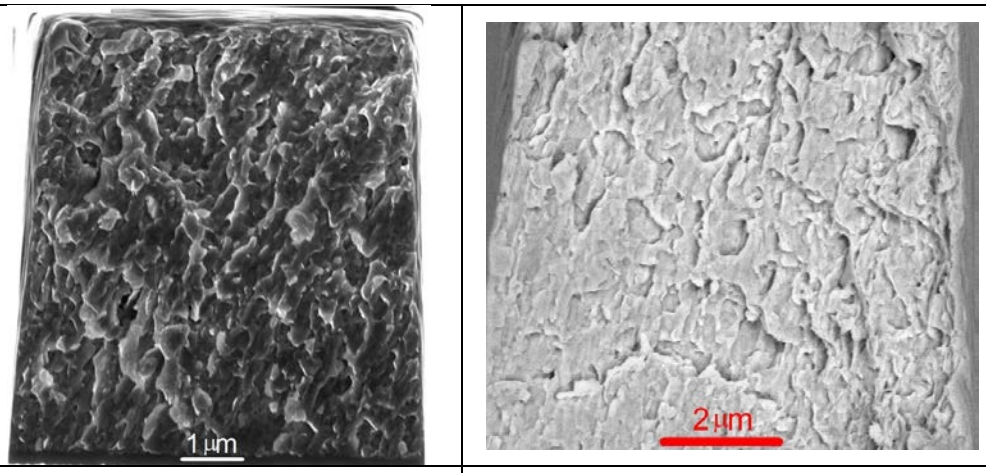

a) b)

FIGURE 4.7: High resolution SEM images of the fracture surfaces for the non-shearing specimens at (a) X = 3.4 and (b) X = 4.0 mm. These images show evidence of small pockets of plastic deformation despite the brittle type failure observed during testing.

4.4 Shearing Region: X > 5.3 mm

4.4.1 Microcompression

Pillars tested in the region X > 5.3 mm show a drastic change in their mechanical behavior. FIGURE 4.9 shows the plots of true stress vs. strain plots for pillars in this region. The 0.02% yield strength in this region shows more variability, 1385 ± 143 MPa, when compared to the non-shearing region. The SEM images of pillars in this region, FIGURE 4.10a – d, shows the deformation behavior has transitioned to localized

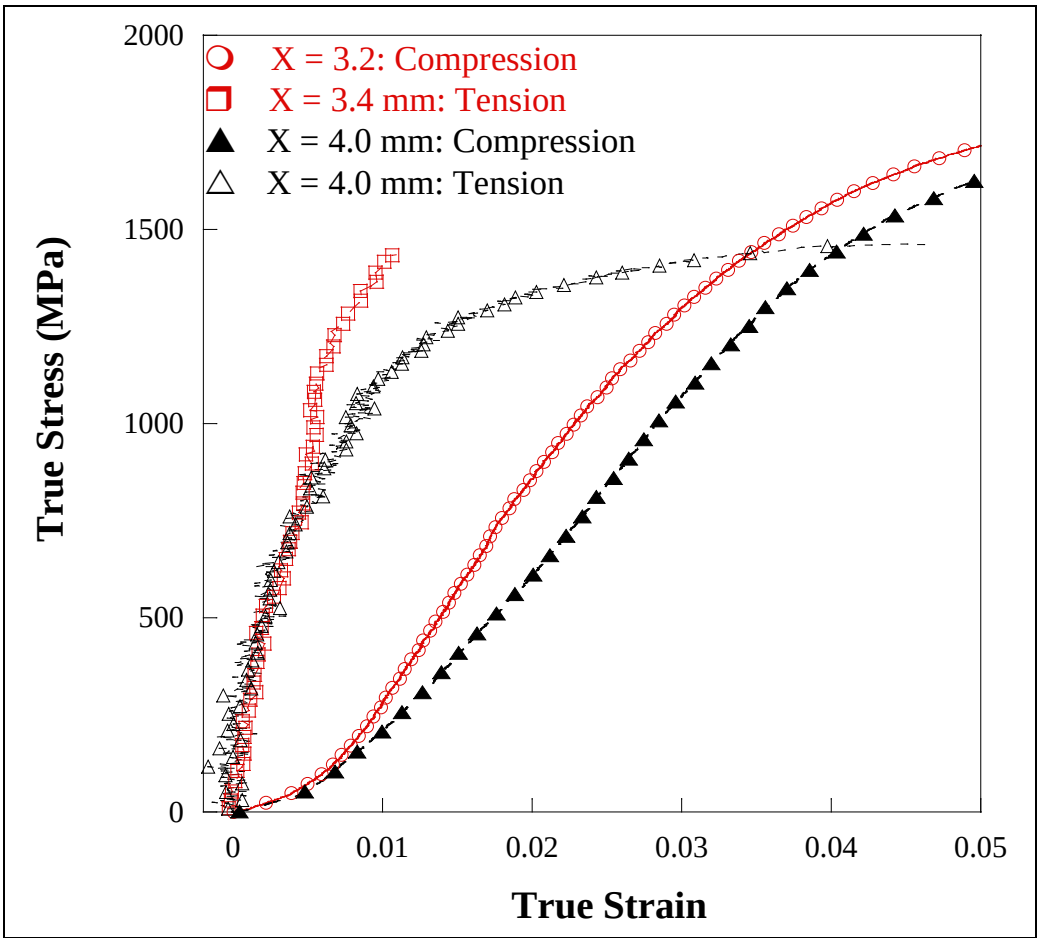

FIGURE 4.8: Comparison of tension and compression true stress vs. strain curves for specimens fabricated in the region X = 3.2 – 3.4 mm(red) and X = 4.0 mm (black). The yield strengths for X = 3.2 – 3.4 mm show no asymmetry, suggesting that dislocation motion is still the active deformation mechanism.

plasticity. FIGURE 4.10a initially showed a single shear band after being compressed to 8% strain but after being reloaded multiple shear bands formed. When a separate pillar was compressed to an initial strain of ~12% it failed instead of forming multiple bands, FIGURE 4.10b. From these failed pillars it is possible to measure the shear band angle by tilting the SEM stage until the beam direction is parallel to the failure surface. The specimens measured all gave a shear band angle of 44-46°. FIGURE 4.10c shows a shear band that initiates at the contact region between the tip and the pillar. A pillar with a

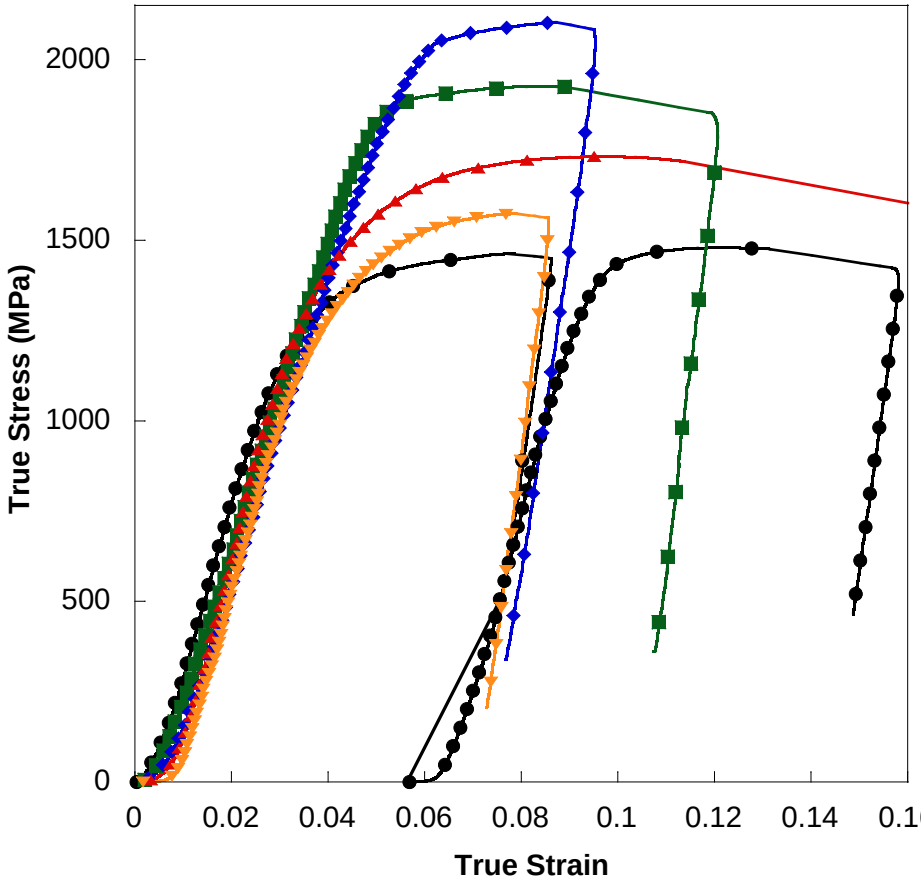

FIGURE 4.9: True Stress vs. true strain curves for pillars tested in the region X > 5.3 mm, where the yield strength is 1385 ± 143 MPa.

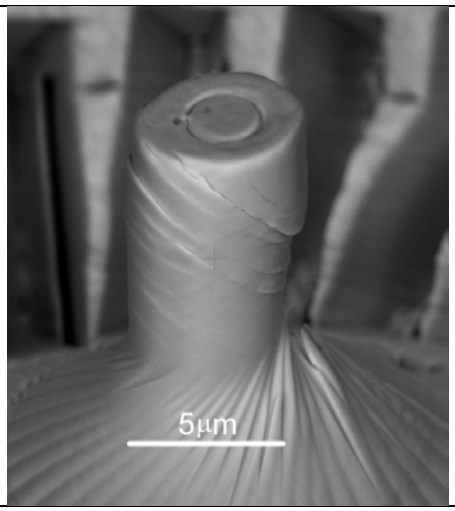

a)

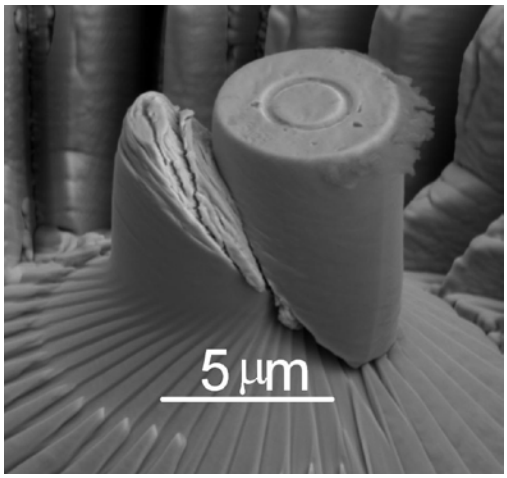

b)

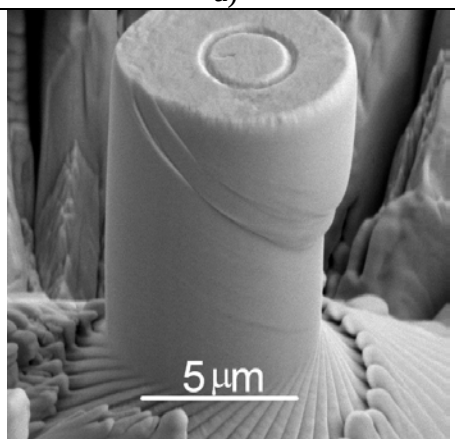

c)

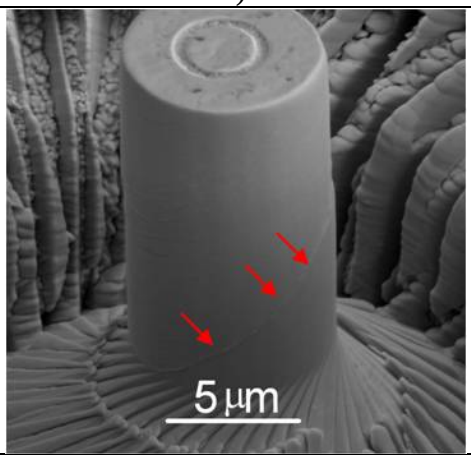

d)

FIGURE 4.10: SEM micrographs of microcompression pillars that display shear band formation. (a) A pillar showing multiple shear bands after two successive compression tests, black curve in figure 4.6. (b) A pillar showing failure via a shear band when the initial strain level is set to ~12%, red curve in figure 4.6. (c) Pillars showing the effects from tip-pillar contact on the shear band propagation. (d) Pillar with a 7.0 μm diameter that still displays shear band formation.

larger diameter, FIGURE 4.10d, still shows formation of shear bands, indicated by the red arrows, showing this behavior is not a size dependent effect.

Also, there is no evidence in either the load-displacement or stress-strain curves of when the shear band forms, unlike compression tests on metallic glass specimens which show a definitive “pop-in” event corresponding to shear band formation [110]. This suggests that the deformation occurring in NC Ta develops over time instead of a

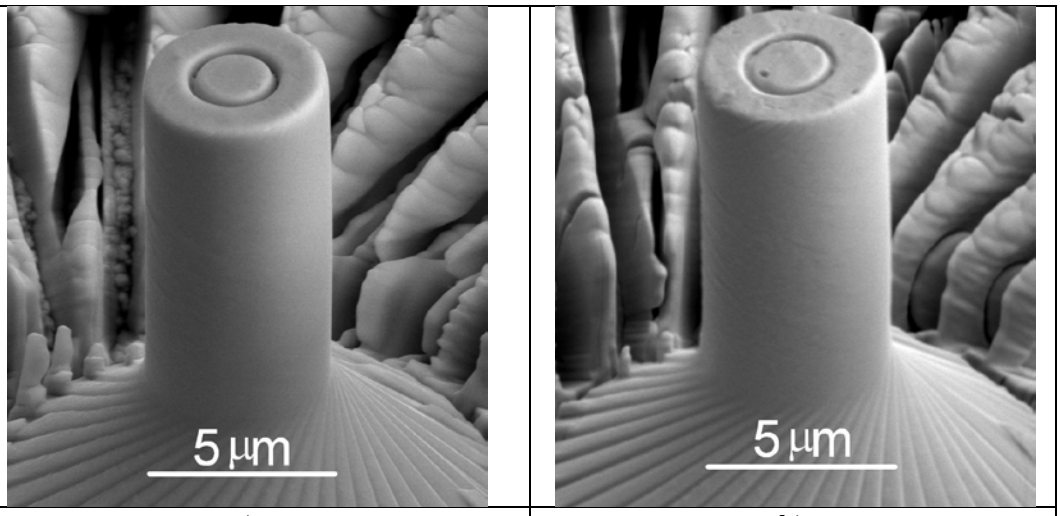

a) b)

FIGURE 4.11: SEM micrographs of pillars fabricated in the shearing region but strain levels of (a) 5.5% and (b) 6.5 %. Diffuse bands are seen at the edges of each pillar, indicating that these bands form over time instead of the rapidly forming bands observed in microcompression studies on bulk metallic glasses. [110].

single abrupt event. To investigate this, pillars compressed to strain levels of 5.5% and 6.5% are shown in FIGURE 4.11a and b respectively. Both of these pillars show only diffuse bands at the pillar edge, confirming the notion that the shear bands develop over time.

For all the tested pillars shown, the direction in which the shear band propagates always follows the radial direction of the disk. As previously shown in FIGURE 3.4a, the grains in this orientation are equiaxed, suggesting that this reduced dimension affects the shear band formation. However, all pillars presented so far were fabricated within a 1.0 mm radius of each other. To exclude any effects from the tip geometry, pillars were also fabricated at positions on the disk 90° from these original pillars. These pillars, not shown here, also deform via shear bands that form along the disk's radial direction.

The microstructure of a sheared pillar shows a different response to loading. FIGURE 4.12 shows a combination of BF TEM images containing the shear band and the

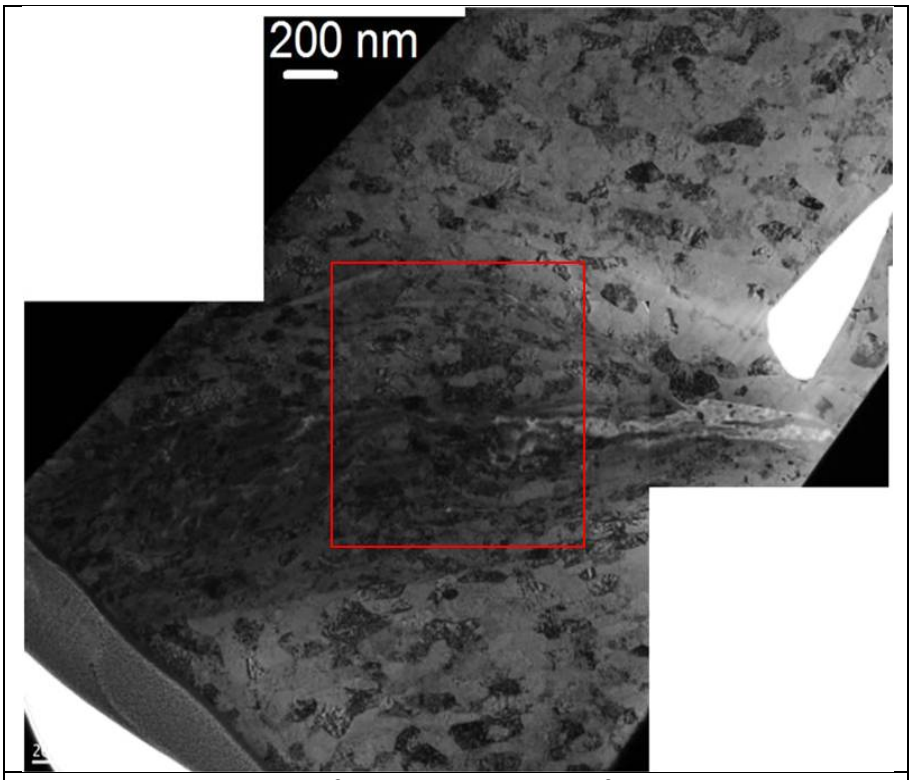

FIGURE 4.12: Bright field TEM image of a microcompression specimen that forms a shear band. Outside of the band the grains appear equiaxed, while inside the shear band the grains are elongated and show evidence of grain rotation. The region outlined in red represents the shear band region that will be analyzed with orientation mapping.

un-sheared portions of this pillar. Indicated by the red box, the shear band region is ~1.0 μm wide and contains thin, elongated grains. This is in contrast to the equiaxed grain structure in the un-sheared portion, upper right of FIGURE 4.12. The lamella for these images was taken along the disk's radial direction which explains the equiaxed structure, showing that the structure inside the shear band is solely a result of the plastic deformation during mechanical testing.

Using the Nanomegas ASTAR system at Drexel University the individual grain orientations in this lamella were indexed. FIGURE 4.13a and b shows an inverse pole figure (IPF) orientation map and corresponding IPF key of, approximately, the region in

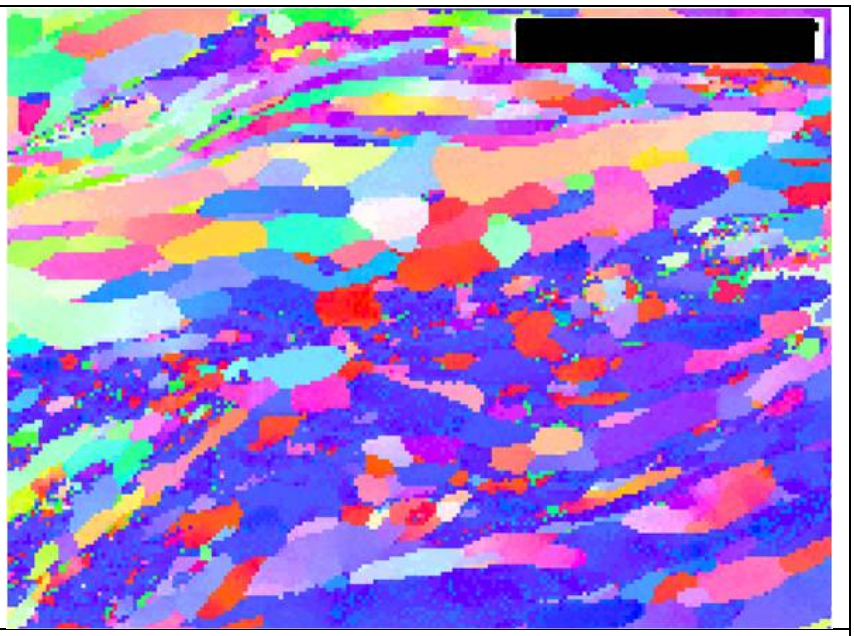

a)

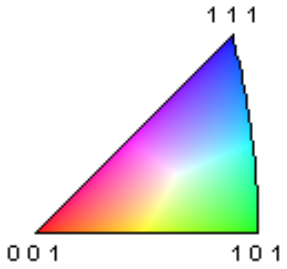

b)

FIGURE 4.13: (a) Orientation and (b) IPF color map of the region corresponding to the red square in figure 4.10. This shows that individual grains exist inside of the band after forming and there appears to be a texture existing inside of the band.

FIGURE 4.12 outlined by the red square. The existence of different orientations in this image shows that the NC Ta processed by HPT does in fact contain individual grains. Also, it reinforces the observation from the BF image that the grains in the shear band are elongated along the shearing direction. This orientation map shows evidence of a texture forming inside of the shear band. Grain boundary misorientation map and key in FIGURE 4.14a and b respectively show that mostly high angle grain boundaries exist both inside and outside of the band. Also evident in this map is the curvature displayed

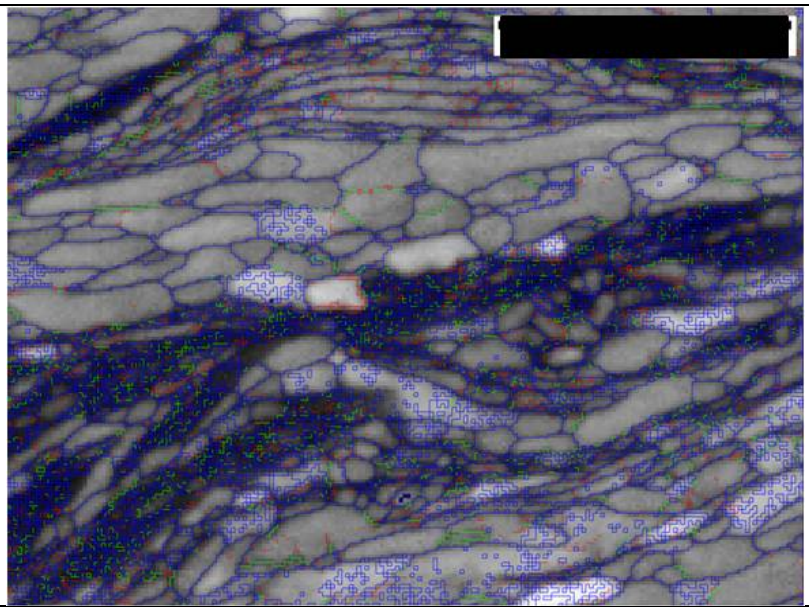

a)

Boundaries: Rotation Angle

	Min	Max	Fraction	Number
	2°	5°	0.102	2601
	5°	15°	0.089	2279
	15°	180°	0.809	20644

b)

FIGURE 4.14: Grain boundary misorientation map of the same region as figure 4.11. Here the blue lines represent high angle grain boundaries (ie. misorientations >15°) which account for ~80% of the total fraction of boundaries. Also evident in this map is the degree of curvature that exists inside the band, suggesting the grains undergo a form of cooperative grain boundary rotation.

by the grains in the shear band, which suggests that grain rotation has occurred in this band. FIGURE 4.15a – f shows BF TEM images, orientation maps, and grain boundary orientation maps for locations outside the band, at a band interface, and inside the band. The IPF key in FIGURE 4.13b is used for the orientation maps in FIGURE 4.15 as well. Outside of the band, the grains are equiaxed with diameters in the NC regime. At the band interface there is a clear distinction between the sheared and non-sheared grains.

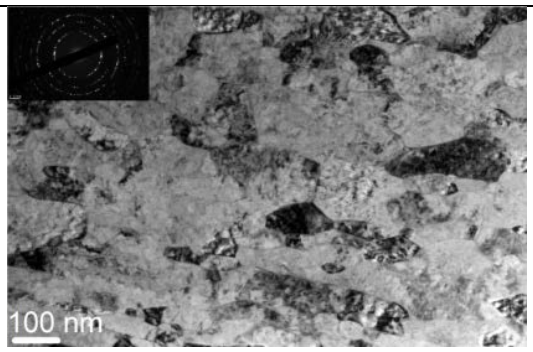

a)

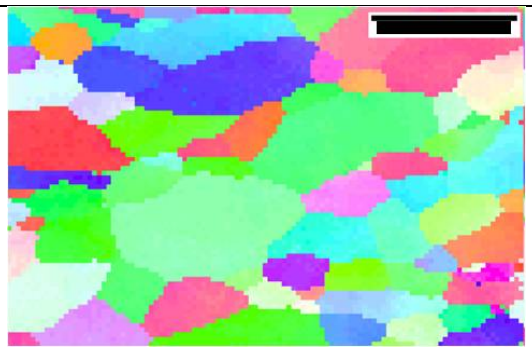

b)

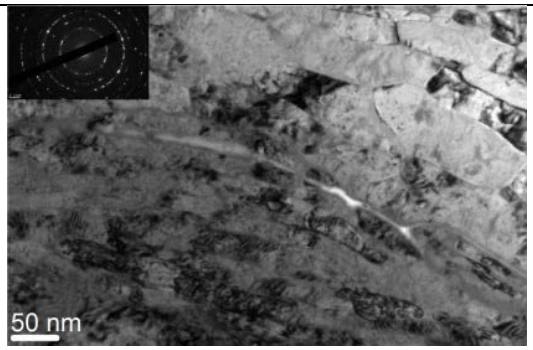

c)

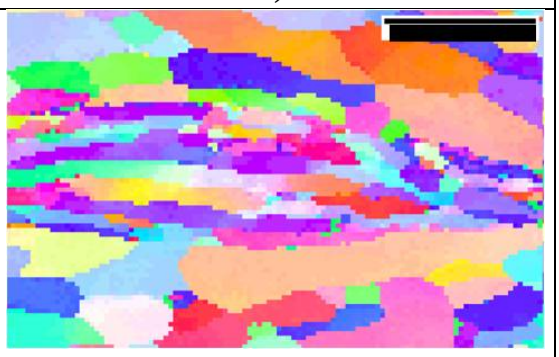

d)

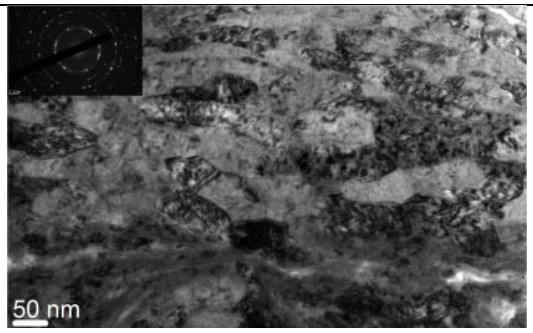

e)

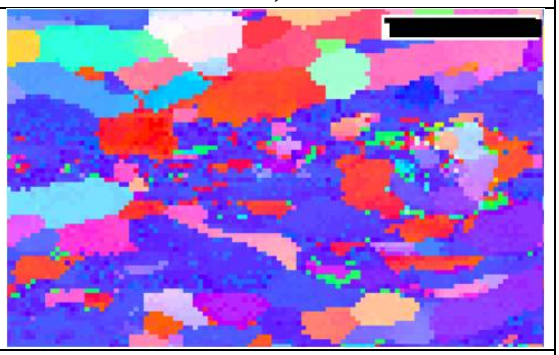

f)

FIGURE 4.15: Bright field TEM images with inset SAED patterns and orientation mapping images from (a-b) outside the shear band, (c-d) at the band interface, and (e-f) inside the shear band. Grains outside of the band show an equiaxed structure similar to the as-processed material, while at the interface there is a change to thinner, more elongated grains. Inside the band the orientation image shows the presence of a texture following the band formation, the IPF map in figure 4.11b is used to index the orientation maps here as well.

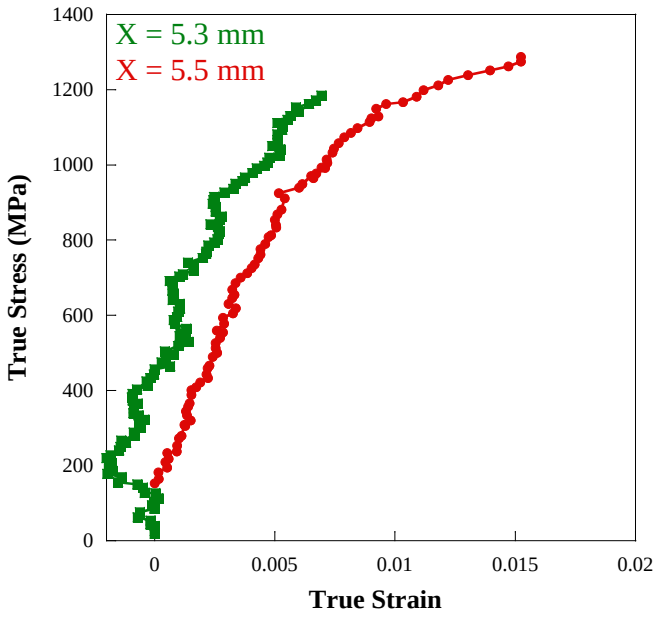

a)

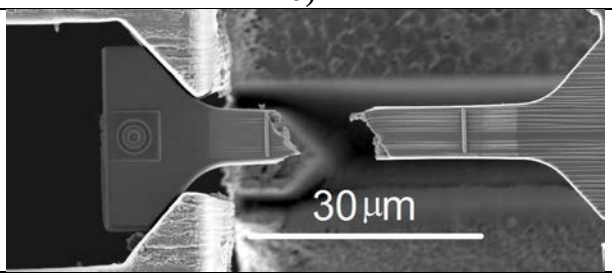

b)

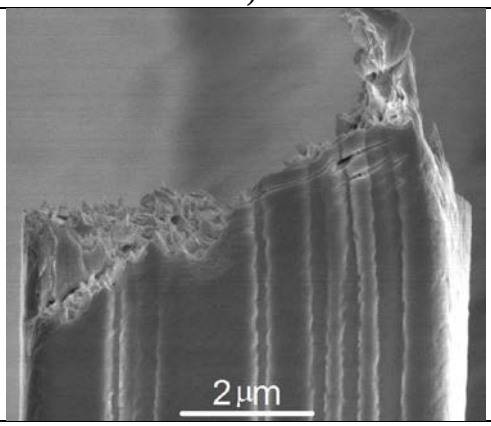

c)

FIGURE 4.16: (a) True stress vs. strain curves for HPT Ta tensile specimens fabricated at positions X = 5.3, and 5.5 mm. Both curves have similar elastic portions that give modulus values lower than the accepted value. (b) SEM image of the failed specimen following fracture showing a transition to shearing type failure in the gauge section. (c) A higher magnification SEM image of the failed specimen edge, showing an angle edge with tensile cracks that are parallel with the surface.

4.4.2 Microtension

FIGURE 4.16a shows true stress vs. strain plots for specimens tested in this region, specifically at locations X = 5.3 and 5.5 mm. Here the 0.02% yield strengths are 1180 and 1150 MPa respectively. These specimens also showed low ductility, only ~0.7% tensile elongation. Also, the elastic modulus has dropped to ~143 GPa, a reduction between regions making the difference from the accepted modulus even greater. FIGURE 4.16b shows an SEM image of a failed specimen in this region, where it can be seen that NC Ta also transitions to failure by shear in tension. At higher magnification, FIGURE 4.16c shows that the shear band angle is measured as ~54° with respect to the tensile loading direction, an increase from the expected plane of maximum shear stress. Tensile cracks in this specimen also follow the same direction as the shear band, indicating that the deformation outside of the main band is still in shear.

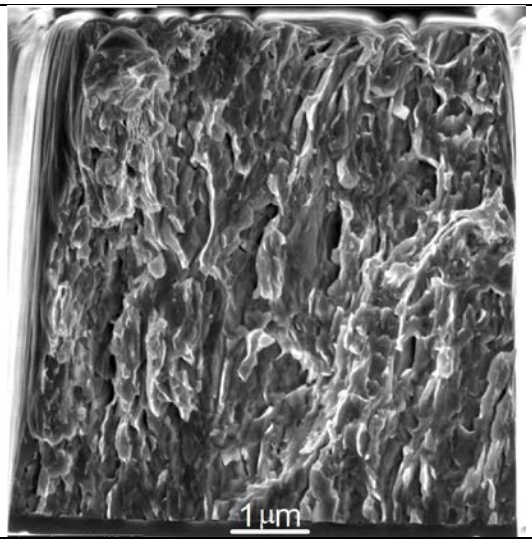

FIGURE 4.17: SEM image of the fracture surface of the shearing specimen which shows directionality along the vertical image direction.

The fracture surface for the shearing specimen, FIGURE 4.17, shows a different structure when compared to the previous specimens. Here the features again show evidence of plasticity, despite the low elongation to failure, and directionality along the vertical direction of the image. This direction corresponds to the specimen gauge thickness and thus the elongated grain direction. However, the deformation appears to occur along the horizontal direction, which would be the minimum grain direction. This suggests that, like the compressive behavior, the deformation in tension also occurs along the minimum grain diameter.

4.4.3 Tension-Compression Asymmetry

The previous non-shearing tensile specimen (X = 4.0 mm) began to display a strength asymmetry. This behavior carries into the shearing region. FIGURE 4.18, shows the tension (green) and compression (blue) curves for specimens at $X \geq 5.3$ mm. Tensile yield strength in this region is 1170 ± 21 MPa and in compression is 1385 ± 143 MPa. The yield strength in compression is 15% higher in this region. Although the asymmetry in this region is smaller than that of specimens at X = 4.0 mm, it seems there is not only a transition to localized deformation at the disk edge but also a trend of increasing tension-compression asymmetry with position.

4.5 Summary and Conclusions

Micromechanical testing techniques were used to determine how the mechanical properties of HPT processed Ta change with grain size. The nanoindentation hardness profile of the disk shows a trend of increasing hardness with position, up to a saturation value of ~4.6 GPa past X = 1.0 mm [154]. Elastic modulus measurements have some scatter in the data but the average value is ~170 GPa, lower than accepted value for bulk,

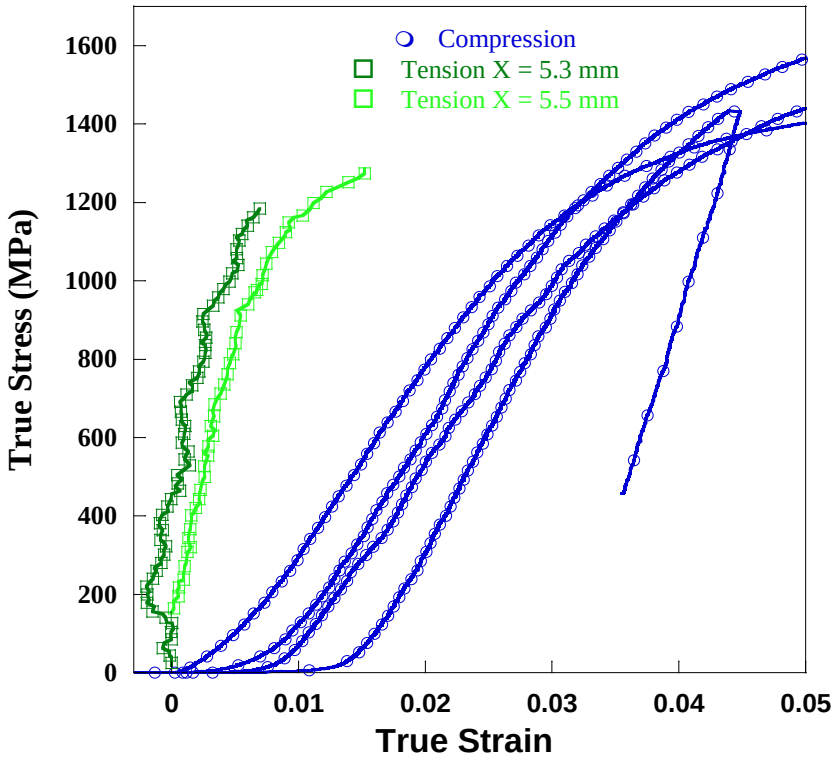

FIGURE 4.18: Comparison of tension and compression true stress vs. strain curves for specimens fabricated in the region X ≥ 5.3 mm. The compressive strength is ~15% higher, which combined with the increase in shear band angle in tension suggests a pressure dependence on the yield strength.

texture free polycrystalline Ta. Strain rate sensitivity values show a decrease with increasing radial distance. From these values the activation volumes associated with plastic deformation of HPT Ta are still on the order expected for dislocation motion.

In the region of the disk 1.0 ≤ X ≤ 5.3 mm microcompression tests show only homogeneous deformation and 0.2% yield strength of 1280 ± 95 MPa. Tensile specimens in the same region showed evidence for a brittle type failure, with strengths of 1340 MPa (X = 3.2 mm) and 1084 MPa (X = 3.9 mm) and elongations that varied from 0.3 – 4%. The 4.0% tensile elongation and slight neck formation for the specimen at X = 3.9 mm is impressive since no processing was done to improve the ductility. SEM images of fracture surfaces at all locations show evidence of localized plasticity. For X > 5.3 mm

the specimens in both tension and compression showed a transition to localized plastic deformation in the form of shear bands. The shear band angle in compression is 44 – 46° and the 0.2% yield strength in this region is 1385 ± 143 MPa. Tensile specimens in this region formed shear bands at 54° with respect to the loading direction and show yield strengths of 1170 ± 21 MPa. At positions, X > 4.0 mm, the compressive strengths are 15 – 23% higher, indicating an increased presence of a tension-compression asymmetry, which is consistent with earlier work on an NC Fe-alloy by Carsley et al [73].

CHAPTER 5: DISCUSSION

5.1 Introduction

In the previous chapter the results for the micromechanical testing of NC Ta were presented. Both the hardness and strain rate sensitivity values showed a dependence on position away from the disk center. The microcompression and microtension tests also reveal a position dependence on the deformation mode and tension-compression asymmetry. At the disk edge the deformation transitions from homogeneous to localized deformation and the compressive yield strength increases compared to the tensile strength. In the following sections the explanations for the observed mechanical properties like the hardness/SRS trends, reduced modulus, and microplasticity will be discussed. Also, reasons for the transition in deformation mode and increased tension-compression asymmetry will be determined.

5.2 Mechanical Properties

Values for hardness measured here are similar to previously reported values for tantalum processed by HPT under the same conditions [65]. The saturation in hardness has been reported by others and is most likely due to saturation in the grain refinement [154, 155]. The formation of new, small grains during HPT involves the reduction of dislocation cell size, and since there is an inverse relationship between the cell size in a material and the applied shear stress, the processing parameters must affect the minimum achievable grain size. Using the Tabor relationship [156], $\sigma_y = H/3$, the yield strength for

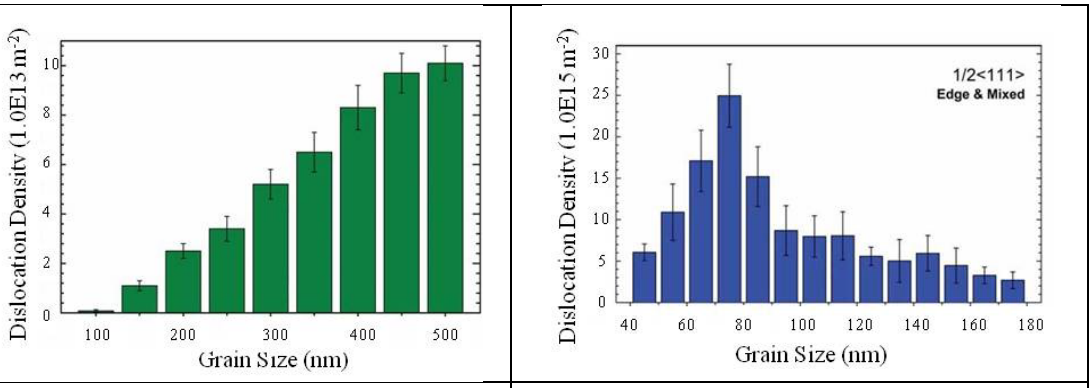

a) b)

FIGURE 5.1: Effects of grain size on the density of (a) screw and (b) edge/mixed type dislocations in HPT processed Mo. Below a grain size of 100 nm the density of screw type dislocations decreases while for edge type it increases. This combination can explain the continuing reduced strain rate sensitivity observed for grain sizes in the NC regime [157].

the HPT Ta should be near 1.5 GPa, which is on the order of the strengths recorded in both tension and compression.

SRS measurements also show a decreasing trend with increasing radial distance, which is expected for BCC metals as the grain size gets smaller at the edge. The smaller SRS results in an increase in the activation volume, to $v^* \sim 26\ b^3$ at the disk edge. Since the activation volume is characteristic of the atomic process occurring during deformation, this can help identify possible deformation mechanisms. Such a large value near the disk edge indicates that mechanisms like diffusion or coble creep, $\sim b^3$, are unlikely. Instead, a high activation volume suggests that the material will still be able to sustain plastic deformation through dislocation motion. As was mentioned previously, it was proposed that the cause for the decreasing SRS is the increase in flow stress due to grain boundary strengthening [11], assuming that propagation of screw dislocations via the kink-pair mechanism is still the rate-limiting process. However, recent reports investigating the density of edge and screw dislocations in HPT Mo have measured a decreasing density of screws, FIGURE 5.1a, and an increase in the density of edges for

grain sizes below 100 nm, FIGURE 5.1b [157]. Since edges move much faster than screws through a BCC lattice, this change will influence the material's SRS. Along with dislocation density measurements, Cheng, et al., also proposed that the reduced SRS values can be explained through the increased dependence on the motion of edge dislocations [157]. The shear strain rate and SRS of a material can be calculated using equation 5.1 and equation 5.2 respectively, which can be separated into edge (*e*) and screw (*s*) components [157]. Here v is the dislocation velocity and ρ is the dislocation density. An increased density of edge dislocations combined with the slow velocity and decreasing density of screw dislocations results in a decreasing SRS. This explains the reduced SRS values measured at the edge of the HPT Ta disk.

$$\dot{\gamma} = bv\rho \qquad \text{equation 5.1}$$

$$m_{s,e} = \frac{\partial \ln \tau}{\partial \ln \dot{\gamma}} = \frac{\partial \ln \tau}{\partial (vb\rho)} = \frac{\partial \ln \tau}{\partial \ln (bv_e \rho_e)} + \frac{\partial \ln \tau}{\partial \ln (bv_s \rho_s)} \qquad \text{equation 5.2}$$

The elastic modulus measured by nanoindentation (170 GPa) and microtension (145 – 165 GPa) are also reduced compared to the accepted value for coarse grain polycrystalline Ta (186 GPa). This has been observed in previous reports for nanocrystalline metals and there are multiple proposed reasons for the reduced modulus. One of the proposed reasons is the high porosity that exists after processing, specifically for bottom-up techniques [158]. However, top-down techniques, like HPT, produce samples with near bulk density, making it unlikely that porosity is causing the lower modulus. A second reason is the increase in the volume fraction of grain boundaries and triple junctions at the small grain size, which can reach near 20% for grain sizes 20 – 30 nm [159]. Their lower modulus values than the crystalline material will have more of an effect as the volume fraction increases. Setman and coworkers also reported on the

presence of a high concentration of vacancies, ~10^{-4}, in metals following HPT processing [160]. This concentration is near the value seen for thermally generated vacancies in metals near their melting point. Such a high number density of vacancies could cause a drop in the elastic modulus [65]. The large variation in the experimental values for NC Ta measured in this work suggests that a third method of determining modulus should be used to confirm the existence of a reduced modulus and to see if any meaningful comparison exists to either the tension or nanoindentation values. This third method, diamond anvil cell (DAC) testing, is presented in Appendix A. Although this method only produced one successful test, on a specimen taken near the disk center, the elastic modulus is also measured to be 165 GPa, confirming the reduced modulus for NC Ta processed by HPT. Determining why the reduced modulus exists presents some difficulties. Effects from porosity can be ignored since SPD processing methods produce bulk density samples. This leaves contributions from increased GB/TJ volume fraction and vacancy concentration. TEM images of the HPT Ta show that the grains are elongated, where the maximum diameter is in the UFG regime and the minimum is NC. This means that the GB volume fraction will depend on which grain orientation is used for calculation, making the influence on elastic modulus unclear. The reports on vacancy concentration showed a trend similar to the hardness, the concentration increases up to some saturation value past a position X. Since the GB volume fraction is still small, it is possible that the high vacancy concentration causes the observed reduction in modulus in the region $X < 5.3$ mm. The smaller elongated direction in the shear region means an increase in the GB volume fraction, which can cause an even further reduction in modulus. Separating the effects from GB/TJ volume fraction along with values for the

vacancy concentration these contributions will require simulations to effectively control and quantify both effects. The vacancy concentration can be obtained from the HPT disk, but an effective concentration measurement using a technique like differential scanning calorimetry (DSC) requires annealing out defects, including dislocations, which could affect the mechanical properties. Since only one HPT processed disk was available these measurements were not made in this work.

Tensile specimens show an increase in strength over coarse grain Ta and a tensile elongation that varies from 0.3 – 4.0%. The two specimens that showed non-shearing behavior display different amounts of tensile ductility. At X = 3.2 mm there was less than 1.0% elongation, but at X = 4.0 mm it increased to ~4.0%. However, the SEM images of the fracture surfaces for these specimens both showed a possibility for microplasticity, even though the stress-strain curves show limited ductility and brittle type failure. An explanation for this behavior is the quantized crystal plasticity (QCP) model proposed by Li et al. [161, 162]. In this work QCP represents localized slip events in grains, resulting in increased plastic strain in these grains. Their model accurately matches the experimental behavior of NC Ni for grain sizes 300, 150, and 50 nm, but only if an asymmetric distribution of critical shear stress values within the grain ensemble is used. Essentially, with respect to the loading direction, there are “hard” and “soft” oriented grains inside the volume allowing only certain grains to undergo slip. Plastic strain will advance in the “soft” grains when a critical shear stress is reached for the specific orientation [163]. This QCP explains the evidence of plastic deformation observed in the fracture surfaces but the rather low amount of global plastic deformation.

5.3 Deformation Transition

The microcompression and microtension tests revealed that the deformation behavior of NC Ta changes from homogeneous to localized plastic deformation. The disk location for the transition to shear bands in tension is the same as in compression, suggesting that the deformation mechanism is the same under both conditions. An obvious question then is what causes this transition to occur? An initial concern is the possible damage the pillar withstands during FIB milling. As was previously discussed, a Ga^+ ion incident on a surface can be implanted some range (R) into the target and reports from Bei and coworkers showed that pillars fabricated without FIB failed near the theoretical strength [108]. However, a later report by the same group using the same type of pillar fabrication, but now with 11% pre-strain before testing, found that the strength was much lower [164]. The main difference between their two reports is that the first report used pillars that were essentially dislocation free, while the pillars in the second report were not. This shows that if the initial material contains dislocations then any extra defects that are added to the pillars due to FIB milling do not have a large impact on the strength. The initial material here is severely plastically deformed, so there is a high dislocation density to start with and thus FIB milling should have little effect on the strength.

Also, compared to the overall pillar size, the damage layer does not make up a large volume fraction. FIGURE 5.2a and b shows the results of TRIM calculations for 30 kV Ga^+ ions incident on a Ta target at normal and grazing incidence respectively [82].

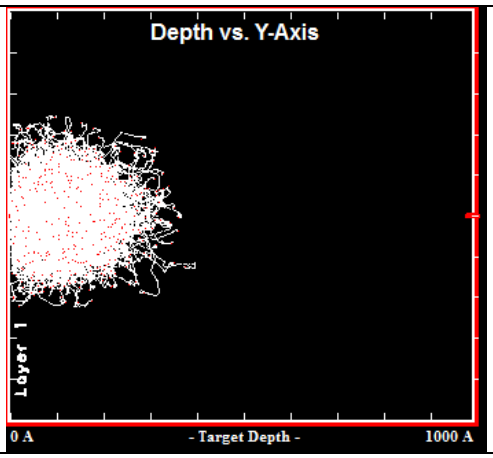

a) b)

FIGURE 5.2: TRIM simulations for a 30 kV Ga^+ ion incident on a Ta surface at (a) normal and (b) grazing incidence [82]. For either instance the penetration depth does not exceed 30 nm, meaning a 5.0 μm diameter pillar will have a small volume considered damaged by the FIB milling.

These two orientations span the region of maximum (normal) to minimum (grazing) implantation depths. At normal incidence, the maximum penetration depth is ~ 30 nm, while at grazing angles this depth is only 20 nm. Assuming a pillar with the following dimensions, 5.0 μm in diameter, 10 μm tall and a grain size of 40 nm, there will be ~2.0 million grains in the entire volume. Using the damage layer at normal incidence, only 1.2% of the total volume may have FIB damage; such a small portion will have a negligible influence on the overall mechanical behavior of the specimens.

Another possibility for the transition to shear bands is that during the HPT process a deformation texture develops that either suppresses the bands in $1.0 \leq X \leq 5.3$ mm or enhances this behavior when $X > 5.3$ mm. There are reports of texture having an effect on the formation of shear bands. For example, Kuroda and Tvergaard showed, using crystal plasticity simulations, that a cube texture ({100}<001>) in a rolled FCC metal will suppress the formation of shear bands in compression and tension [166]. The ideal (110) pole figures for a BCC metal tested in torsion were calculated by Baczynski and Jonas

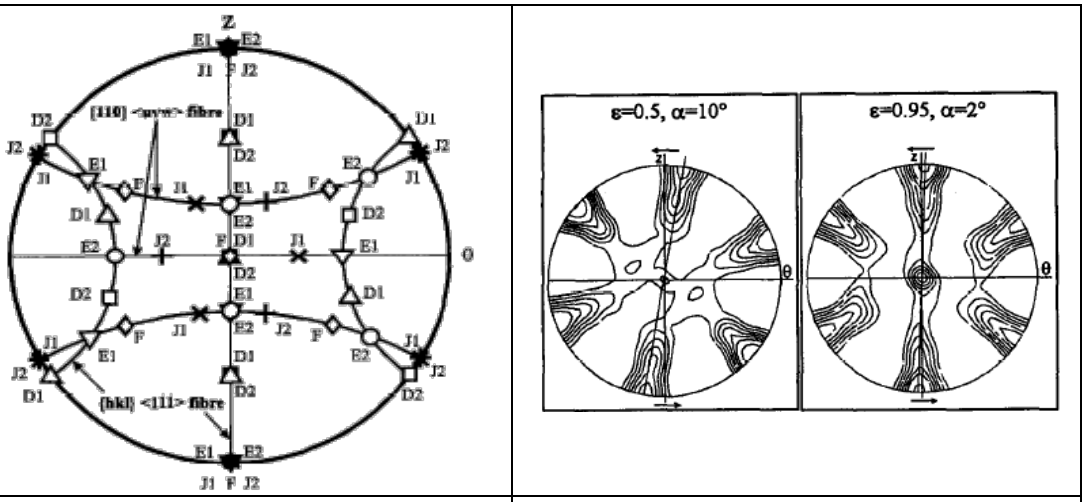

a) b)

FIGURE 5.3: (a) Ideal (110) pole figures for a BCC metal under torsion. (b,c) Experimental (110) pole figures for BCC Fe at different levels of torsion strain [165]. This shearing texture is observed in all locations of HPT processed Ta, indicating that no texture change occurs in the disk.

and are shown in FIGURE 5.3 [165]. These ideal pole figures are similar to the results for the HPT disk reported in FIGURE 3.2. These (110) pole figures showed that a weak shear texture is present at all the disk locations. No change in the texture between the non-shearing and shearing region means it could not explain why there is a transition in the behavior.

Since FIB damage and texture do not give any insight into why the transition occurs, the next thought is that there is a change in the microstructure between the two regions. Jia et al. also observed shear bands in NC Fe samples tested in compression but only once the grain size was equal to, or less than 300 nm [40]. These shear bands also developed over time and multiply with increasing strain. TEM analysis of the microstructures inside and outside the shear band were performed by Wei, and shown in FIGURE 5.4 [67]. There were equiaxed grains outside of the shear band and elongated grains inside the shear band, which suggests signs of rotating into their final positions.

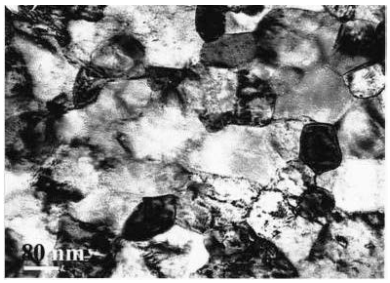

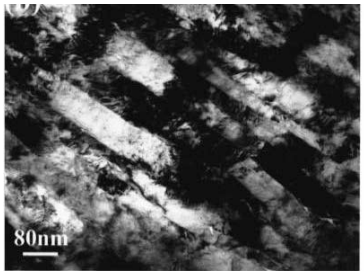

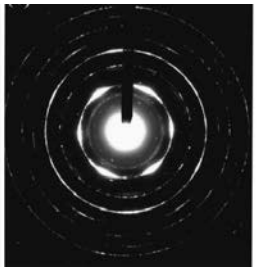

a)	b)	c)

FIGURE 5.4: Results from quasi-static testing of NC Fe that deformed via shear bands, where the bright field TEM image of the un-sheared region (a) shows equiaxed grains while the shear band (b) contains elongated grains. An SAED pattern (c) from inside the band shows a six fold symmetry about the (110) diffraction ring, suggesting a texture form during band propagation [67].

Also, the diffraction pattern from inside the band displays intensity changes along the (110) ring. The shear bands observed in NC Ta share some similar details to those seen in UFG/NC Fe. These include the elongated, thinner grains in the shear band, with equiaxed grains outside it. Also, the TEM images show evidence of grain rotation inside the band. Finally, TEM orientation mapping of the shear band in Ta also shows evidence of a texture forming inside of the band along the <111> direction.

These similarities suggest that the mechanisms causing the shear band to form are the same in both metals. Joshi and Ramesh developed a theory based on geometric softening to explain the transition seen in Fe, where there is a critical grain size below which the grains in the plane of maximum shear stress are susceptible to shear band formation via grain rotation [167, 168]. In a material with a large number of grains (N_b), there are grains in either a “hard” or “soft” single crystal orientation with respect to the shearing direction. Dislocation slip will occur in a number of grains (N_s) in this “soft” orientation. However, the “hard” grains will begin to rotate into the more favorable “soft” orientation for slip. When an internal variable, $\Phi(= N_s/N_b)$, in a region reaches unity, a geometrical softening effect occurs and an instability forms. The rotation rate, $\dot{\Phi}$, in this

model is described by equation 5.3, where the first term is the contribution from overall plasticity and the second from grain-grain interactions. The contribution from overall plastic deformation is due to rigid rotation of the grains, while grain-grain interactions are represented by rotational diffusion (D_r). This rotation is accommodated by neighboring grains through rotation and slip, out to some distance (L) from the origin which causes the band to propagate and widen. Joshi and Ramesh also derived an equation for calculating an initial critical perturbation wavelength (λ_{crit}) of the $\dot{\Phi}$ term needed to cause an instability to form [169]. By incrementally increasing the strain ($\hat{\gamma}_p$) and internal variable (Φ) in equation 5.3 it was found that an instability will form and propagate when the conditions in equation 5.4 and equation 5.5 are met. From these equations the expression for the critical perturbation, $\lambda_{crit,}$ is then given in equation 5.6. The rotation diffusion coefficient, D_r, is defined using equation 5.7, where d is the grain size, j is the number of grains involved in the band, μ is the shear modulus, and υ is Poisson's ratio [167].

$$\dot{\Phi} = \Psi\dot{\gamma}_p + \frac{D_r}{\dot{\gamma}_o L^2}\frac{\partial^2 \Phi}{\partial \hat{X}^2} \qquad \text{equation 5.3}$$

$$\frac{\partial \hat{\gamma}_p^h}{\partial \Phi} > \frac{k^2 D_r}{\Psi\dot{\gamma}_o L^2} \qquad \text{equation 5.4}$$

$$\frac{\partial \hat{\gamma}_p^h}{\partial \Phi} \approx \left(\frac{\bar{c}}{m}\right)\hat{\gamma}_p^h \qquad \text{equation 5.5}$$

$$\lambda_{crit} = \left[\left(\frac{\dot{\gamma}_o \hat{\gamma}_p^h \Psi}{D_r}\left\{\frac{\bar{c}}{m}\right\}\right)^{1/2}\right]^{-1} \qquad \text{equation 5.6}$$

The effective viscosity (η_{eff}) is defined by equation 5.8, which contains contributions from the bulk (η_{bulk}) , equation 5.9, and boundary (η_b) equation 5.10,

viscosities [6, 167]. For these expressions, k_B is the Boltzmann constant, T is temperature, δ the grain boundary thickness, Ω is the atomic volume, and D_{gb} is the grain boundary diffusion coefficient.

$$D_r = \frac{\mu d^2}{(2-\upsilon) j \eta_{eff}} \qquad \text{equation 5.7}$$

$$(\eta_{eff})^{-1} = (\eta_{bulk})^{-1} + (\eta_b)^{-1} \qquad \text{equation 5.8}$$

$$\eta_{bulk} = \frac{\tau_{sO}}{\dot{\gamma}_o} \qquad \text{equation 5.9}$$

$$\eta_b = \frac{k_B T d^3}{64 \delta \Omega 2 D_{gb}} \qquad \text{equation 5.10}$$

Substituting equation 5.7 and equation 5.9 into equation 5.6 gives an expression for λ_{crit} that depends on the grain size (d), equation 5.11 [169]. In this equation, γ_p^h is the plastic strain and Ψ is a fabric factor representing initial texture and grain size effects. There is also a term that represents the strength index, equation 5.12, which depends on the shear modulus, μ, the SRS, m, and an anisotropy factor, equation 5.13. Here the terms τ_{sO} and τ_{hO} represent the shear strength of the soft and hard single crystal orientations of the material.

$$\lambda_{crit} = \left[(2-\upsilon) \Psi \gamma_p^h M \left(\frac{j}{d^2} \right) \left(\frac{\eta_{eff}}{\eta_{bulk}} \right) \right]^{-1/2} \qquad \text{equation 5.11}$$

$$M = \frac{\tau_{sO} \bar{c}}{\mu m} \qquad \text{equation 5.12}$$

$$\bar{c} = 1 - \tau_{sO} / \tau_{hO} \qquad \text{equation 5.13}$$

Using equation 5.11 and the values in TABLE 5.1, λ_{crit} values for both the non-shearing (NS) and shearing (S) regions in HPT Ta were calculated. Values for the single crystal strengths, τ_{sO} and τ_{hO}, are taken from reports by Mitchell and Spitzig [170]. Strength indices in both regions were calculated as, M = 0.0075 for the non-shearing region and M = 0.0105 in the shearing. FIGURE 5.5a shows the plot for λ_{crit} in both regions, where the dashed red line indicates $\lambda_{crit} = d$, meaning when λ_{crit} is equal to or less than the grain size the material is susceptible to the grain rotation mechanism. If it is larger than the grain size then the perturbation can be suppressed by classic stabilization mechanisms such as crystallographic slip. The plots for both regions are close to this line, but the critical grain size, horizontal axis value where this transition occurs, gives 124 nm for the shearing region and 178 nm for the non-shearing region.

Solving equation 5.11 for M and setting $\lambda_{crit} = d$ gives a plot like the one shown in FIGURE 5.5b, making it easier to identify where the transition occurs. In the non-shearing region, the transition to grain rotation instability occurs at ~126 nm and for shearing region the critical grain size increases to ~178 nm. Comparing these critical grain sizes to the cumulative distribution plots, FIGURE 5.6, will give the area

TABLE 5.1: Lists the parameters used for calculating the λ_{crit} and strength index (M) values in both the non-shearing (NS) and shearing (S) regions of the HPT Ta disk. Values for the hard and soft orientations for Ta were taken from reports by Mitchell and Spitzig [170].

	μ (GPa)	ν	$\bar{c}$	m	τ_{sO} (MPa)	Ω(m^3) x 10^{-29}	D_{gb}(m^2/s) x 10^{-20}	M	δ (nm)
NS	69	0.35	0.07	0.0062	68	3.82	1.0	0.0075	1
S	69	0.35	0.07	0.0092	68	3.82	1.0	0.0109	1

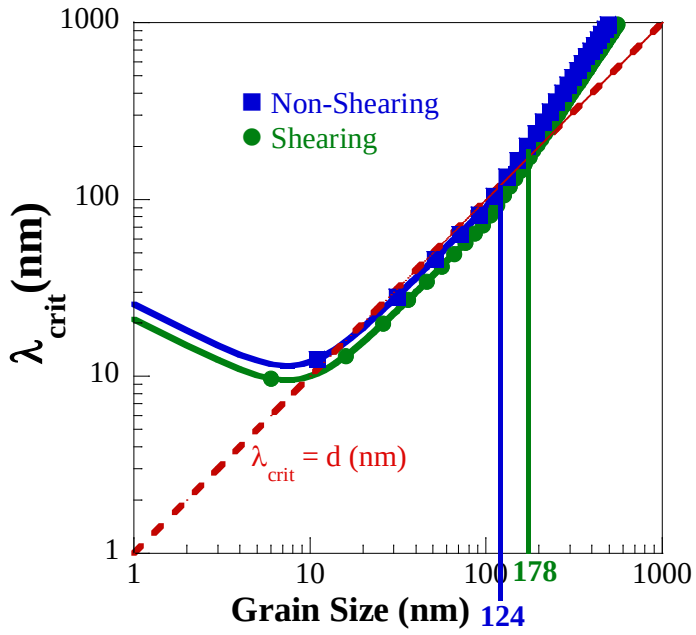

a)

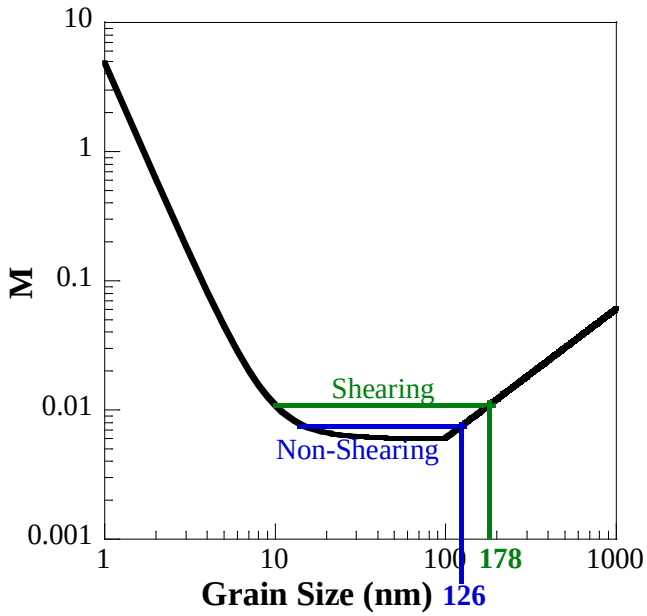

b)

FIGURE 5.5: a) Plot of the λ_{crit} values for both regions on the HPT Ta disk. The dashed red line represent where $\lambda_{crit} = d$, below which the material is considered unstable. Both the non-shearing(blue) and shearing(green) regions cross this line at 124 and 178 nm respectively. (b) Plot of the strength index M for Ta, where the solid black line represents $\lambda_{crit} = d$ and the horizontal lines show the range of unstable grain sizes for the non-shearing (blue) and shearing (green) regions.

fraction of grains in each region where the maximum diameter is smaller than this critical size. The fraction of grains in the non-shearing region below this value is low, and only 11% of the grains have a maximum diameter less than the critical grain size. In this region the grains are large enough to account for the applied stress through dislocation mechanisms. However, in the shearing region there are still 42% of grains smaller than the critical grain size. This makes it more likely that the grains in this region are susceptible to grain rotation mechanism. Therefore we believe this model helps us explain why the transition from homogeneous to localized plastic deformation occurs in the HPT Ta disk.

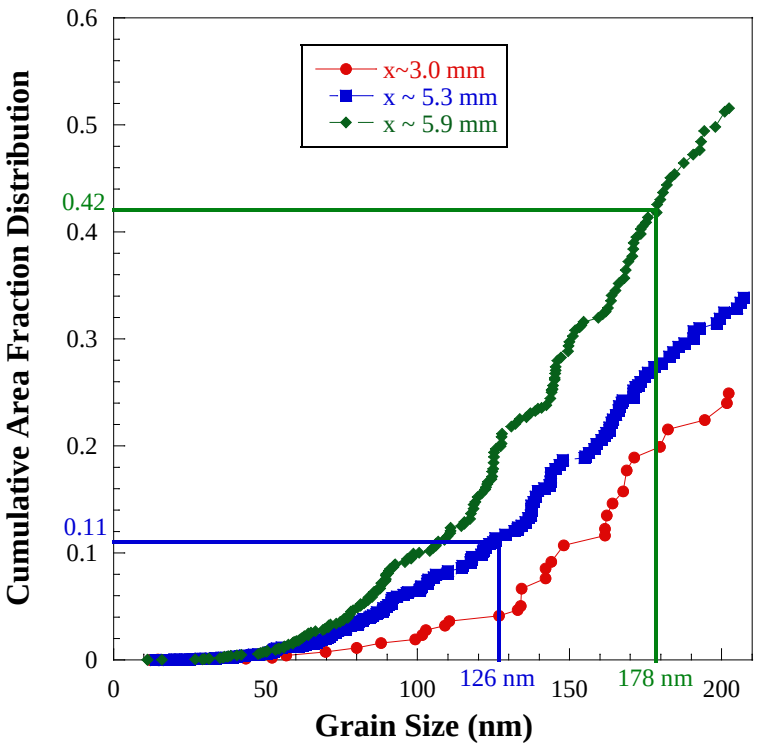

FIGURE 5.6: Reduced range of the cumulative area fraction plot for the maximum grain diameter at locations X = 3.0, 5.3, and 5.9 mm. The vertical lines indicate the necessary critical grain size for each region to undergo the grain rotation mechanism. The corresponding horizontal lines represent the area fraction of grains that are below this critical size. In the shearing region of the disk 42% of the grains are below the critical size, while the non-shearing region only has 11%.

5.4 Tension-Compression Asymmetry

The tension-compression asymmetry was quantified in both the non-shearing and shearing regions of the disk. It is common, when discussing material yielding, to determine at what stress value a material will yield when under different stress states through the use of yield criterion. For this work however, only data for a uniaxial stress state (uniaxial tension or compression) is available for NC Ta. One of the more common criterion is the Tresca yield criterion, which says that yielding occurs when the maximum shear stress in the material equals the maximum shear stress at yielding in a simple tension test [2]. Another commonly used criterion is the von Mises yield criterion [2], where now yielding starts when the maximum distortion/shear energy in the material equals the maximum distortional/shear energy at yielding in a simple tension test. The similarity between these criterions is their reliance on the value of maximum shear stress, which assumes that the deformation is dominated by dislocation motion. Also, both calculate equal yield strengths for uniaxial tension and compression along with the maximum shear stress plane being 45°. There is no asymmetry closer to the disk center, X = 3.2 mm, meaning that the Tresca or von Mises criterion could be used and that dislocation motion is the dominant deformation mechanism.

There is a transition to a higher yield stress in compression compared to tension for radial positions of X > 4.0 mm, suggesting that the Tresca or von Mises criterion cannot be used. In the shearing region, X > 5.3 mm, the specimens deform via shear bands, which in compression formed at an angle with respect to the loading direction of ~ 44 – 46° while in tension at ~ 54°. This change in shear band angle adds to the evidence that, in this region of the disk, the material does not obey either of the previous yield

criterions. Asymmetry in NC metals has been reported on in the literature, and one of the first such reports, by Carsley et al., was on an Fe-10% Cu alloy with grains in the UFG regime [73, 171, 172]. In that work shear bands were also observed in tension and compression under quasi static strain rates where the compressive and tension shear band angles were ~49° and ~54° respectively. Also, the compressive yield strength was ~30% higher than the tensile yield strength. These features led the authors to conclude that, instead of the yield criterion being entirely dependent on the maximum shear stress, there was now a pressure or normal stress dependence.

Most other reports on a tension-compression asymmetry in NC metals are simulations investigating FCC metals. Cheng and coworkers developed a model to calculate the strength of UFG/NC Al, Cu, and Fe, by following the work of Carsley, where a hydrostatic pressure component was added to the equation for the stress needed to bow-out a dislocation source in a grain [173]. This model allowed for prediction of the strength, in tension and compression, along with the presence of an asymmetry that gets more intense as the grain size decreases. Lund and Schuh used molecular dynamics (MD) simulations to produce tensile, compressive, and plane stress states in NC Ni with grain sizes 2 – 4 nm [174]. Their work also shows a tension-compression asymmetry with the yield strength in compression higher than in tension. Plotting the data on a 2-D yield surface showed that neither the Tresca or von Mises criterion accurately matched the data. Instead, a pressure dependent Mohr-Coulomb or Drucker-Prager criterion was used, which gave an excellent fit to the data. These criteria were originally developed to determine the yield behavior for brittle materials and granular solids, where rather than being solely dependent on the maximum shear stress, there is an influence from the

normal stress [175]. Separate simulation reports by Gürses and El Sayed [176] also have shown an increase in compressive over tensile strength and evidence that a pressure component becomes important. These literature results combined with the strength asymmetry and increase in the tensile shear band angle for NC Ta suggests that near the disk edge there is an increase in the pressure dependence on the yield strength.

The reduced dependence on the maximum shear stress also suggests a switch from deformation being based completely on dislocation motion to a possibility for grain boundary motion. Results by Bringa et al. showed that grain boundary plasticity mechanisms, such as GB sliding, in NC Cu are effected by pressure and follow a Mohr-Coulomb type behavior [177]. Gürses and El Sayed also developed a constitutive model for NC Cu that includes competing deformation mechanisms of dislocation emission, and a pressure/normal stress dependence on grain boundary diffusivity and sliding [178]. When the grain size in their model is below ~60 nm there is a strong tension-compression asymmetry, a trait attributed to the plasticity being dominated by grain boundary mechanisms. As was shown by the compression specimens, the deformation mechanism for NC Ta in the shearing region occurs via grain rotation. The presence of an asymmetry in this region is therefore due to the grain rotation mechanism's increased dependence on normal stress over the shear stress dependence for dislocation motion.

During rotation, the movement of the grains around each other could be considered a type of friction, allowing the Mohr-Coulomb criterion to be used to determine yielding. Unfortunately, without having experimental yield strengths for specimens tested under biaxial stress states, it is not possible to determine the best fit yield criterion for this material. However, it is possible to determine some parameters for

the Mohr-Coulomb criterion, equation 5.14, using only the tensile/compressive yield strengths. Here, τ and σ_n represent, respectively, the shear and normal stress acting on

$$\tau = k_o + \alpha\sigma_n \qquad \text{equation 5.14}$$

the plane at yielding, while k_o is the shear yield stress without a normal stress dependence and α is the friction coefficient. Lewandowski et al. studied the effects of a hydrostatic pressure on the yield behavior of BMG in compression and tension and determined that the flow and fracture strength followed the Mohr-Coulomb criterion [179]. Values for k_o and α for their material were determined by the y-intercept and slope, respectively, of the line between the shear and normal stresses in tension and compression. The normal and shear stresses acting on the plane are calculated by equation 5.15 and equation 5.16 respectively [2, 179]. In these equations, $\theta = 90^\circ - \lambda$, where λ is the angle of the shear band with respect to the loading direction, and σ_1 and σ_3 are the principal stresses. In tension, the principal stresses are defined by, the tensile yield stress, $\sigma_y^T = \sigma_1 = 1170$ MPa, and $\sigma_3 = 0$ MPa. For compression, $\sigma_1 = 0$ MPa and the yield stress, $\sigma_y^C = \sigma_3 = -1385$ MPa. Using the parameters listed in TABLE 5.2, the values for τ and σ_n in both tension and compression were plotted, and the line between them gives k_o (y-intercept) = 629 MPa and α (slope) = 0.095. The friction coefficient value measured here

TABLE 5.2: Parameters for calculating the shear yield stress (k_o) and friction coefficient (α) for the Mohr-Coulomb criterion of NC Ta.

Test type	σ_1 (MPa)	σ_3 (MPa)	λ°	θ°	τ	σ_n
Ten.	1170	0	54	36	523	720
Comp.	0	-1385	46	44	650	-627

$$\sigma_n = \frac{(\sigma_1 + \sigma_3)}{2} \cdot sin(2\theta) \qquad \text{equation 5.15}$$

$$\tau = \frac{(\sigma_1 + \sigma_3)}{2} + \left[\frac{(\sigma_1 - \sigma_3)}{2} \cdot cos(2\theta) \right] \qquad \text{equation 5.16}$$

is comparable to the literature values for NC metals of α = 0.03 – 0.11 [174, 177], but tests on NC Ta under only shear must be done to determine the accuracy of the k_o value. Also, performing tension and compression tests with the specimens under hydrostatic pressure, similar to that by Lewandowski et al. [179], will lead to a better fit for these parameters.

5.5 Summary

The SRS was shown to decrease near the edge of the HPT disk edge, which could be due to the increased density of edge type dislocations in NC grains produced via SPD techniques [157]. For positions X < 5.3 mm the tensile specimens failed in a brittle manner but displayed evidence of plasticity in isolated regions on the fracture surfaces. This behavior is attributed to quantized crystal plasticity, where “soft” grains in the specimen volume will slip and advance the local plastic strain but keep the overall strain low [161].

The transition from homogeneous to localized plastic deformation in both tension and compression is due to the less elongated grains present in the shearing region of the disk. A model developed by Joshi and Ramesh predicts a critical grain size necessary for a grain rotation mechanism of shear band formation [169]. Calculations of this critical grain size for HPT Ta show that the minimum diameter in both regions is well below this size. However, for the elongated direction, a larger percentage of the grains in the shearing region are below the critical size, meaning they are more susceptible to the grain

rotation mechanism. This indicates that there is a critical grain size that must be met in all three dimensions in order for the rotation to occur, and this criterion is met in the region X > 5.3 mm.

Closer to the disk center (X < 4.0 mm) the yield strengths in tension and compression are comparable, indicating that a von Mises or Tresca yield criterion could be used to describe yielding and thus dislocation motion is still the dominant mechanism. As the position passes this location however, there is an increase in the strength asymmetry. Literature results on tension-compression asymmetry show evidence that there is increased dependence on the pressure/normal stress in NC metals [173, 174, 176]. This pressure dependence is crucial for the grain rotation mechanism which is active in the region X > 5.3mm [177, 178]. While difficult to determine a best fit criterion, the shear yield stress and frication coefficient of the Mohr-Coulomb criterion were determined to be k_o = 629 MPa and α = 0.095 for NC Ta respectively.

CHAPTER 6: CONCLUSIONS AND FUTURE WORK

6.1 Summary

The goal of this dissertation is to quantify the effects of grain size and other microstructural features such as grain morphology and texture on the quasi-static mechanical properties of UFG/NC Ta, both because of the need for a better understanding of the mechanical behavior of UFG/NC BCC metals at large, and because of the interest in using tantalum as a replacement material in KE penetrators. Tantalum has a high density, propensity to deform via ASBs at high rates [65], and, in the case of coarse grain size, displays higher ductility than many other BCC metals. This combination of properties makes it attractive as a candidate as a model bcc material for the studying of mechanical behavior of UFG/NC BCC metals produced by severe plastic deformation, and as a penetrator material. For the latter, however, the required quasi-static properties must also be known in these grain size regimes [70].

Using HPT, a bulk Ta sample was processed under 5 GPa and N = 5 turns, producing a disk sample that contains a grain size gradient. Site specific mechanical properties were determined by micromechanical testing techniques such as nanoindentation, microcompression and microtension because of the small volume needed for testing [89, 121, 140]. The resulting properties are related back to the underlying microstructure and texture by using TEM and SXRD. Microcompression and microtensile specimens with dimensions on the micron scale were fabricated using FIB

milling at multiple radial positions (X). Compression specimens were tested using a nanoindenter while tension specimens were tested using a custom built *in-situ* SEM stage coupled with DIC based strain calculations [115, 151]. Due to the limited volume of HPT processed Ta, tensile specimens were first made from a coarse grain, 15μm thick Ta foil to determine proper testing specifics such as specimen design, Pt marker dimensions, and imaging parameters. An effective specimen design includes both a longer grip portion for stabilization and a curved gauge section to localize the stress between the Pt markers. These markers allow for the best DIC matching when they are thin lines or small diameter circles and imaged under e-beam settings of 5 kV/0.40 nA with a dwell time of 10 μs. Using these parameters, the elastic modulus for the Ta foil specimens was measured as 189 GPa, which is comparable to the accepted modulus. Therefore, these parameters are used when testing the NC Ta specimens.

To quantify this grain size gradient, both TEM and SXRD based texture analyses were done on the disk. Two-dimensional x-ray patterns show mainly continuous rings near the disk center and slight intensity changes for patterns recorded at the disk edge. All peaks are indexed as BCC Ta, indicating that no phase change occurs during HPT processing. Grain size estimates from XRD show a decreasing grain size with increasing radial distance, which is expected for HPT processed metal. Calculations for (110) pole figures show an expected torsion texture for BCC metals at all disk locations [33, 165]. This texture has an intensity of roughly 2.0 mrd, which is low considering that a value of 1.0 mrd is taken as a random texture. TEM lamellas were taken at three different orientations with respect to the HPT torsion strain and at multiple radial positions to allow for a 3-D representation of the grain shape and structure. Grain size measurements at each location were also made from these TEM images. Along the direction of the

torsion strain the grains show an elongated structure that is in the UFG regime. Perpendicular to the HPT strain the grains are thinner and well within the NC regime at ~40 nm. Area weighted average grain size and cumulative area fraction plots show that the minimum diameter is fairly constant in all regions but the maximum diameter is reduced at the disk edge.

The nanoindentation hardness profile of the disk gives values of ~2.0 GPa near the disk center, which increase to over 4.0 GPa at X = 2.0 mm. For positions greater than this the hardness levels off to ~4.6 GPa due to saturation in the grain refinement. Elastic modulus measurements for all positions average to be ~170 GPa, lower than the accepted value for Ta. Strain rate sensitivity values show a decrease with increasing radial distance, and at X = 1.0, 3.0, 5.3, and 5.9 mm the values for SRS are m = 0.027, 0.0203, 0.0092, and 0.0062, respectively. All these SRS values are lower than the value for coarse grain Ta, m = 0.040-0.060, measured by Wei et al. [66]. From these values the corresponding activation volumes are derived to be $v^* =$ 6.22, 7.9, 17.6, and 26.6b^3, respectively, for these locations. These low SRS measurements are due to the increased density of edge dislocations in NC grains produced via HPT [157].

Using a FIB system, microcompression pillars with diameters ranging from 5 – 10 μm were fabricated at multiple positions on the HPT Ta disk. In the region of $1.0 \leq X \leq 5.3$ mm the pillars have 0.2% yield strength of 1280 ± 95 MPa and show only homogeneous deformation. A tensile specimen fabricated at X = 3.4 mm showed a brittle type failure with low ductility (<1.0%). A specimen at X = 4.0 mm yields at a lower strength, but showed a large increase in the elongation (4.0%) and slight necking before fracture, similar to a ductile failure. The fracture surfaces for both specimens show evidence of localized plasticity, a behavior attributed to the distribution of “hard” or

"soft" crystallographic orientations inside the specimen. Some grains can undergo slip easier than others, resulting in quantized crystal plasticity but low ductility overall [161].

At X > 5.3 mm, both tension and compression specimens showed a transition to localized plastic deformation via shear bands. In compression, the bands formed at an angle of 44 – 46° with respect to the loading direction and have a 0.2% yield strength of 1385 ± 143 MPa. In tension, the bands form at an angle of 54° with respect to loading axis and yield at a lower strength of 1170 ± 21 MPa. TEM lamellas taken of these tested pillars show evidence of grain rotation and texturing inside the band. The transition to shear bands and the observed microstructure are similar to previous reports on NC Fe [40, 67]. The transition in NC Fe occurred below a critical grain size, which can be calculated from a grain rotation based model [167, 169]. Using this model, the critical grain size for Ta to undergo the grain rotation mechanism was calculated. The minimum diameter at all locations is below this critical size, but in the shearing region a larger number of the grains have a maximum diameter below this critical size. This indicates that there is a critical grain size that must be met in all three dimensions in order for the rotation to occur, and this criterion is met in the region X > 5.3 mm.

Tension and compression strengths in the non-shearing region are comparable, indicating that a von Mises or Tresca yield criterion could be used to describe yielding [2]. This also reaffirms that dislocation motion is the main carrier of plasticity in this region. However, closer to the disk edge, the compressive strengths are ~15 – 25% higher, which is consistent with earlier work on a NC Fe-alloy by Carsley et al. [73]. Literature results on tension-compression asymmetry show evidence that there is increased dependence on the pressure and normal stress in NC metals [173, 174, 176]. Initial studies suggest that a Mohr-Coulomb criterion can describe yielding, but

additional studies under biaxial stress must be done to confirm this. Plotting the shear vs. normal stress acting on the shear band plane under both tension and compression allows for determining values for shear yield stress (k_o) and friction coefficient (α) of the Mohr-Coulomb criterion for NC Ta. The former is represented by the y-intercept while the latter is the slope of line between points [179]. These parameters for NC Ta are k_o = 629 MPa, and α = 0.095. Since only uniaxial stress values are available it does not give the ideal values but the friction coefficient measured here is comparable with literature reports [174, 177].

As stated previously, the goal of this dissertation is to quantify the quasi-static mechanical behavior of UFG/NC Ta and relate this behavior back to the underlying microstructure. Properties such as tensile ductility and formation of shear bands at lower strain rates were of particular interest as they will determine if a material could be an appropriate replacement for DU in KE penetrators. Earlier tests showed that NC Ta deforms via ASBs at dynamic rates [65], while this work shows that it is possible for NC Ta to maintain its tensile ductility if the grain size is kept above a critical value in all three dimensions. If below this critical grain size, a NC Ta KE penetrator will deform via shear bands under quasi-static rates, making it unlikely to survive during launch [70].

6.2 Future Work

All tests reported in this work were done along the HPT disk face that was in contact with the platens during processing, meaning the specimens were made in the through thickness of the disk. It has been shown that an elongated grain structure exists at all locations in the Ta disk and the reduction of this dimension causes a transition in the mechanical behavior. Due to this influence it is worthwhile to perform tests along a

different disk face. Microcompression/tension along the cross-section of the disk would allow for the loading to occur in a direction parallel to the torsion strain, or along the elongated grain direction. It is possible that loading along this orientation will result in a different material response in the non-shearing region, however since the elongated direction is reduced at the disk edge it is still expected to deform via shear bands.

Further analysis of the reduced elastic modulus is also needed. Measurements from nanoindentation, microtension, and diamond anvil cell (Appendix A) all show a similar reduced value for the elastic modulus at the disk center. Values at the disk edge give an even lower elastic modulus from microtension, but unfortunately diamond anvil cell specimens from this region were unsuccessful though the data recorded indicates a strong possibility that the elastic modulus is further reduced in this region. Therefore, more DAC tests on multiple disk locations must be done to confirm if the elastic modulus values have a trend with radial position. If confirmed, this means there is an influence from the microstructure since HPT processed metals have no porosity, the reason most commonly associated with the reduced modulus in bottom-up processed metals. An initial explanation for the microstructure influence is the increase in volume fraction of grain boundaries and triple junctions as the grains decrease in size [159]. However, it has been shown that SPD refinement techniques create a large vacancy concentration that depends on hydrostatic pressure and applied shear strain [160]. Both the increased volume fraction of GB/TJ and vacancy concentration could have an effect on the elastic modulus, but these values must be quantified. The vacancy concentration in the disk can be measured by using methods such as differential scanning calorimetry (DSC) or residual electrical resistivity (RER). With these values it will be possible to perform molecular dynamics simulations to investigate and determine the separate influence from

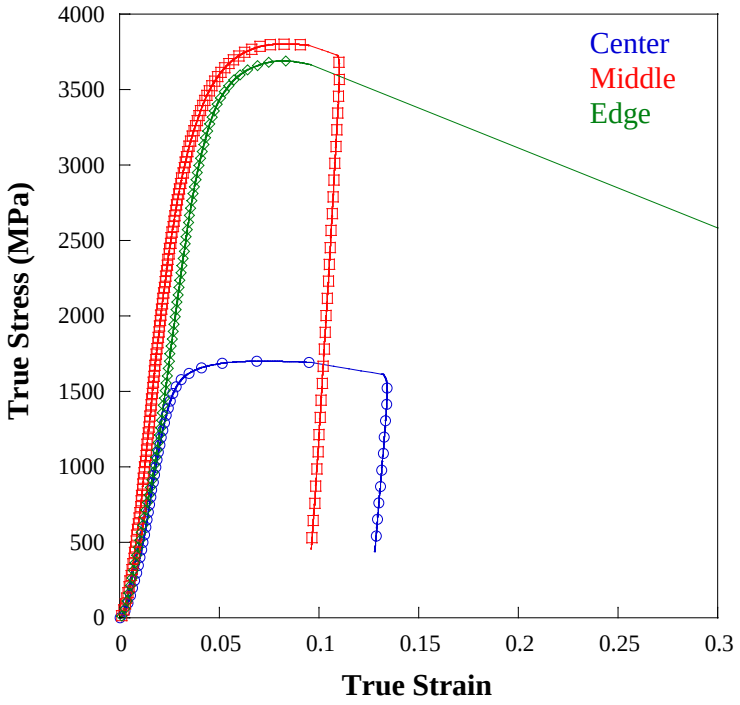

FIGURE 6.1: True stress vs. strain curves for microcompression tests of HPT W specimens fabricated at locations considered the radial center, middle and edge of the processed disk. Behavior at the center position is similar to that observed for coarse grain W. There is also a large increase in the yield strength for the middle and edge specimens, which is expected since these regions correspond to the smallest grain sizes for this material.

grain boundaries and vacancies on the modulus.

These tests on UFG/NC Ta represent only one of the refractory metals available for study, samples of W, V, Cr, Mo, and Nb have also been processed by HPT. Most of these metals have shown the increased susceptibility to form ASBs at dynamic rates, so it is important to use the micromechanical testing techniques to quantify their quasi-static behavior. Of all these refractory metals, W is of most interest for the KE penetrator applications, not only because of the ASB formation but also because its density is comparable to that of DU. Preliminary results for microcompression of HPT W are shown in the true stress vs. strain curves in FIGURE 6.1. These represent specimens

fabricated at positions approximately equal to the radial center (blue), middle (red), and edge (green) of the HPT processed W disk. Even at the center position, where the grains are largest, the strength is above 1.5 GPa, which is stronger than coarse-grain commercial purity W and also stronger than any Ta specimens studied here. The smaller grains in the middle and edge specimens more than double the strength to 3.5 GPa. Ion beam channeling and SEM images of the as milled and tested pillars are shown in FIGURE 6.2a – f. These images show a large influence from the microstructure. The large grains in the center pillar result in formation of dislocation slip lines in the pillar, FIGURE 6.2a and b. Smaller grains make up the middle and edge pillars, FIGURE 6.2c and e, and as a result the pillars show a different deformation behavior. The middle pillar still shows evidence of homogeneous deformation, FIGURE 6.2d, but the dislocation motion here is mostly likely that observed for UFG/NC metals, emission and absorption at grain boundaries. Similar to Ta, the HPT processed W also shows a transition to localized plastic deformation at the disk edge, FIGURE 6.2f. No microstructure investigation was done on these pillars at this point, but it is possible that the grain rotation mechanism is also active at the smallest grain sizes for W as well as Ta.

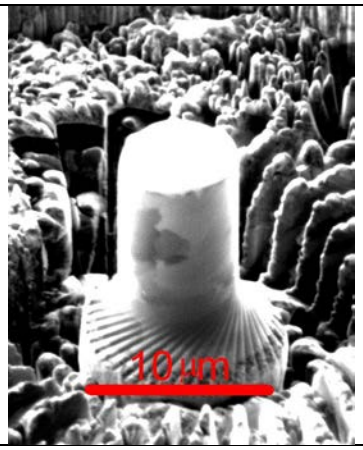

a)

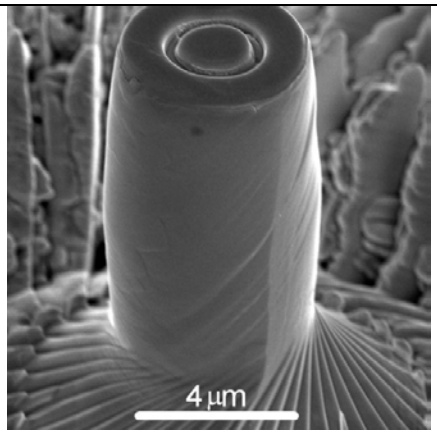

b)

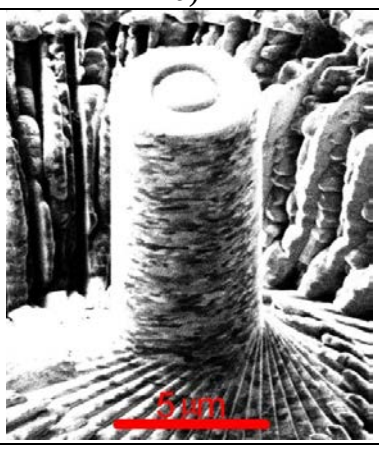

c)

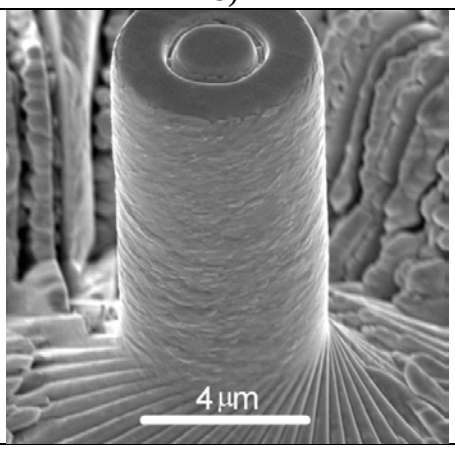

d)

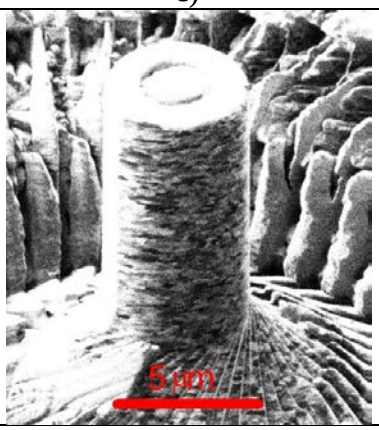

e)

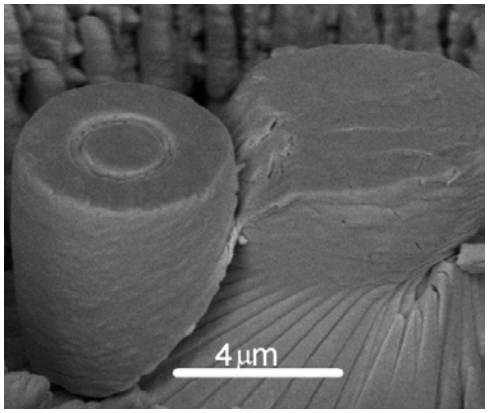

f)

FIGURE 6.2: FIB channeling and SEM images of the HPT W microcompression specimens corresponding to the (a,b) center, (c,d) middle, and (e,f) edge of the disk, clearly showing an influence of the microstructure on the mechanical behavior. The large grains in the disk center (a) result in slip traces on the tested pillar (b) while the smaller grains for the middle (c) and edge (e) specimens result in different deformation behavior.

REFERENCES

[1] W. D. J. Callister, *Materials Science and Engineering: An Introduction*. New York: John Wiley & Sons Inc., 2007.

[2] T. H. Courtney, *Mechanical Behavior of Materials*, Second ed.: Waveland Press, Inc., 2000.

[3] D. R. Askeland and P. P. Phule, *The Science and Engineering of Materials*. Toronto: Nelson, 2006.

[4] E. O. Hall, "The Deformation and Ageing of Mild Steel: III Discussion of Results," *Proceedings of the Physical Society B,* vol. 64, pp. 747-752, 1951.

[5] N. J. Petch, "The Cleavage Strength of Polycrystals," *The Journal of the Iron and Steel Institute,* vol. 174, pp. 25-28, 1953.

[6] M. A. Meyers, *et al.*, "Mechanical properties of nanocrystalline materials," *Progress in Materials Science,* vol. 51, pp. 427-556, May 2006.

[7] R. Peierls, "The Size of a dislocation," *Proceedings of the Physical Society,* vol. 52, pp. 34-37, 1940.

[8] A. Seeger, "The flow stress of high-purity refractory body-centered buci metals and its modification by atomic defects," *Journal de Physique IV,* vol. 5, pp. 45-65, 1995.

[9] L. Hollang, *et al.*, "Work hardening and flow stress of ultrapure molybdenum single crystals," *Materials Science and Engineering A,* vol. 319-321, pp. 233-236., 2001.

[10] Y. J. Chen, *et al.*, "Spontaneous and forced shear localization in high-strain-rate deformation of tantalum," *Materials Science and Engineering A,* vol. 268, pp. 70-82, 1999.

[11] Q. Wei, "Strain rate effects in the ultrafine grain and nanocrystalline regimes—influence on some constitutive responses," *Journal of Materials Science,* vol. 42, pp. 1709-1727, 2007.

[12] K. M. Lee, *et al.*, "XRD and TEM studies on tin oxide (II) nanoparticles perpared by inert gas condensation," *Materials Letters,* vol. 58, pp. 3122-3125, 2004.

[13] C. Cheung, *et al.*, "ELECTRODEPOSITION OF NANOCRYSTALLINE Ni-Fe ALLOYS," *Nanostructured Materials,* vol. 5, pp. 513-523, 1995.

[14] K. S. Kumar, *et al.*, "Deformation of electrodeposited nanocrystalline nickel," *Acta Materialia,* vol. 51, pp. 387-405., 2003.

[15] K. A. Darling, *et al.*, "Grain-size stabilization in nanocrystalline FeZr alloys," *Scripta Materialia,* vol. 59, pp. 530-533, 2008.

[16] R. Z. Valiev, "Structure and mechanical properties of ultrafine-grained metals," *Materials Science and Engineering A,* vol. 234-236, pp. 59-66, 1997.

[17] R. Z. Valiev, *et al.*, "Bulk nanostructured materials from severe plastic deformation," *Progress in Materials Science,* vol. 45, pp. 103-189, 2000.

[18] Y. Saito, *et al.*, "Novel ultra-high straining process for bulk materials - Development of the accumulative roll-bonding (ARB) process," *Acta Materialia,* vol. 47, pp. 579-583, 1999.

[19] N. Tsuji, *et al.*, "ARB (Accumulative roll-bonding) and other new techniques to produce bulk ultrafine grained materials," *Advanced Engineering Materials,* vol. 5, pp. 338-344, 2003.

[20] Q. Guo, *et al.*, "Grain refinement in as-cast AZ80 Mg alloy under large strain deformation," *Materials Characterization,* vol. 58, pp. 162-167, 2007.

[21] I. J. Beyerlein and L. S. Toth, "Texture evolution in equal-channel angular extrusion," *Progress in Materials Science,* vol. 54, pp. 427-510, 2009.

[22] Y. Ivanisenko, *et al.*, "Grain boundary statistics in nano-structured iron produced by high pressure torsion," *Materials Science and Engineering a-Structural Materials Properties Microstructure and Processing,* vol. 390, pp. 159-165, Jan 2005.

[23] R. Z. Valiev, *et al.*, "Structure and deformation behavior of Armco iron subjected to severe plastic deformation," *Acta Materialia,* vol. 44, pp. 4705-4712, 1996.

[24] M. Shaarbaf and M. R. Toroghinejad, "Nano-grained copper strip produced by accumulative roll bonding," *Materials Science and Engineering A,* vol. 473, pp. 28-33, 2008.

[25] J. S. Carpenter, *et al.*, "Bulk texture evolution of Cu–Nb nanolamellar composites during accumulative roll bonding," *Acta Materialia,* vol. 60, pp. 1576-1586, 2012.

[26] R. Z. Valiev and T. G. Langdon, "Principles of equal-channel angular pressing as a processing tool for grain refinement," *Progress in Materials Science,* vol. 51, pp. 881-981, 2006.

[27] Y. Iwahashi, *et al.*, "The processed of grain refinement in equal-channel angular pressing," *Acta Materialia,* vol. 46, pp. 3317-3331, 1998.

[28] V. Stolyarov, *et al.*, "Influence of ECAP routes on the microstructure and properties of pure Ti," *Materials Science and Engineering A,* vol. 299, pp. 59-67, 2001.

[29] P. W. Bridgman, "On Torsion Combined with Compression," *Journal of Applied Physics,* vol. 14, pp. 273-283, 1943.

[30] T. Hebesberger, *et al.*, "Structure of Cu deformed by high pressure torsion," *Acta Materialia,* vol. 53, pp. 393-402, 2005.

[31] A. P. Zhilyaev and T. G. Langdon, "Using high-pressure torsion for metal processing: Fundamentals and applications," *Progress in Materials Science,* vol. 53, pp. 893-979, 2008.

[32] K. Edalati, *et al.*, "Microstructural characteristics of tungsten-base nanocomposites produced from micropowders by high-pressure torsion," *Acta Materialia,* vol. 60, pp. 3885-3893, 2012.

[33] N. A. Enikeev, *et al.*, "Observations of texture in large scale HPT-processed Cu," *Materials Science Forum,* vol. 584-586, pp. 367-374, 2008.

[34] S. Cheng, *et al.*, "Tensile Properties of in situ consolidated nanocrystalline Cu," *Acta Materialia,* vol. 53, pp. 1521-1533, 2005.

[35] H. Wei, *et al.*, "The effect of gauge volume on the tensile properties of nanocrystalline electrodeposits," *Scripta Materialia,* vol. 57, pp. 996-999, 2007.

[36] A. Djekoun, *et al.*, "Characterization of Fe and Fe50Ni50 ultrafine nanoparticles synthesized by inert gas-condensation method," *Physica B,* vol. 404, pp. 3824-3829, 2009.

[37] S. Zherebtsov, *et al.*, "Strength and ductility-related properties of ultrafine grained two-phase titanium alloy produced by warm multiaxial forging," *Materials Science and Engineering A,* vol. 536, pp. 190-196, 2012.

[38] Q. Wei, *et al.*, "Ultrafine and Nanostructured Refractory Metals Processed by SPD: Microstructure and Mechanical Properties," *Materials Science Forum,* vol. 579, pp. 75-90, 2008.

[39] Q. Wei, *et al.*, "Microstructure and mechanical properties of super-strong nanocrystalline tungsten processed by high-pressure torsion," *Acta Materialia,* vol. 54, 2006.

[40] D. Jia, *et al.*, "Effects of nanocrystalline and ultrafine grain sizes on constitutive behavior and shear bands in iron," *Acta Materialia*, vol. 51, pp. 3495-3509, 2003.

[41] A. H. Chokshi, *et al.*, "On the Validity of the Hall-Petch Relationship in Nanocrystalline Materials," *Scripta Metallurgica*, vol. 23, pp. 1679-1683, Oct 1989.

[42] F. C. Frank and W. T. Read Jr., "MULTIPLICATION PROCESSES FOR SLOW MOVING DISLOCATIONS," *Physical Review*, vol. 79, pp. 722-723, 1950.

[43] D. Jia, *et al.*, "Failure Mode and Dynamic Behavior of Nanophases Iron Under Compression," *Scripta Materialia*, vol. 42, pp. 73-78, 2000.

[44] D. Jia, *et al.*, "Deformation behavior and plastic instabilities of ultrafine-grained titanium," *Applied Physics Letters*, vol. 79, pp. 611-613, 2001.

[45] V. Yamakov, *et al.*, "Dislocation processes in the deformation of nanocrystalline aluminium by molecular-dynamics simulation," *Nature Materials*, vol. 1, pp. 45-48, Sep 2002.

[46] C. C. Koch, "Optimization of the strength and ductility in nanocrystalline and ultrafine grained metals," *Scripta Materialia*, vol. 49, pp. 657-662, 2003.

[47] F. Ebrahimi, *et al.*, "Deformation and fracture of electrodeposited copper," *Scripta Materialia*, vol. 39, pp. 315-321., 1998.

[48] C. C. Koch, "Ductility in nanostructured and ultra fine-grained materials: Recent Evidence for optimism," *Journal of Metastable and Nanocrystalline Materials*, vol. 18, pp. 9-20, 2003.

[49] A. F. Zimmerman, *et al.*, "Mechanical properties of nickel silicon carbide nanocomposites," *Materials Science and Engineering A*, vol. 328, pp. 137-146, 2002.

[50] Y. M. Wang, *et al.*, "Enhanced tensile ductility and toughness in nanostrucutured Cu," *Applied Physics Letters*, vol. 80, pp. 2395-2397, 2002.

[51] L. Lu, *et al.*, "Ultrahigh Strength and High Electrical Conductivity in Copper," *Science*, vol. 304, pp. 422-426, 2004.

[52] Q. Wei, *et al.*, "Effect of nanocrystalline and ultrafine grain sizes on the strain rate sensitivity and activation volume: fcc versus bcc metals," *Materials Science and Engineering a-Structural Materials Properties Microstructure and Processing*, vol. 381, pp. 71-79, Sep 2004.

[53] H. Conrad, *High-strength materials*. New York: Wiley, 1965.

[54] J. E. Dorn and S. Rajnak, "Nucleation of kink-pairs and the peierls mechanism of plastic deformation," *Transactions of the Metallurgical Society of AIME,* vol. 230, pp. 1052-1064, 1964.

[55] H. Van Swygenhoven and J. R. Weertman, "Deformation in Nanocrystalline Metals," *Materials Today,* vol. 9, pp. 24-31, 2006.

[56] P. Liu, *et al.*, "Direct dynamic atomic mechanisms of strain-induced grain rotation in nanocrystalline, textured, columnar-structured thin gold films," *Scripta Materialia,* vol. 64, pp. 343-346, 2011.

[57] D. S. Gianola, *et al.*, "Stress-assisted discontinuous grain growth and its effects on the deformation behavior of nanocrystalline aluminum thin films," *Acta Materialia,* vol. 54, pp. 2253-2263, 2006.

[58] D. A. Konstantinidis and E. C. Aifantis, "On the "anomalous" hardness of nanocrystalline materials," *Nanostructured Materials,* vol. 10, pp. 1111-1118, Oct 1998.

[59] H. Van Swygenhoven and P. M. Derlet, "Grain-boundary sliding in nanocrystalline fcc metals," *Physical Review B,* vol. 64, 2001.

[60] J. A. Sharon, *et al.*, "Stress-driven grain growth in nanocrystalline Pt thin films," *Scripta Materialia,* vol. 64, pp. 25-28, 2011.

[61] A. E. Romanov and A. L. Kolesnikova, "Application of disclination concept to solid structures," *Progress in Materials Science,* vol. 54, pp. 740-769, 2009.

[62] J. W. Cahn and J. E. Taylor, "A unified approach to motion of grain boundaries, relative tangential translation along grain boundaries, and grain rotation," *Acta Materialia,* vol. 52, pp. 4887-4898, 2004.

[63] Q. Wei, *et al.*, "Dynamic behaviors of body-centered cubic metals with ultrafine grained and nanocrystalline microstructures," *Materials Science and Engineering a-Structural Materials Properties Microstructure and Processing,* vol. 493, pp. 58-64, Oct 2008.

[64] Q. Wei, *et al.*, "Nanoengineering opens a new era for tungsten as well," *JOM,* vol. 58, pp. 40-44, Sep 2006.

[65] Q. Wei, *et al.*, "Microstructure and mechanical properties at different length scales and strain rates of nanocrystalline tantalum produced by high-pressure torsion," *Acta Materialia,* vol. 59, pp. 2423-2436, 2011.

[66] Q. Wei, *et al.*, "Microstructure and mechanical properties of tantalum after equal channel angular extrusion (ECAE)," *Materials Science and Engineering A,* vol. 358, pp. 266-272, 2003.

[67] Q. Wei, *et al.*, "Evolution and microstrucure of shear bands in nanostructured Fe," *Applied Physics Letters,* vol. 81, pp. 1240-1242, 2002.

[68] Q. Wei, *et al.*, "Nano-structured vanadium: processing and mechanical properties under quasi-static and dynamic compression," *Scripta Materialia,* vol. 50, pp. 359-364, 2004.

[69] T. W. Wright, *The physics and mathematics of adiabatic shear bands*: Cambridge Press, 2002.

[70] B. E. Schuster, *et al.*, "Nanocrystalline Refractory Metals for Extreme Condition Applications," *JOM,* vol. 63, pp. 27-31, 2011.

[71] L. S. Magness and T. G. Farrand, "Deformation Behavior and its Relation to the Penetration Performace of High-Density KE Penetrator materials," *Proceedings of the Army Science Conference.*, pp. 465-479, 1990.

[72] T. R. Malow, *et al.*, "Compressive mechanical behavior of nanocrystalline Fe investigated with an automated ball indentation technique," *Materials Science and Engineering A,* vol. 252, pp. 36-43., 1998.

[73] J. E. Carsley, *et al.*, "Mechanical Behavior of a Bulk Nanostrucutred Iron Alloy," *Metallurgical and Materials Transactions a-Physical Metallurgy and Materials Science,* vol. 29A, pp. 2261-2271, 1998.

[74] J. R. Trelewicz and C. A. Schuh, "The Hall-Petch breakdown in nanocrystalline metals: A crossover to glass-like deformation," *Acta Materialia,* vol. 55, pp. 5948-5958, 2007.

[75] R. M. Langford, *et al.*, "Focused ion beam micro- and nanoengineering," *MRS Bulletin,* vol. 32, pp. 417-423, May 2007.

[76] J. Melngailis, "FOCUSED ION-BEAM TECHNOLOGY AND APPLICATIONS," *Journal of Vacuum Science & Technology B,* vol. 5, pp. 469-495, Mar-Apr 1987.

[77] J. Mayer, *et al.*, "TEM sample preparation and FIB-induced damage," *MRS Bulletin,* vol. 32, pp. 400-407, May 2007.

[78] FEI. Available: http://www.fei.com/products/components/

[79] J. Orloff, *et al.*, *High Resolution Focused Ion Beams*. New York: Kluwer Academic/Plenum Publishers, 2003.

[80] C. A. Volkert and A. M. Minor, "Focused ion beam microscopy and micromachining," *MRS Bulletin,* vol. 32, pp. 389-395, May 2007.

[81] L. A. Giannuzzi and A. S. Fred, Eds., *Introduction to Focused Ion Beams*. New York: Springer Science+Business Media Inc., 2005.

[82] J. F. Ziegler. *PARTICLE INTERACTIONS WITH MATTER* Available: http://www.srim.org/

[83] J. A. El-Awady, *et al.*, "Effects of focused ion beam induced damage on the plasticity of micropillars," *Physical Review B,* vol. 80, p. 5, Sep 2009.

[84] Y. Fu and N. K. A. Bryan, "Investigation of physical properties of quartz after focused ion beam bombardment," *Applied Physics B,* vol. 80, pp. 581-585, 2005.

[85] H. Bei, *et al.*, "Effects of focused ion beam milling on the nanomechanical behavior of a molybdenum-alloy single crystal," *Applied Physics Letters,* vol. 91, p. 111915, 2007.

[86] S. Shim, *et al.*, "Effects of focused ion beam milling on the compressive behavior of directionally solidified micropillars and the nanoindentation response of an electropolished surface," *Acta Materialia,* vol. 57, pp. 503-510, 2009.

[87] G. M. Pharr and R. F. Cook, "Instrumentation of a Conventional Hardness Tester for Load-Displacement Measurement during Indentation," *Journal of Materials Research,* vol. 5, pp. 847-851, Apr 1990.

[88] W. C. Oliver and G. M. Pharr, "An Improved Technique for Determining Hardness and Elastic-Modulus Using Load and Displacement Sensing Indentation Experiments," *Journal of Materials Research,* vol. 7, pp. 1564-1583, Jun 1992.

[89] W. C. Oliver and G. M. Pharr, "Measurement of hardness and elastic modulus by instrumented indentation: Advances in understanding and refinements to methodology," *Journal of Materials Research,* vol. 19, pp. 3-20, Jan 2004.

[90] H. Huang, *et al.*, "Mechanical properties of single crystal tungsten microwhiskers characterized by nanoindentation," *Materials Science and Engineering a-Structural Materials Properties Microstructure and Processing,* vol. 523, pp. 193-198, Oct 2009.

[91] T. H. Fang and W. J. Chang, "Nanomechanical properties of copper thin films on different substrates using the nanoindentation technique," *Microelectronic Engineering,* vol. 65, pp. 231-238, 2003.

[92] M. R. VanLandingham, *et al.*, "Nanoindentation of Polymers: An Overview," *Macromolecular*, vol. 167, pp. 15-43, 2001.

[93] C. A. Schuh and T. G. Nieh, "A nanoindentation study of serrated flow in bulk metallic glasses," *Acta Materialia*, vol. 51, pp. 87-99, 2003.

[94] J. L. Cuy, *et al.*, "Nanoindentation mapping of the mechanical properties of human molar tooth enamel," *Archives of Oral Biology*, vol. 47, pp. 281-291, 2002.

[95] F. Haque, "Application of nanoindentation to development of biomedical materials," *Surface Engineering*, vol. 19, pp. 255-268, 2003.

[96] S. Min Han, *et al.*, "Determining hardness of thin films in elastically mismatched film-on-substrate systems using nanoindentation," *Acta Materialia*, vol. 54, pp. 1571-1581, 2006.

[97] R. Saha and W. D. Nix, "Effects of the substrate on the determination of thin film mechanical properties by nanoindentation," *Acta Materialia*, vol. 50, pp. 23-38, 2002.

[98] W. D. Nix and H. Gao, "Indentation size effects in crystalline materials: A law for strain gradient plasticity," *Journal of the Mechanics and Physics of Solids*, vol. 46, pp. 411-425, 1998.

[99] M. D. Uchic, *et al.*, "Sample Dimensions Influence Strength and crystal plasticity," *Science*, vol. 305, pp. 986-989, 2004.

[100] M. D. Uchic and D. M. Dimiduk, "A methodology to investigate size scale effects in crystalline plasticity using uniaxial compression testing," *Materials Science and Engineering A*, vol. 400-401, pp. 268-278, 2005.

[101] S. S. Brenner, "Plastic deformation of copper and silver whiskers," *Journal of applied physics*, vol. 28, pp. 1023-1026, 1957.

[102] S. S. Brenner, "Tensile Strength of Whiskers " *Journal of applied physics*, vol. 27, pp. 1484-1491, 1956.

[103] J. R. Greer, *et al.*, "Size dependence of mechanical properties of gold at the micron scale in the absence of strain gradients," *Acta Materialia*, vol. 53, pp. 1821-1830, 2005.

[104] D. M. Dimiduk, *et al.*, "Size-affected single-slip behavior of pure nickel microcrystals," *Acta Materialia*, vol. 53, pp. 4065-4077, 2005.

[105] J. Y. Kim and J. R. Greer, "Size-dependent mechanical properties of molybdenum nanopillars," *Applied Physics Letters,* vol. 93, p. 3, Sep 2008.

[106] D. Kaufmann, *et al.*, "Size dependent mechanical behavior of tantalum," *International Journal of Plasticity,* vol. 27, pp. 470-478, 2011.

[107] J. Y. Kim, *et al.*, "Insight into the deformation behavior of niobium single crystals under uniaxial compression and tension at the nanoscale," *Scripta Materialia,* vol. 61, pp. 300-303, Aug 2009.

[108] H. Bei, *et al.*, "Compressive strengths of molybdenum alloy micro-pillars prepared using a new technique," *Scripta Materialia,* vol. 57, pp. 397-400, 2007.

[109] B. E. Schuster, *et al.*, "Microcompression of nanocrystalline nickel," *Applied Physics Letters,* vol. 88, Mar 2006.

[110] B. E. Schuster, *et al.*, "Bulk and microscale compressive properties of a Pd-based metallic glass," *Scripta Materialia,* vol. 57, pp. 517-520, 2007.

[111] D. Jang, *et al.*, "Effects of size on the strength and deformation mechanism in Zr-based metallic glasses," *International Journal of Plasticity,* vol. 27, pp. 858-867, 2011.

[112] A. J. Clarke, *et al.*, "A microcompression study of shape-memory deformation in U–13 at.% Nb," *Scripta Materialia,* vol. 60, pp. 890-892, 2009.

[113] N. A. Mara, *et al.*, "Ultrahigh strength and ductility of Cu-Nb Nanolayered composites," *Materials Science Forum,* vol. 633-634, pp. 647-653, 2011.

[114] M. C. Liu, *et al.*, "Is the compression of tapered micro- and nanopillar samples a legitimate technique for the identification of deformation mode change in metallic glasses?," *Scripta Materialia,* vol. 66, pp. 817-820, 2012.

[115] H. Zhang, *et al.*, "The desing of accurate micro-compression experiments," *Scripta Materialia,* vol. 54, pp. 181-186, 2006.

[116] J. Sharpe, W.N., *et al.*, "A new technique for measuring the mechanical properties of thin films," *Journal of microelectromechanical systems,* vol. 6, pp. 193-199, 1997.

[117] K. J. Hemker and J. Sharpe, W.N., "Microscale Characterization of Mechanical Properties," *Annual Review of Materials Research,* vol. 37, 2007.

[118] D. S. Gianola and C. Eberl, "Micro- and nanoscale tensile testing of materials," *Journal of the Minerals, Metals and Materials Society,* vol. 61, pp. 24-35, Mar 2009.

[119] D. S. Gianola and J. Sharpe, W.N., "Techniques for testing thin films in tension," *Experimental Techniques,* vol. 28, pp. 23-27, 2004.

[120] D. Kiener, *et al.*, "A further step toward an understanding of size-dependent crystal plasticity: In situ tension experiments of miniaturized single-crystal copper samples," *Acta Materialia,* vol. 56, pp. 580-592, 2008.

[121] J. Y. Kim, *et al.*, "Tensile and compressive behavior of tungsten, molybdenum, tantalum, and niobium at the nanoscale," *Acta Materialia,* vol. 58, pp. 2355-2363, 2010.

[122] J. Y. Kim and J. R. Greer, "Tensile and compressive behavior of gold and molybdenum single crystals at the nano-scale," *Acta Materialia,* vol. 57, pp. 5245-5253, 2009.

[123] D. Kiener, *et al.*, "A Further step towards and understanding of size-dependent crystal plasticity in situ tension experiements of minatureized single-crystal copper samples," *Acta Materialia,* vol. 56, pp. 580-592, 2008.

[124] P. A. Shade, "Small Scale MEchanical Testing Techniques and Application to Evaluate a single crystal Nickel Superalloy," *OSU Dissertation,* 2008.

[125] C. Hatchett, "An Analysis of a Mineral Substance from North America, Containing a Metal Hitherto Unknown," *Philosophical Transactions,* vol. 92, 1802.

[126] W. H. Wollaston, "On the Identity of Columbium and Tantalum," *Philosophical Transactions,* vol. 99, pp. 246-252, 1809.

[127] M. Zhang, *et al.*, "Nanocrystalline tetragonal tantalum thin films," *Scripta Materialia,* vol. 57, pp. 1032-1035, 2007.

[128] MatWeb. Available: www.matweb.com

[129] M. Zhang, *et al.*, "Hardness enhancement in nanocrystalline tantalum thin films," *Scripta Materialia,* vol. 54, pp. 1227-1230, 2006.

[130] S. N. Mathaudhu and K. T. Hartwig, "Grain refinement and recrystallization of heavily worked tantalum," *Materials Science and Engineering A,* vol. 426, pp. 128-142, 2006.

[131] S. N. Mathaudhu and K. T. Hartwig, "Processing microstructure property relationships in severely deformed tantalum," *Materials Science and Engineering A,* vol. 463, pp. 94-100, 2007.

[132] Z. L. Pan, *et al.*, "Tensile properties of nanocrystalline tantalum from molecular dynamics simulations," *Acta Materialia,* vol. 56, pp. 3470-3480, Aug 2008.

[133] R. Z. Valiev, *et al.*, "Producing bulk ultrafine-grained materials by severe plastic deformation," *JOM,* vol. 58, pp. 33-39, 2006.

[134] K. E. Harris, *et al.*, "Grain Rotation in Thin Films of Gold," *Acta Materialia,* vol. 46, pp. 2623-2633, 1998.

[135] A. S. Mohammadabadi and K. Dehghani, "A new model for inverse Hall-Petch relation of nanocrystalline materials," *Journal of Materials Engineering and Performance,* vol. 17, pp. 662-666, Oct 2008.

[136] S. Takeuchi, "The mechanism of the inverse Hall-Petch relation of nanocrystals," *Scripta Materialia,* vol. 44, pp. 1483-1487, May 2001.

[137] Q. Wei, *et al.*, "Mechanical behavior and dynamic failure of high-strength ultrafine grained tungsten under uniaxial compression," *Acta Materialia,* vol. 54, pp. 77-87, 2006.

[138] Q. Wei, *et al.*, "Adiabatic shear banding in ultrafine-grained Fe processed by severe plastic deformation," *Acta Materialia,* vol. 52, pp. 1859-1869, 2004.

[139] J. R. Greer and J. T. M. De Hosson, "Plasticity in small-sized metallic systems: Intrinsic versus extrinsic size effect," *Progress in Materials Science,* vol. 56, pp. 654-724, 2011.

[140] M. D. Uchic, *et al.*, "Plasticity of Micrometer-Scale Single Crystals in Compression," *Annual Review of Materials Research,* vol. 39, pp. 361-386, 2009.

[141] G. T. Murray and R. A. Burn, "The mechanical properties of Tantalum with special reference to the ductile-brittle transition," Materials Research Corporation, Orangeburg1963.

[142] L. Wcislak, *et al.*, "Texture analysis with high-energy synchrotron radiation," *Journal of applied crystallography,* vol. 35, pp. 82-95, 2002.

[143] H. R. Wenk, *et al.*, "Texture analysis from driffraction spectra," *Materials Science Forum,* vol. 157-162, pp. 473-480, 1994.

[144] L. Lutterotti, *et al.*, "Texture, Residual Stress and Structural Analysis of Thin Films using a Combined X-Ray Analysis," *Thin Solid Films,* vol. 450, pp. 34-41, 2004.

[145] S. Matthies, *et al.*, "Advances in Texture Analysis from Diffraction Spectra," *Journal of Applied Crystallography,* vol. 30, pp. 31-42, 1997.

[146] H. G. Jiang, *et al.*, "On the applicability of the x-ray diffraction line profile analysis in extracting grain size and microstrain in nanocrystalline materials," *Journal of Materials Research,* vol. 14, pp. 549-559, 1999.

[147] D. Balzar and N. C. Popa, "Analyzing Microstructure by Rietveld Refinement," *The Rigaku Journal,* vol. 22, pp. 16-25, 2005.

[148] V. Maier, *et al.*, "Nanoindentation strain-rate jump tests for determining the local strain-rate sensitivity in nanocrystalline Ni and ultra fine grained Al," *Journal of Materials Research,* vol. 26, pp. 1421-1430, 2011.

[149] J. Portillo, *et al.*, "Precession electron diffraction assisted orientation mapping in the transmission electron microscope," *Materials Science Forum,* vol. 644, pp. 1-7, 2010.

[150] J. Bennett. (2012). *AutoIT.* Available: http://www.autoitscript.com/site/

[151] J. Sharpe, W.N., *et al.*, "Strain measurements of silicon dioxide microspecimens by digital imaging processing," *Experimental Mechanics,* vol. 47, pp. 649-658, 2007.

[152] B. D. Lucas and T. Kanade, "An Iterative image registration technique with an application to stereo visioin," *Proceedings of Imaging Understanding Workshop,* pp. 121-130, 1981.

[153] A. R. Kilmametov, *et al.*, "Texture analysis of nanostructured metals produced by severe plastic deformation," *Materials Science Forum,* vol. 443-444, pp. 243-246, 2004.

[154] R. Pippan, *et al.*, "Saturation of gragmentation during severe plastic deformation," *Annual Review of Materials Research,* vol. 40, pp. 319-343, 2010.

[155] J. Cizek, *et al.*, "Evolution of defects in copper deformed by high-pressure torsion," *Acta Materialia,* vol. 59, pp. 2322-2329, 2011.

[156] D. Tabor, "The Hardness and Strength of Metals," *J. Inst. Met.*, vol. 79, 1951.

[157] G. M. Cheng, *et al.*, "Grain size effect on deformation mechanisms of nanocrystalline bcc metal," *Materials Research Letters,* vol. 1, pp. 1-6, 2012.

[158] H. S. Kim and M. B. Bush, "The Effects of grain size and porosity on the elastic modulus of nanocrystalline materials," *Nanostructured Materials,* vol. 11, pp. 361-367, 1999.

[159] Y. Zhou, *et al.*, "The effects of triple junctions and grain boundaries on hardness and Young's modulus in nanostructured Ni-P," *Scripta Materialia,* vol. 48, pp. 825-830, 2003.

[160] D. Setman, *et al.*, "The presence and nature of vacancy type defects in nanometals detained by severe plastic deformation," *Materials Science and Engineering A,* vol. 493, pp. 116-122, 2008.

[161] L. Li, *et al.*, "The stress-strain response of nanocrystalline metals: A quantized crystal plasticity approach," *Acta Materialia,* vol. 57, pp. 812-822, 2009.

[162] L. Li, *et al.*, "Slip-induced intergranular stress redistribution in nanocrystalline Ni," *Acta Materialia,* 2012.

[163] L. Li, *et al.*, "Probing the relation between dislocation substructure and indentation characteristics using quantized crystal plasticity," *Journal of Applied Mechanics-Transactions of the ASME,* vol. 79, p. 031009, 2012.

[164] H. Bei, *et al.*, "Effects of pre-strain on the compressive stress-strain response of Mo-alloy single-crystal micropillars," *Acta Materialia,* vol. 56, pp. 4762-4770, 2008.

[165] J. Baczynski and J. J. Jonas, "Texture development during the torsion testing of alpha-iron and two IF steels," *Acta Materialia,* vol. 44, pp. 4273-4288, 1996.

[166] M. Kuroda and V. Tvergaard, "Effects of texture on shear band formation in plane strain tension/compression and bending," *International Journal of Plasticity,* vol. 23, pp. 244-272, 2007.

[167] S. P. Joshi and K. T. Ramesh, "Rotational diffusion and grain size dependent shear instability in nanostructured materials," *Acta Materialia,* vol. 56, pp. 282-291, 2008.

[168] S. P. Joshi and K. T. Ramesh, "Grain size dependent shear instabilities in body-centered and face-centered cubic materials," *Materials Science and Engineering A,* vol. 493, pp. 65-70, 2008.

[169] S. P. Joshi and K. T. Ramesh, "Stability map for nanocrystalline and amorphous materials," *Physical Review Letters,* vol. 101, p. 025501, 2008.

[170] T. E. Mitchell and W. A. Spitzig, "Three-Stage Hardening in Tantalum Single Crystals," *Acta Metallurgica,* vol. 13, pp. 1169-1179, 1965.

[171] X. H. Zhu, *et al.*, "On the failure of pressure-sensitive plastic materials part 1: Models of yield and shear band behavior," *Scripta Materialia,* vol. 36, pp. 721-726, 1997.

[172] J. E. Carsley, *et al.*, "On the failure of pressure-sensitive plastic materials part II: Comparisons with experiments on ultra fine grained Fe-10% Cu alloys," *Scripta Materialia,* vol. 36, pp. 727-732, 1997.

[173] S. Cheng, *et al.*, "Strength and tension/compression asymmetry in nanostructured and ultraine-grain metals," *Acta Materialia,* vol. 51, pp. 4505-4518, 2003.

[174] A. C. Lund and C. A. Schuh, "Strength asymmetry in nanocrystalline metals under multiaxial loading," *Acta Materialia,* vol. 53, pp. 3193-3205, 2005.

[175] A. C. Lund and C. A. Schuh, "The Mohr-Coulomb criterion from unit shear processes in metallic glass," *Intermetallics,* vol. 12, pp. 1159-1165, 2004.

[176] E. Gurses and T. El Sayed, "On tension-compression asymmetry in ultrafine-grained and nanocrystalline metals," *Computational Materials Science,* vol. 50, pp. 639-644, 2010.

[177] E. M. Bringa, *et al.*, "Pressure effects on grain boundary plasticity in nanophase metals," *Applied Physics Letters,* vol. 89, 2006.

[178] E. Gurses and T. El Sayed, "A constitutive model of nanocrystalline metals based on competing grain boundary and grain interior deformation mechanisms.," *Materials Letters,* vol. 65, pp. 339-3395, 2011.

[179] J. J. Lewandowski and P. Lowhaphandu, "Effects of hydrostatic pressure on the flow and fracture of a bulk amorphous metal," *Philosophical Magazine A,* vol. 82, pp. 3427-3441, 2002.

[180] A. Jayaraman, "Diamond anvil cell and high-pressure physical investigations," *Review of Modern Physics,* vol. 55, p. 65, 1983.

[181] H. K. Mao, *et al.*, "Calibration of the ruby pressure gauge to 800 kbar under quasi-hydrostatic conditions," *Journal of Geophysical Research,* vol. 91, p. 4673, 1986.

[182] A. P. Hammersley, *et al.*, "Two dimensional detector software from real detector to idealised image or two-theta scan," *High Pressure Research,* vol. 14, p. 235, 1996.

APPENDIX A: PUBLICATIONS

C.R. Becker, K.E. Strawhecker, **J.P. Ligda**, C.A. Lundgren, *"Microfabricated Amorphous Silicon Nanopillars on an Ultrasmooth 500-nm-thick Titanium Adhesion Layer."* ARL-TR-6209 (2012).

J.P. Ligda, B.E. Schuster, Q. Wei, "*Transition in the Deformation Mode of Nanocrystalline Tantalum processed by High Pressure Torsion.*" Scripta Materialia 67 (2012) 253-256.

B.E. Schuster, **J.P. Ligda**, Z. Pan, Q. Wei, "*Nanocrystalline Refractory Metals for Extreme Condition Application,*" JOM 63 (2011) 27-31.

APPENDIX B: PRESENTATIONS

(Oral: Invited) Wei, Q., **Ligda, J.P**., Schuster, B.E., Society of Engineering Science 49th Annual Technical Meeting, Georgia Institute of Technology, Atlanta, GA, October 2012.

(Oral) **Ligda, J.P**., Schuster, B.E., Ren, Y., Scotto D'Antuono, D., Taheri, M., Wei, Q., "*Investigating Gradients in Texture and Grain Size in High Pressure Torsion Processed Body Center Cubic Metals*", Materials Science and Technology, Pittsburgh, PA, October 2012.

(Oral) **Ligda, J.P.**, Schuster, B.E., Wei, Q., *Microcompression and tension testing of nanocrystalline Tantalum and Tungsten*, The Minerals, Metals, and Materials Society Meeting, Orlando, FL, March 2012.

(Poster) **Ligda, J.P**., Schuster, B.E., Ren, Y., Wei, Q., *Transmission Electron Microscopy and Synchrotron X-ray Texture analysis of BCC metals Processed by High Pressure Torsion*, The Minerals, Metals, and Materials Society Meeting, Orlando, FL, March 2012.

(Poster) **Ligda, J.P.**, Schuster, B.E, Wei, Q., *Micromechanical Testing of Nanocrystalline BCC Metals*, The Minerals, Metals, and Materials Society Meeting, Orlando, FL, March 2012.

(Poster) **Ligda, J.P.**, Schuster, B.E, Wei, Q.,*Micromechanical Testing of Nanocrystalline BCC Metals*, FIB/SEM User's Group Meeting, Washington, DC, February 2012.

(Oral: Invited) **Ligda, J.P.**, *Microcompression and Microtension Testing of Nanocrystalline Tantalum*, 8th International Graduate Student Forum, Beihang University, Beijing, China, October 2011.

(Poster) **Ligda, J.P.**, Schuster, B.E., Ren, Y., Wei, Q., *Site-specific texture analysis of High Pressure Torsion processed bcc metals using synchrotron radiation*, Materials Science and Technology Meeting, Columbus, OH, October 2011.

(Oral) **Ligda, J.P.**, *Mechanical property variations of Nanocrystalline Tantalum processed by High Pressure Torsion*, ARL 2011 Summer Student Symposium, Aberdeen, MD, August 2011.

(Poster) **Ligda, J.P.**, Schuster, B.E., Wei, Q., *Mechanical Properties of Nanocrystalline Tantalum*, North Carolina Nanotechnology Commercialization Conference, Charlotte, NC, March 2011.

(Oral) **Ligda, J.P.**, Schuster, B.E., Wei, Q., *Deformation behavior of nanocrystalline and ultra fine grained Tantalum*, Materials Research Society Meeting, Boston, MA, November 2010.

APPENDIX C: DIAMOND ANVIL CELL

A.1 Introduction

The previous results for nanoindentation and tension presented here showed that the elastic modulus for NC Ta is lower than the accepted modulus. As another method for determining the elastic modulus diamond anvil cell (DAC) testing was done on Ta samples taken from two locations on the HPT disk. The DAC technique involves compressing a sample between two opposing diamond anvils. These anvils apply a high, hydrostatic pressure, while the sample is irradiated with a high energy x-ray beam. Since the sample is under hydrostatic pressure, as the compressive stress increases the atoms will be pushed closer together. This reduction in the lattice constant will result in a measurable change in the XRD peak positions. The applied pressure is determined from a standard sample so that the change in lattice constants, and therefore volume, with pressure can be plotted. From the volume vs. pressure plot the bulk modulus of the tested material is determined by fitting with an equation of state (EOS). This technique has been used extensively in geology when studying the high pressure response of materials commonly found in the Earth's crust, but few reports exist on its use for NC metals.

A.2 Experimental

Samples of UFG/NC Ta were prepared using FIB at locations near the disk center (X ~1.0 mm) and edge (X ~6.0 mm). An example of a DAC sample with dimensions roughly 40x40x20 μm is shown in FIGURE A.1a. These samples were made by

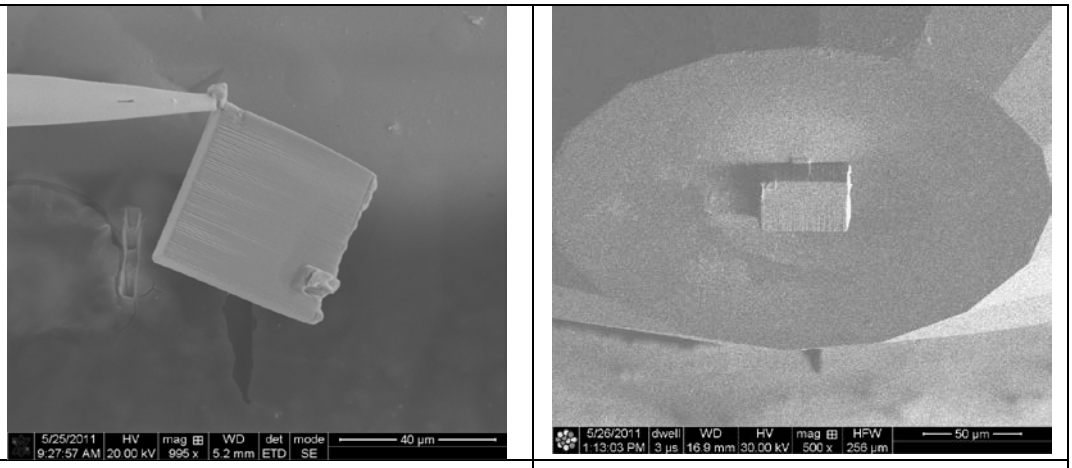

a) b)

FIGURE A.1: SEM images of an (a) prepared DAC specimen cut from HPT processed Ta and (b) this specimen attached to the culet of the diamond.

thinning a μ-EDM post to ~20 μm thick, similar to the process of creating a tensile specimen. With the sample in plane-view in the electron beam, an OmniProbe needle was attached to the sample and cut free from the bulk Ta disk. The sample must be in plain-view during this step so it can be set flat on the diamond face, as shown in FIGURE A.1b, where the diamond has a 300 micron culet.

A Rhenium gasket with an initial sample well diameter of approximately 125 microns and thickness of ~50 microns was positioned around the sample. A small crystal of sodium chloride was deposited in the sample well as an x-ray pressure calibration standard. A neon pressure medium was loaded into the sample chamber of the diamond anvil cells using a high pressure gas loading apparatus previously described [180]. The pressure was monitored in-situ during the experimental measurement using the ruby fluorescence method, which correlates the shift of the R_1 and R_2 fluorescence lines of ruby to a well-defined equation of state [181]. Ruby fluorescence measurements were typically made immediately preceding and after the x-ray diffraction measurement to examine pressure drift during data collection. Powder angle-dispersive x-ray diffraction

experiments were conducted at the California High-Pressure Science Observatory located at Beamline 12.2.2 of the Advanced Light Source at Lawrence Berkeley National Laboratory. The x-ray wavelength was 0.4133 Å. Each x-ray pattern was collected for approximately 300 seconds, with 3 patterns collected per pressure point. The patterns were integrated and reduced using the software Fit2D [182]. Background, defined by cubic-spline interpolation between selected minima in the diffraction patterns, was subtracted.

Structural parameters were determined from the diffraction patterns using the software UnitCell. Unit cell parameters at pressure were initially estimated from lower pressure values and pressure derivatives. Observed patterns were compared with predicted patterns and unit cell parameters were refined based on the most prominent and clearly identifiable diffraction peaks. The quality of the refinement was assessed by the precision of the least-squares fitting in Unit Cell. Volume data were analyzed using up to a fourth-order Birch-Murnaghan equation of state shown in equation A.1 [4].

$$P(f) = 3K_0 f(1+2f)^{5/2}\left[1 + \frac{3}{2}(K' - 4)f + \frac{3}{2}\left(K_0 K'' + K'(K' - 7) + \frac{143}{9}\right)f^2\right] \quad \text{equation A.1}$$

Here, $f = (1/2)\left[(V_0/V)^{2/3} - 1\right]$, where V_0 is the initial volume, V is the volume under pressure, K_0 is the ambient bulk modulus, and K' and K'' are the first and second pressure derivatives of the bulk modulus at ambient conditions, respectively.

A.3 Preliminary Results

A plot showing how the lattice spacing in Ta changes with pressure for both the center and edge specimens are shown in FIGURE A.2a and b respectively. As expected,

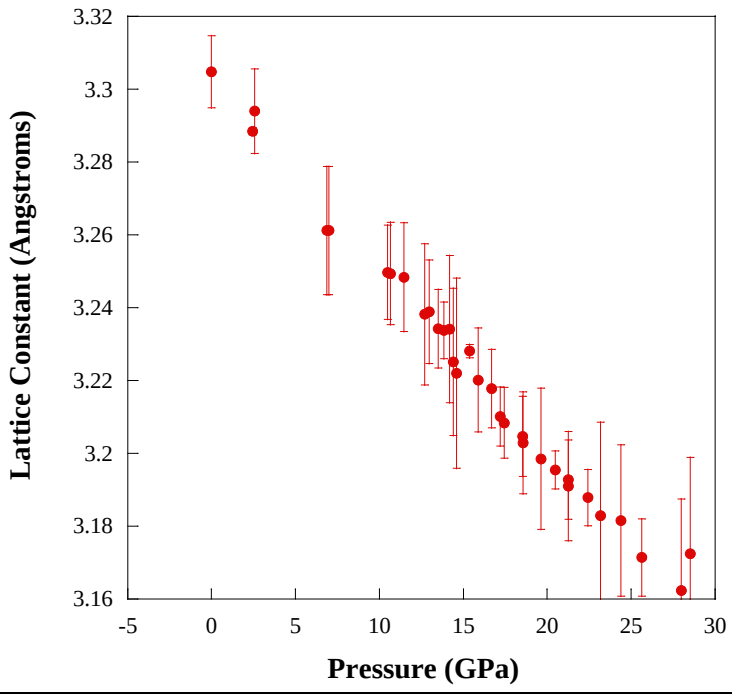

a)

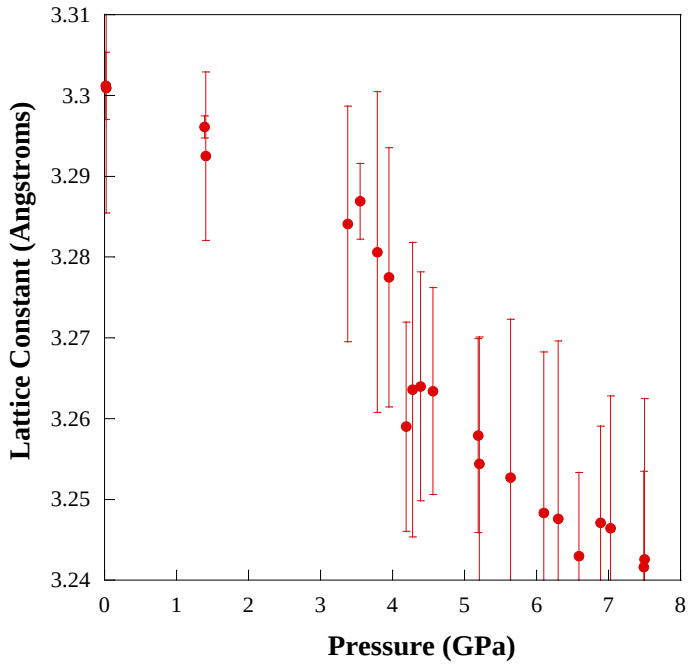

b)

FIGURE A.2: Tantalum lattice constant vs. pressure for the (a) center and (b) specimens. Both plots show a linear decrease with increasing pressure, but at all levels the XRD peaks are indexed as bcc tantalum. Pressure levels for the edge specimen do not reach those of the center specimen due to problems with the gasket assembly.

the lattice spacing decreases linearly with increasing pressure up to 30 GPa for the center specimen but only to ~ 8 GPa for the edge specimen. The lower pressure achieved for the edge specimen was due to a faulty gasket during testing. The lattice spacing started at 0.33 nm, the ambient spacing for Ta, and is compressed to 0.316 nm at the highest pressure. Scatter in this data is due to uncertainty during the peak matching process but shows the trend of decreasing lattice spacing with pressure.

Using these values, the unit cell volume can be calculated and plotted at each pressure, FIGURE A.3. It is easily seen in this figure that the trend for each specimen is similar, at least up to 8.0 GPa, the highest value obtained for the edge specimen. The low pressure values achieved for this specimen make it difficult to properly fit and determine a bulk modulus, therefore, only the center specimen was analyzed. Fitting the volume vs. pressure data for the center specimen to EQUATION A.1 gives a bulk modulus (K) value of K = 182.73 ± 4.01 GPa. Assuming Ta to be an isotropic linear elastic material, the elastic modulus can be calculated by, $E = 3K(1-2v)$. The bulk modulus is calculated from the DAC tests and the Poisson's ratio (v) is set to 0.35. From this equation, the elastic modulus for the center specimen is calculated to be 165 GPa. This value is lower than the accepted elastic modulus but close to both the nanoindenter and tensile data measured for this location.

A.4 Conclusions

Specimens for DAC testing were fabricated at locations near the center and edge of the HPT processed Ta disk. These specimens were compressed under high hydrostatic pressures while being exposed to high energy synchrotron x-ray radiation to measure decreases in lattice constant. From these lattice constants values the unit cell volume

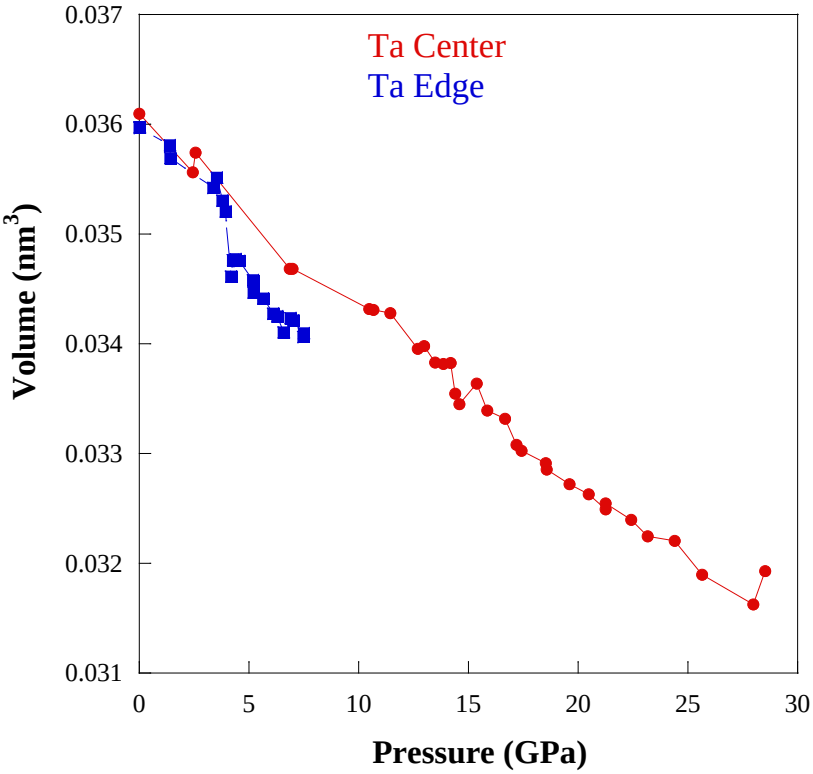

FIGURE A.3: Unit cell volume vs. pressure for Ta center and edge DAC specimens. Data for the center specimen was fit to equation A.1 to determine the bulk modulus, which can then be used to calculate the elastic modulus. This specimen shows a reduced elastic modulus value, when compared to the accepted modulus, but are close both the nanoindenter and tensile values. Tests on edge specimen failed at much lower pressures and were able to give a good fit to determine bulk modulus, but the overall trend seems to similar to the center specimen.

change with pressure can be calculated and fit to a fourth-order equation of state to determine the material's bulk modulus, which is in turn used to calculate the elastic modulus. Values for the center specimen give an elastic modulus value that is lower than the accepted modulus, but close to the nanoindenter and tensile data at similar locations. Tests for the edge specimen were not successful so no values could be determined. However, the similarities between of the DAC, nanoindenter, and tension values of the center specimens indicated that the elastic modulus is reduced even for bulk density NC metals. It is worthwhile to perform more DAC tests on an edge specimen to determine if

the modulus drops even more, considering the smaller grain sizes in this region and the fact that the measured tension modulus dropped to 145 GPa.

APPENDIX D: SPECIMEN FABRICATION/TENSION IMAGING SCRIPTS

B.1 Introduction

The goal for this appendix is to provide a description for running AutoFrancis and an understanding of the underlying code to mill the specimens. AutoFrancis automates the milling of compression pillars and tension dog-bone specimens at multiple positions using the FIB. This program allows the creation of specimens with a variety of sizes, and standardizes the image matching by using set fiducial sizes.

There are two main steps required in order to create a compression test sample. The first step is a rough cut of the sample and the second step is the thinning part, and each contains a set of sub steps that must be completed to create a full specimen. The program uses a script called AutoMike, created by Mike Seekely and Mike Uchic from the Air Force Research Laboratory, to thin the compression pillars. AutoFrancis does not change the source code of AutoMike. There are three steps for creating a tension specimen. The first two steps are the rough cut and thinning, and the last is milling the dog-bone shape.

B.2 Running AutoFrancis

AutoFrancis v1.0 requires RunScript, a program available through FEI company, to be executed. All the required files, including .bmp, .psc, and .ini files, must be located in the same folder. An image of the main RunScript screen is shown in

FIGURE B.1a, and the user must open the file “AutoFrancis.psc” and add it to RunScript before running the program. There are also some features in RunScript that can be activated by the user, and these include an option to view any images taken during an image match command and options to turn off both the electron and ion beams after completing a script, FIGURE B.1b. To run a selected script the user must hit the “play” button, identified by the red circle in FIGURE B.1c.

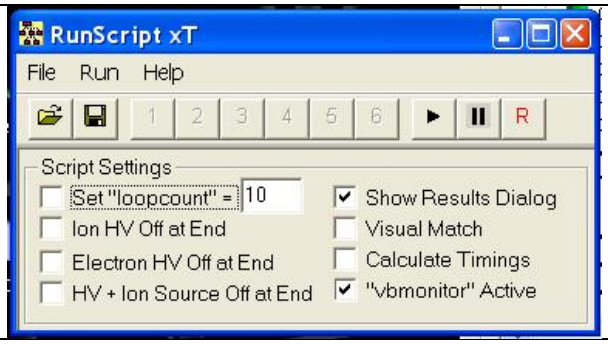

a

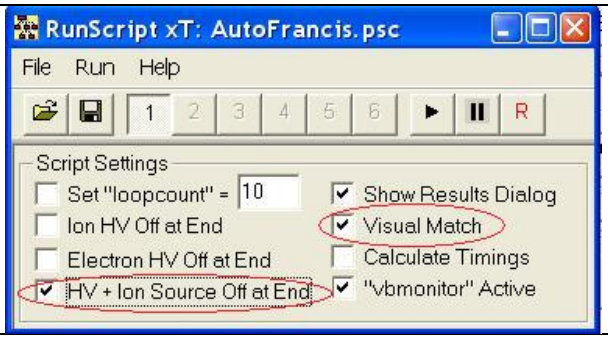

b

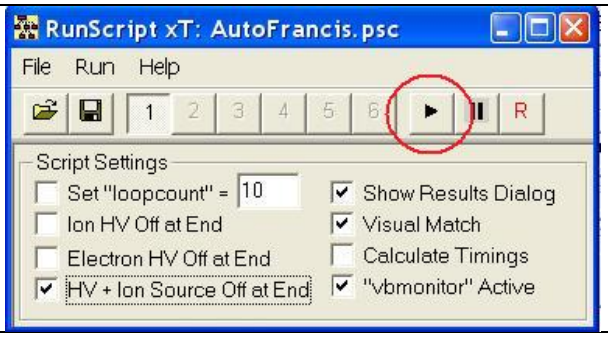

c

FIGURE B.1: Screens shots showing (a) the main RunScript interface, (b) options for image matching and turning the source off, and (c) play button that will execute the loaded script.

TABLE B.1: Sizes for the inner and outer diameter of the circle fiducial needed to fabricate pillars with a diameter of 2.5, 5, 10, or 20 µm by using AutoFrancis. For other diameters no listed here, new fiducials must be made where the outer diameter is half that of the pillar diameter.

Pillar Dia.	Inner Diameter	Outer Diameter
2.5 µm	1 µm	1.25 µm
5 µm	2.25 µm	2.5 µm
10 µm	4.5 µm	5 µm
20 µm	8.5 µm	10 µm

B.3 AutoFrancis: Compression

There are a number of preconditions that must be met before running AutoFrancis. Each operation requires specific fiducial marks and stage positions for it to be successful. For a compression pillar, the rough cut step requires the stage to be tilted at 52°, while the thinning step requires the stage to be at a 0° tilt. The thinning step also requires a circle fiducial to be milled into the top of the rough pillar with the dimensions given in TABLE B.1. These values are only for fiducials used in making pillars with diameters of 2.5, 5.0, 10, or 20 µm. Also, since the AutoMike program uses a log file to keep track of current positions and milling depths, the user must uncheck the "Logging Active" function, FIGURE B.2, in RunScript BEFORE RUNNING AutoFrancis.

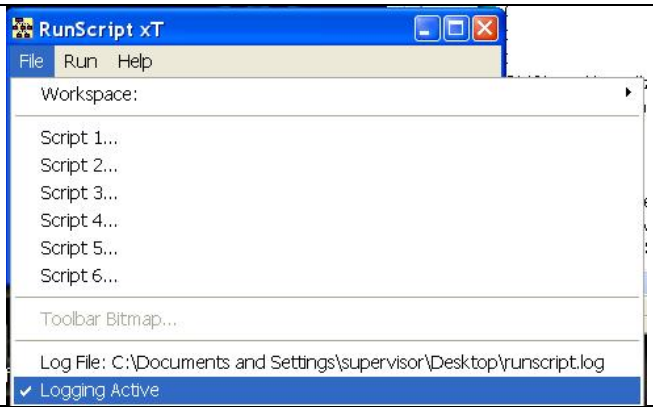

FIGURE B.2: Screen shot showing how to remove the "Logging Active" function in RunScript, needed to effectively run the pillar thinning scripts.

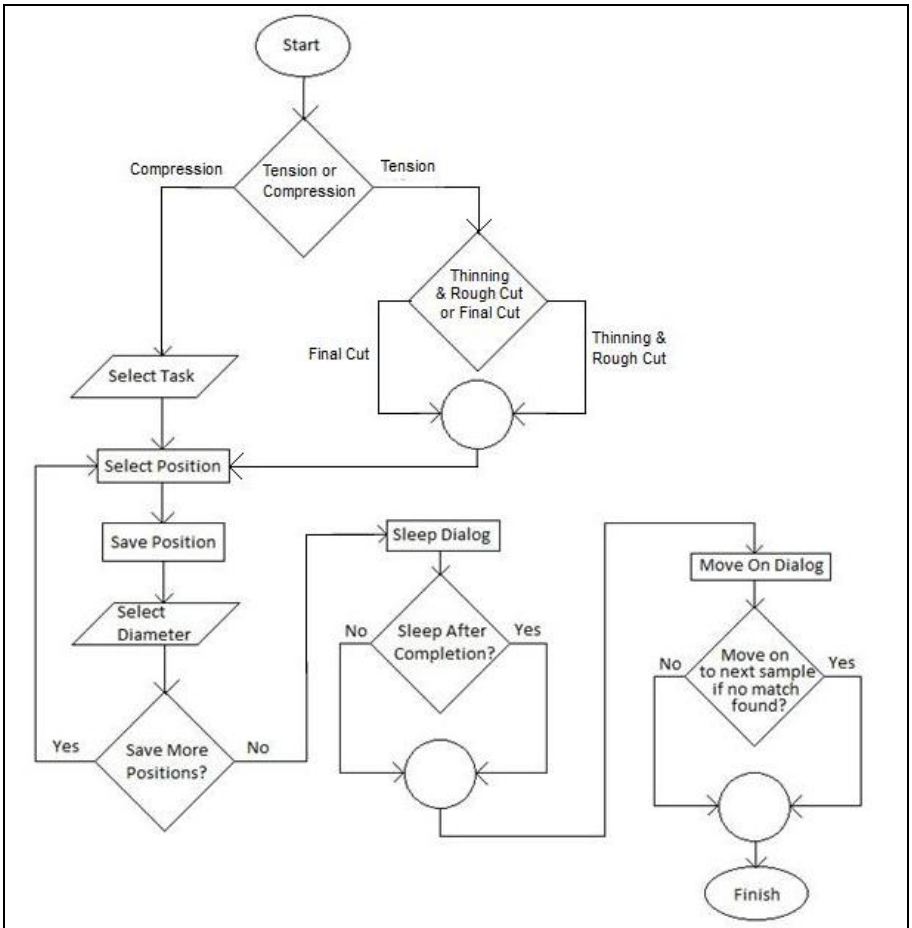

FIGURE B.3: Flow diagram of the steps in the "AutoFrancis" program taken for setting up initial locations and sizes of a compression or tensile specimens.

The following information is step-by-step instructions on running AutoFrancis to complete a compression pillar, a screen shot of any referenced dialog box can be found in FIGURE B.4a – g. Also, a flow diagram for AutoFrancis is shown in FIGURE B.3.

B.3.1 Compression Rough Cut

1. AutoFrancis Dialog: Select Compression: FIGURE B.4a
2. Select Task Dialog: Select Rough Cut: FIGURE B.4b
3. On the user interface, navigate to desired location
4. Save Current Position Dialog: Select Save to save current position: FIGURE B.4c
5. Diameter Size Dialog: Select Diameter Size: FIGURE B.4d

6. Add more positions Dialog: Select No (Alternative 1): Figure B.4e
7. Sleep Option Dialog: Select No (Alternative 2): Figure B.4f
8. Move On Dialog: Select No (Alternative 3): Figure B.4g
9. End

Alternative 1

1. Add More Positions Dialog: Select Yes: 1: Figure B.4e
2. Continue to Step 3 in section B.2.1

Alternative 2

1. Sleep Option Dialog: Select Yes: Figure B.4f
2. Continue to Step 8 in section B.2.1

Alternative 3

1. Move On Dialog: Select Yes: Figure B.4g
2. Continue to Step 9 in section B.2.1

B.3.2 Compression Thinning

1. AutoFrancis Dialog: Select Compression: Figure B.4a
2. Select Task Dialog: Select Thinning: Figure B.4b
3. On the user interface, navigate to desired location with a fiducial
4. Save Current Position Dialog: Select Save to save current position: Figure B.4c
5. Diameter Size Dialog: Select Diameter Size: Figure B.4d
6. Add more positions Dialog: Select No (Alternative 1) : Figure B.4e
7. Sleep Option Dialog: Select No (Alternative 2) : Figure B.4f
8. Move On Dialog: Select No (Alternative 3) : Figure B.4g
9. End

Alternative 1

1. Add More Positions Dialog: Select Yes: Figure B.4e
2. Continue to Step 3 in section B.2.2

Alternative 2

1. Sleep Option Dialog: Select Yes: Figure B.4f
2. Continue to Step 8 in section B.2.2

Alternative 3

1. Move On Dialog: Select Yes: FIGURE B.4g
2. Continue to Step 9 in section B.2.2

B.4 AutoFrancis: Tension

For tensile specimens, the bulk sample must be attached to a 45° pre-tilted holder for the rough cut and thinning steps. These steps require a bullzeye fiducial milled into the material at the desired location for the tensile specimen with the dimensions listed in the first row of TABLE B.2. The stage must also be tilted to 7.0° with the sample surface perpendicular to the ion beam. The last step of creating a tension specimen is milling the dog-bone shape. This final cut requires a vertical holder so that the recently thinned plate is normal to the e-beam. The final cut also requires a bullzeye fiducial located at the free end of the tensile specimen with dimensions listed in row two of TABLE B.2. For this holder, the stage must be tilted to 52° so that the thinned plate is normal to the ion beam.

TABLE B.2: Size of the bullzeye fiducials needed to run the tension scripts for the rough/thinning and final milling of specimens.

	Inner Diameter 1	Outer Diameter 1	Inner Diameter 2	Outer diameter 2
Rough/Thinning	4 µm	5 µm	0 µm	1 µm
Final	4 µm	5 µm	0 µm	1.5 µm

a

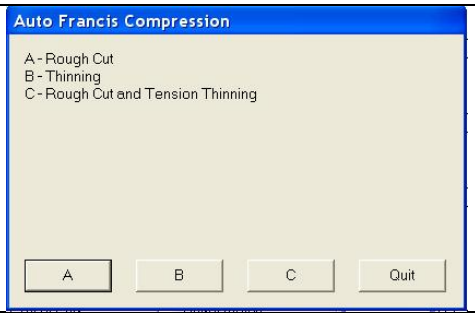

b

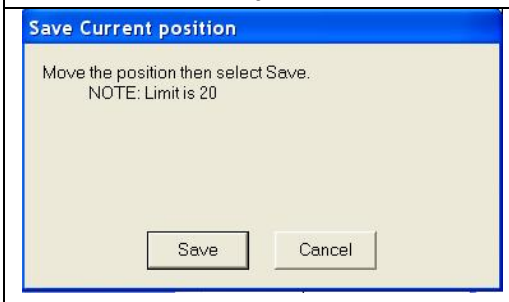

c Save Current Position

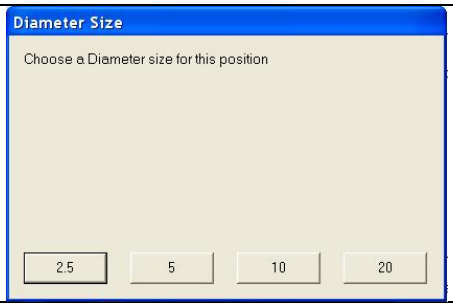

d Diameter Size Dialog

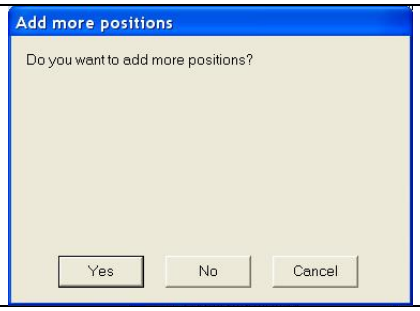

e Add more positions Dialog

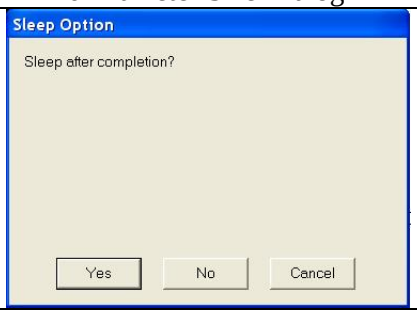

f Sleep Option Dialog

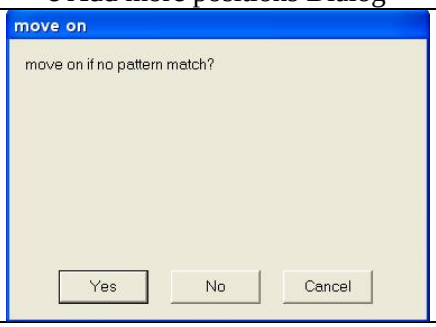

g move on Dialog

FIGURE B.4: Compression dialog boxes for the (a) main AutoFrancis interface, (b) compression specific scripts, (c) milling location, (d) pillar diameter, (e) multiple positions, (f) machine sleep mode, and (g) moving to the next specimen.

The following are step-by-step instructions on running AutoFrancis to complete a tensile specimen, a screen shot of any referenced dialog box can be found in FIGURE B.5a – g. The flow diagram for AutoFrancis in FIGURE B.3 also applies to the tension scripts.

B.4.1 Tension Rough Cut

1. AutoFrancis Dialog: Select Tension: FIGURE B.4a
2. Auto Francis Tension Dialog: Select Rough Cut and Thinning: FIGURE B.5a
3. AutoFrancisTension Dialog: select Rough Cut: FIGURE B.5b
4. On the user interface, navigate to desired location with a fiducial
5. Save Current Position Dialog: Select Save to save current position: FIGURE B.5c
6. Gauge Size Dialog: Select Size: FIGURE B.5d
7. Add more positions Dialog: Select No (Alternative 1): FIGURE B.5e
8. Sleep Option Dialog: Select No (Alternative 2): FIGURE B.5f
9. Move On Dialog: Select No (Alternative 3): FIGURE B.5g
10. End

Alternative 1

1. Add More Positions Dialog: Select Yes: FIGURE B.5e
2. Continue to Step 4 in section B.3.1

Alternative 2

1. Sleep Option Dialog: Select Yes: FIGURE B.5f
2. Continue to Step 9 in section B.3.1

Alternative 3

1. Move On Dialog: Select Yes: FIGURE B.5g
2. Continue to Step 10 in section B.3.1

B.4.2 Tension Thinning

1. AutoFrancis Dialog: Select Tension: FIGURE B.4a
2. Auto Francis Tension Dialog: Select Rough Cut and Thinning: FIGURE B.5a
3. AutoFrancisTension Dialog: select Thinning: FIGURE B.5b
4. On the user interface, navigate to desired location with a fiducial
5. Save Current Position Dialog: Select Save to save current position: FIGURE B.5c
6. Gauge Size Dialog: Select Size: FIGURE B.5d
7. Add more positions Dialog: Select No (Alternative 1): FIGURE B.5e
8. Sleep Option Dialog: Select No (Alternative 2): FIGURE B.5f
9. Move On Dialog: Select No (Alternative 3): FIGURE B.5g
10. End

Alternative 1

1. Add More Positions Dialog: Select Yes: FIGURE B.5e
2. Continue to Step 4 in section B.3.2

Alternative 2

1. Sleep Option Dialog: Select Yes: FIGURE B.5f
2. Continue to Step 9 in section B.3.2

Alternative 3

1. Move On Dialog: Select Yes: FIGURE B.5g
2. Continue to Step 10 in section B.3.2

B.4.3 Tension Final Cut

1. AutoFrancis Dialog: Select Tension: FIGURE B.4a
2. Auto Francis Tension Dialog: Select Final Cut: FIGURE B.5a
3. On the user interface, navigate to desired location with a fiducial

4. Save Current Position Dialog: Select Save to save current position: FIGURE B.5c
5. Gauge Size Dialog: Select Size: FIGURE B.5d
6. Add more positions Dialog: Select No (Alternative 1): FIGURE B.5e
7. Sleep Option Dialog: Select No (Alternative 2): FIGURE B.5f
8. Move On Dialog: Select No (Alternative 3): FIGURE B.5g
9. End

Alternative 1

1. Add More Positions Dialog: Select Yes: FIGURE B.5e
2. Continue to Step 4 in section B.3.3

Alternative 2

1. Sleep Option Dialog: Select Yes: FIGURE B.5f
2. Continue to Step 9 in section B.3.3

Alternative 3

1. Move On Dialog: Select Yes: FIGURE B.5g

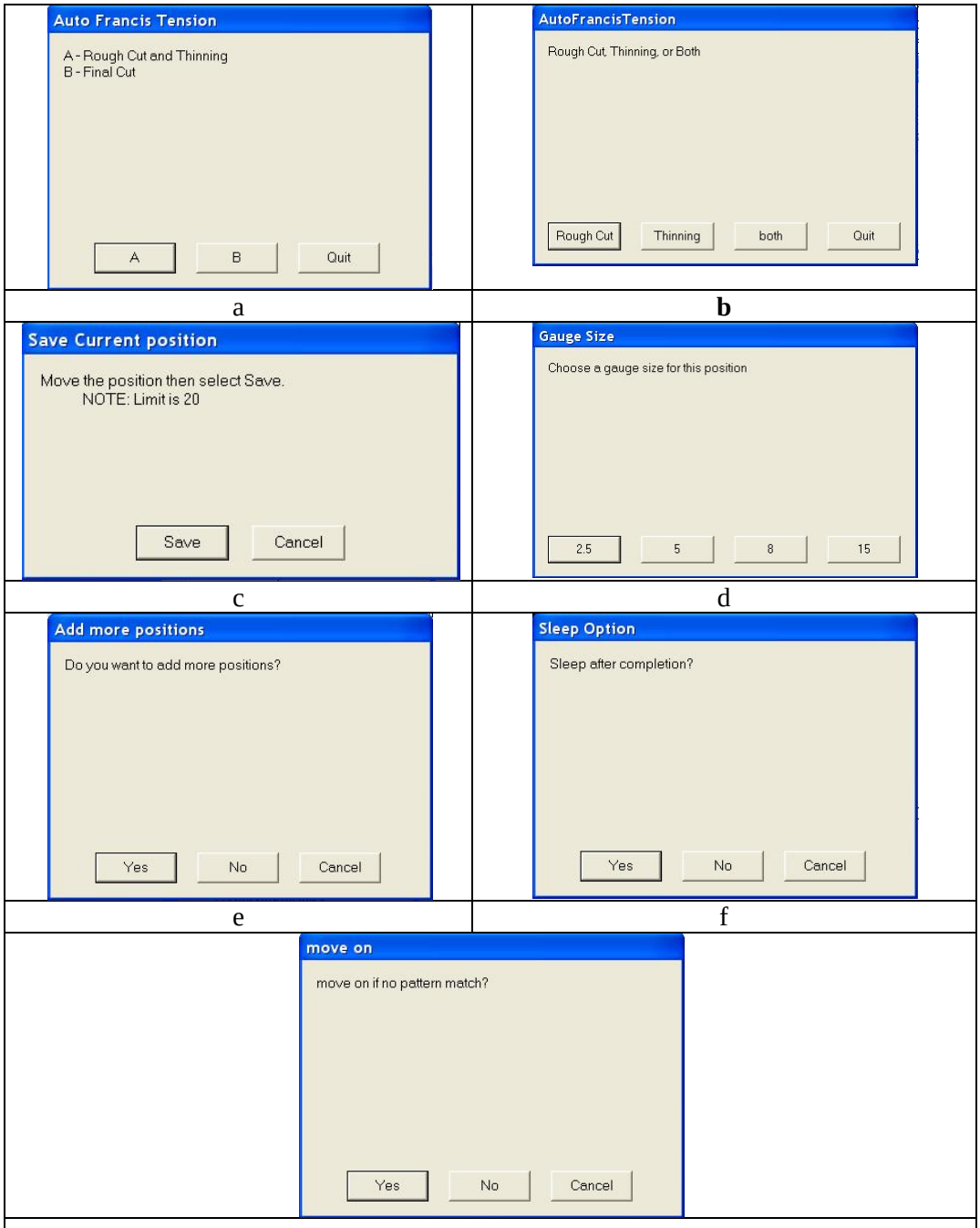

FIGURE B.5: Tension script dialog boxes for the (a) tension specific scripts, (b), specific thinning scripts to reach the desired gauge thickness (c) milling location, (d) specimen gauge width, (e) multiple positions, (f) machine sleep mode, and (g) moving to the next specimen.

B.5 Example Code: Compression

All of the scripts were written in Microsoft Notepad using a language specific for the FEI microscope. The most crucial commands used in these scripts control the

microscope imaging, milling, and movements similar to the way a user would. The important imaging commands are, "**getmag**", "**setmag**", "**grabframe**", and "**match**" which allows an image to be captured at a set magnification and match the location of a bitmap during the compression pillar thinning. Main milling commands include inserting "**box**" and "**circle**" patterns with specific side lengths or inner/outer diameters respectively, along with ion beam aperture selection, "**getaperture**". Stage movements are done by the "**stagemove**" command that defines specific x, y, z, r, and t positions. This language also allows for defining variables, setting up loops, and calling child scripts from a parent script. There are many more commands available with this language but these represent the most frequently used ones.

An example of the main "AutoFrancis" script used to set up locations for milling specimens is shown in FIGURE B.6 below. This script allows for 20 separate positions to be saved for milling, each with a specific pillar diameter. Only the code for two positions is shown here due to the lengthy amount needed for all 20 positions.

```
positionCounter = 0
sleepAfterCompletion = 0
roughCut = 0
thinning = 0
both = 0
ellipsepat = 0
moveon = 0

xa1=  0
ya1=  0
xa2=  0
ya2=  0
xb1=  0
yb1=  0
xb2=  0
yb2=  0
xe1=  0
ye1=  0
xe2=  0
ye2=  0
```

```
dialog 4, "A", "B", "C", "Quit", "Auto Francis Compression", "A - Rough Cut
B - Thinning  C - Rough Cut and Tension Thinning"
if (dresult = 1) roughCut = 1
if (dresult = 2) thinning = 1
if (dresult = 3) both = 1
if (dresult = 4) goto end
if (both = 1) thinning = 1
if (both = 1) roughCut = 1

saveLoop:
	dialog 2, "Save", "Cancel", "Save Current position", "Move the position then
select Save. NOTE: Limit is 20"
	if (dresult = 2) goto end
	dialog 1, "OK", "Current Positions", "The current position is saved"

	#reset xyzrt
	x = 0
	y = 0
	z = 0
	r = 0
	t = 0
	c = 0
	b = 0
	p = 0

dialog 4, "2.5", "5", "10", "20", "Diameter Size", "Choose a Diameter size for this
position"
	if (dresult = 1) p = 2.5
	if (dresult = 2) p = 5
	if (dresult = 3) p = 10
	if (dresult = 4) p = 20

	getstagepos
	getdetcontrast c
	getdetbrightness b
	positionCounter = positionCounter + 1

	if (positionCounter > 20) goto end

	if (positionCounter = 1) goto setPosition1
	if (positionCounter = 2) goto setPosition2
continue:
	dialog 3, "Yes", "No", "Cancel", "Add more positions", "Do you want to add
more positions?"
	if (dresult = 1) goto saveLoop
	if (dresult = 2) goto sleepOption
	if (dresult = 3) goto end
#-------------------------------------------------------------
#SET POSITIONS TO VARIABLES
```

```
#-----------------------------------------------------------------
setPosition1:
	x1 = x
	y1 = y
	z1 = z
	r1 = r
	t1 = t
	c1 = c
	b1 = b
	p1 = p
goto continue
setPosition2:
	x2 = x
	y2 = y
	z2 = z
	r2 = r
	t2 = t
	c2 = c
	b2 = b
	p2 = p
goto continue

#-----------------------------------------------------------------
#Start Compression Milling
#-----------------------------------------------------------------

sleepOption:
	dialog 3, "Yes", "No", "Cancel", "Sleep Option", "Sleep after completion?"
	if (dresult = 1) sleepAfterCompletion = 1
	if (dresult = 3) goto end
	dialog 3, "Yes", "No", "Cancel", "move on", "move on if no pattern match?"

	if (dresult = 1) moveon = 1
	if (dresult = 3) goto end

goto position1

position1:
	stagemove xyzrt, x1, y1, z1, r1, t1
	setdetcontrast c1
	setdetbrightness b1
	ellipsepat = p1
	run initializeManager.ini
	#if (roughCut = 1) run fiducialmatch.ini
	if (roughCut = 1) run roughCutController.ini
	if (both = 1) run fiducialmatch2.ini
	if (thinning = 1) run AutoMike_v2.0_1.ini
	positionCounter = positionCounter - 1
if (positionCounter = 0) goto end

position2:
```

```
        stagemove xyzrt, x2, y2, z2, r2, t2
        setdetcontrast c2
        setdetbrightness b2
        ellipsepat = p2
        run initializeManager.ini
        #if (roughCut = 1) run fiducialmatch.ini
        if (roughCut = 1) run roughCutController.ini
        if (both = 1) run fiducialmatch2.ini
        if (thinning = 1) run AutoMike_v2.0_1.ini
        positionCounter = positionCounter - 1
if (positionCounter = 0) goto end
```

FIGURE B.6: "*AutoFrancis*" script for setting up multiple milling locations.

Depending on if the user chooses to perform the rough cut or thinning step at each position, that location's corresponding variable, "roughCut" or "thinning", value is changed from 0 to 1. If a rough cut is picked then the script shown below, "*21nARoughcut*", FIGURE B.7, will run to mill a rough pillar that has a diameter set by variable "p". This program simply mills a set of concentric circles with an inner diameter equal to the desired pillar diameter and an outer diameter of ~60 μm, large enough to accept the nanoindenter tip during compression. If instead the pillar is to be thinned, then the AutoMike script will run. This script is not shown here since it was provided by colleagues at AFRL.

```
#-----------------------------------------------------------------
#Rough Milling: Compression
#-----------------------------------------------------------------
getmag
if (mag<>1200) setmag 1200

getparallelmode
if (mode <>0) setparallelmode 0

setctrlbeam 0
setprimbeam 0
getaperture
if (aperture <>15) setaperture 15

getstagepos
xcenter=0
ycenter=0
r2=20
```

```
setpatinfo depth, si
circle xcenter, ycenter, r1, (r2 + 40)
mill
clear

setpatinfo depth, si
circle xcenter, ycenter, r1, (r2 + 30)
mill
clear

setpatinfo depth, si
circle xcenter, ycenter, r1, r2
mill
clear
```

FIGURE B.7: *"21nARoughcut"* script for milling the rough compression pillars.

B.6 Example Code: Tension

Milling of a tensile specimen has its own specific scripts, they are similar to the compression scripts but require different fiducials and stage positions. After choosing the desired locations, a rough thinning (FIGURE B.8) or final thinning (FIGURE B.9) are performed. The scripts for both steps are shown below. Following these two thinning steps the dog-bone pattern is milled to create the final tensile specimen, FIGURE B.10. The script shown below is used to mill a specimen with an 8.0 μm gauge width.

```
#---------------------------------------------------------------
#Rough Tension Thinning
#---------------------------------------------------------------

getaperture
if (aperture <> 15) setaperture 15
getmag
if (mag <> 1500) setmag 1500
getparallelmode
if (mode <> 0) setparallelmode 0
run fiducialmatchRC.ini
if (p = 2.5) yrough = 4.25
if (p = 5) yrough = 5.5
if (p = 8) yrough = 7
if (p = 15) yrough = 10.5
```

```
#using xsection============================
xfirst=-26+x
xsecond=26+x
yfirst=yrough+y
ysecond= 30+y
depth = 15
setpatinfo depth, si
xsect xfirst, (-1*ysecond), Xsecond, (-1*yfirst)
mill
clear
xsect xfirst, yfirst, xsecond, ysecond
setrotation 180, patkey
mill
clear
```

FIGURE B.8: "*TensionRoughCut*" script for thinning the μ-edm post to near the desired gauge thickness

```
-------------------------------------------------------------
#Tension Thinning
#-------------------------------------------------------------

if (p = 2.5) ythin = 3.25
if (p = 5) ythin = 5.75
if (p = 8) ythin = 7.75
if (p = 15) ythin = 10.5

stop=0
getstagepos
newt=t+1.5
stagemove t, newt
getaperture
if (aperture <>13) setaperture 13
run fiducialmatchT.ini
if (result = 0) goto exit
getmag
if (mag <> 2500) setmag 2500
xOne=-20+x
yOne= -ythin+y
xTwo= 20+x
yTwo= -(ythin+10)+y
depth= 9
setpatinfo depth, si
box xOne, yOne, xTwo, yTwo
mill
clear
```

```
yOne= -(ythin-2)+y
yTwo= -(ythin+5)+y
depth = 12
box xOne, yOne, xTwo, yTwo
mill
clear

# tilit to 5.5 from 8.5

getstagepos
newt=t-3
stagemove t, newt
getaperture
if (aperture <>13) setaperture 13
run fiducialmatchT.ini
if (mag <> 2500) setmag 2500


xOne=-20+x
yTwo= ythin+y
xTwo= 20+x
yOne= (ythin+10)+y
depth= 9
setpatinfo depth, si
box xOne, yOne, xTwo, yTwo
setrotation 180, patkey
mill
clear
yTwo= (ythin-2)+y
yOne= (ythin+5)+y
box xOne, yOne, xTwo, yTwo
setrotation 180, patkey
mill
clear

exit:
```

FIGURE B.9: "*Tensionthinning*" script for thinning the plate down to the final gauge thickness.

```
 #============================
#Tension Specimen Final Milling
#============================
#============================
# TOP MILLING
#============================
getstagepos
newt=50.5
stagemove t, newt
getaperture
if (aperture <>13) setaperture 13
run fiducialmatchF.ini
getmag
if (mag <> 1000) setmag 1000

#polygon milling--------------------------------
xOne=-60+x
yOne=20+y
xTwo=5+x
yTwo=20+y
xThree=-14+x
yThree=8+y
xFour=-49+x
yFour=8+y
depth=4
setpatinfo depth, si

yOne=35+y
yTwo=25+y
box xOne, yOne, xTwo, yTwo
mill
clear

depth=2
setpatinfo depth, si
yOne=30+y
yTwo=20+y
box xOne, yOne, xTwo, yTwo
mill
clear

depth=2
setpatinfo depth, si
yOne=25+y
yTwo=15+y
box xOne, yOne, xTwo, yTwo
mill
```

```
clear

depth=5
setpatinfo depth, si
yOne=20+y
yTwo=20+y
polygon xOne, yOne, xTwo, yTwo, xThree, yThree, xFour, yFour
mill
clear

#bitmap milling----------------------------------------------------
xOne=-60+x
yOne=17.2+y
xTwo=5+x
yTwo=5+y
depth=5
setpatinfo depth, si
bitmap "taper_top.bmp", xOne, yOne, xTwo, yTwo
setrotation 180, patkey
mill
clear

#2nd bitmap milling-----------------------
setaperture 10
run fiducialmatchF.ini
xOne=-60+x
yOne=16.2+y
xTwo=5+x
yTwo=4.5+y
depth=5
setpatinfo depth, si
bitmap "taper_top.bmp", xOne, yOne, xTwo, yTwo
setrotation 180, patkey
mill
clear
#====================================
# BOTTOM MILLING
#====================================
getstagepos
newt=53.5
stagemove t, newt
getaperture
if (aperture <>13) setaperture 13
run fiducialmatchF.ini
getmag
if (mag <> 1000) setmag 1000
```

```
#polygon milling----------------------------------------------------
xOne=-60+x
yOne=-20+y
xTwo=5+x
yTwo=-20+y
xThree=-14+x
yThree=-8+y
xFour=-49+x
yFour=-8+y
depth=4
setpatinfo depth, si

yOne=-35+y
yTwo=-25+y
box xOne, yOne, xTwo, yTwo
mill
clear

depth=2
setpatinfo depth, si
yOne=-30+y
yTwo=-20+y
box xOne, yOne, xTwo, yTwo
mill
clear

depth=2
setpatinfo depth, si
yOne=-25+y
yTwo=-15+y
box xOne, yOne, xTwo, yTwo
mill
clear

depth=5
setpatinfo depth, si
yOne=-20+y
yTwo=-20+y
polygon xOne, yOne, xTwo, yTwo, xThree, yThree, xFour, yFour
mill
clear

#bitmap milling-----------------------------------------------------
xOne=-60+x
yOne=-5+y
xTwo=5+x
yTwo=-17.2+y
```

```
depth=4
setpatinfo depth, si
bitmap "taper_bottom.bmp", xOne, yOne, xTwo, yTwo
mill
clear

#2nd bitmap milling----------------------
setaperture 10
run fiducialmatchF.ini
xOne=-60+x
yOne=-4.5+y
xTwo=5+x
yTwo=-16.2+y
depth=5
setpatinfo depth, si
bitmap "taper_bottom.bmp", xOne, yOne, xTwo, yTwo
mill
clear
```

FIGURE B.10: "*8umdogbone*" script for milling the final dog-bone tensile geometry into the thinned plate

An example of a fiducial matching program and the bitmap, "bullzeye_final.bmp" used during the final patterning is shown in FIGURE B.11a below. The lines in bold reference the fiducial that must be matched, shown in FIGURE B.11b.

```
#Pattern Matching File for tension fiducial
n=0
cbCount = 5
getdetcontrast origContrast

#increase contrast loop
loop:
        getmag
        if (mag <> 1000) setmag 1000
        grabframe 0,0,1024,884,2,800,0
        sleep 400
        threshold = 0.3
        match bullzeye_final.bmp 0.5,0.5
        if (result=1) goto putToMiddle
        if (result=0) run cbAdjust.ini
        cbCount = cbCount - 1
        if (cbCount = 0) goto cont
        getdetcontrast curContrast
        if (curContrast > 100) goto cont
goto loop
```

```
#decrease contrast loop
cont:
        cbCount = 10
        setdetcontrast origContrast
        loop2:
        getmag
        if (mag <> 1000) setmag 1000
        grabframe 0,0,1024,884,2,800,0
        sleep 400
        threshold = 0.3
        match bullzeye_final.bmp 0.5,0.5
        if (result=1) goto putToMiddle
        if (result=0) run decreaseContrast.ini
        cbCount = cbCount - 1
        if (cbCount = 0) goto end
        getdetcontrast curContrast2
        if (curContrast2 < 0) goto end
goto loop2

putToMiddle:
        imageposx = x/1000
        imageposy = y/1000
        imageposy2 = y/615.661
        if (y<0) y=y * (-1)
        if (x<0) x=x * (-1)
        if (y>1) goto skipcheckx
        if (x<1) goto skipstagemove
        skipcheckx:
        getstagepos
        imagexabs=x+imageposx
        imageyabs=y+imageposy2
        stagemove xy, imagexabs, imageyabs
        sleep 200
        goto loop
        skipstagemove:
        x=imageposx*1000
        y=imageposy*1000

end:
```

a

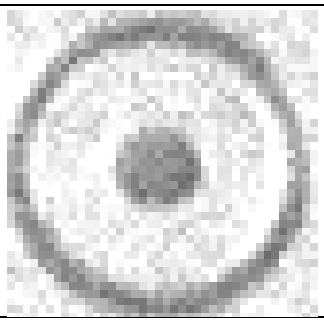

b

FIGURE B.11: (a)“*fiducialmatch_F*” script used to match the fiducial on the specimen to the bitmap (b) on file.

B.7 AuotIT Script

As was mentioned previously, to obtain the highest quality images for DIC tracking the resolution along the gauge length section must be high. This was accomplished through the use of a third party imaging software provided by 4Pi. While using this program allows control over image resolution and aspect ratio, it does not contain an automatic image capture mode. This is overcome through use an AutoIt script, shown in FIGURE B. 12, to act as the user and tell the 4Pi software to capture sequential images. This script language uses commands that mimic common user actions in Windows based programs such as mouse clicks, key strokes, file saving, etc [150]. The bolded code in the first line within the “Do” loop corresponds to the start of e-beam image capture. Since the 4Pi software is not a common Windows program a mouse click command must be used. The values in the parenthesis for this command represent, from left-to-right, which mouse button to “click”, pixel location on the monitor, and number of clicks. This command only tells the 4Pi software to acquire an image, all imaging parameters (ie. resolution, aspect ratio, dwell time, acceleration voltage, and beam current) must be set by the user prior to testing. After starting an image the code must pause until capture is completed, after which the final image can be saved in a

```
$var “1000” ;initial image number
$savelocation =
C:\DocumentsandSettings\Supervisor\Desktop\Alex\alextests\PIC”
$exit = “0”
MouseClick(“left”,259,14,1,0) ;activate revolution window
MouseClick(“left”,35,68,1,0) ;select survey button
Sleep(1000) ;pause script for 1 second
Do
  MouseClick(“left”,92,69,1,0) ;select e-image button
  Sleep(51000) ;pause script for 51 seconds
  WinClose(“Channel 1 (1:4)”) ;exit out of e-image window
  WinWaitActive(“Close Warning”) ;wait for active window
  MouseClick(“left”,710,538) ;click save
  WinWaitActive(“Save File”) ;wait for window to open
  MouseClick(“left”,654,459,2,0) ;double click existing text
  Send(“DELETE”) ;delete initial text
  MouseClick(“left”,654,459,2,0) ;double click existing text
  Send(“DELETE”) ;delete initial text
  Send($savelocation) ;type save location
  Sleep(500) ;pause script for 500 milliseconds
  $var = $var + 1 ;add one to image number
  Send($var) ;type image number
  Send(“ENTER”) ;type enter key
  Sleep(3000) ;pause script for 3 seconds
Until $exit = “1” ;infinite loop
```

FIGURE B. 12: AutoIT code used for taking sequential SEM images with the third party imaging software. This code simulates user actions, such as mouse clicks and keystrokes to start SEM imaging and then save each image with a numerically incrementing file name.

predetermined location, with a specific file name. The saving portion of the code can be seen in the bolded lines 12 – 22, where the file name and location are determined by the “*var*” and “*savelocation*” variables respectively. While the file location remains the same, the name must advance numerically or the new image will overwrite any previous ones. This is easily done by defining the “*var*” variable as a number (ie. 1000) and having this variable advance by one increment for each saved image. After saving the image the loop repeats itself, taking a new image and saving it with a new name. This loop is an infinite loop, meaning it will continue until the user stops the AutoIt program. As a note, this code contains multiple “mouseclick” commands at specific locations, it is therefore

recommend to not move the physical mouse location as it could disrupt the code execution.